

MASTER

Design of a 3-D switched antenna array for mobile, high-resolution direction-of-arrival measurements

Kwakkernaat, M.R.J.A.E.

Award date:
2004

[Link to publication](#)

Disclaimer

This document contains a student thesis (bachelor's or master's), as authored by a student at Eindhoven University of Technology. Student theses are made available in the TU/e repository upon obtaining the required degree. The grade received is not published on the document as presented in the repository. The required complexity or quality of research of student theses may vary by program, and the required minimum study period may vary in duration.

General rights

Copyright and moral rights for the publications made accessible in the public portal are retained by the authors and/or other copyright owners and it is a condition of accessing publications that users recognise and abide by the legal requirements associated with these rights.

- Users may download and print one copy of any publication from the public portal for the purpose of private study or research.
- You may not further distribute the material or use it for any profit-making activity or commercial gain

Eindhoven University of Technology
Faculty of Electrical Engineering
Division of Telecommunication
Technology and Electromagnetism
Radiocommunications (ECR) Group



Design of a 3-D switched antenna array for mobile, high-resolution direction-of-arrival measurements

M.R.J.A.E. Kwakkernaat

August 2004

Master of Science Thesis
carried out from November 2003 to August 2004

Supervisors:
Dr. ir. Y.L.C. de Jong
Dr. R.J.C. Bultitude
Dr. M.H.A.J. Herben

Graduation professor:
Prof. dr. E.R. Fledderus

The Faculty of Electrical Engineering of Eindhoven University of Technology disclaims all responsibility for the contents of traineeship and graduation reports.

Abstract

The different propagation mechanisms in urban micro-cell environments play an important role in creating a high-quality cellular system. At this moment, more research is needed to determine the dominant propagation mechanisms, which in turn may lead to better propagation prediction models. Performing high-resolution direction-of-arrival (DOA) channel sounding measurements can significantly help to obtain a more fundamental understanding of the dominant propagation mechanisms in the mobile radio channel. Moreover, the results obtained from the measurements can be used to develop more accurate deterministic propagation prediction models.

To determine the DOAs and the power-delay-profiles of incident waves, a channel sounding system can be equipped with a suitable antenna array configuration. By examining the electrical signals at the different antenna elements in the array and using this information as input for a high-resolution direction-finding (DF) algorithm, it is possible to distinguish the DOAs and the corresponding powers-delay-profiles of multiple radio waves impinging on the array. The channel sounding system currently available at the TU/e is capable of estimating these signal properties, but needs to be upgraded in order to increase the measurement speed and to improve the resolution.

This thesis presents a three-dimensional (3-D) antenna array geometry and a high-resolution algorithm that can be used for mobile, high-resolution DOA estimations. The array geometry is designed using knowledge obtained from the investigation of different planar array geometries. In combination with a recently extended version of the Unitary ESPRIT algorithm, this array geometry is investigated on its DF performance capabilities.

A new Structured Least Squares (SLS) technique is developed that can improve the estimation results of the 3-D Unitary ESPRIT algorithm by solving its invariance equations more accurately. Simulations show a significant performance improvement compared to the standard structured least squares (SLS), total least squares (TLS) or least squares (LS) techniques.

Furthermore, simulations show that the 3-D tilted cross antenna array in combination with the extended Unitary ESPRIT algorithm is capable of resolving the true DOAs and the corresponding powers of a number of sources at arbitrary angles with typical values for the signal-to-noise ratio (SNR). The estimation accuracy is determined from the simulation results in different scenarios. Under typical conditions it is possible to obtain less than four degrees resolution in azimuth as well as in elevation, which is a large improvement to the current system where five degrees azimuth resolution but far less elevation resolution was available. A measurement speed of roughly 30Km/h is possible with the new system without introducing large errors in the measurements. This is of course a large improvement with the current system, which only operates in a static configuration.

The 3-D antenna array is designed as a switched antenna array. This makes it possible to use a novel impedance switching technique that helps to suppress the effects of mutual coupling between the antenna elements in the array by terminating the non-active elements in the array with a complex impedance. Simulation and measurement results prove the concept and show that the technique can be very effective in the type of application presented here.

Parts of the 3-D tilted cross array are already implemented and work is currently being done to finalise the array. Modifications on the current channel sounding equipment are also in progress to make it fit with the new 3-D antenna array. It is expected that the entire

measurement system will be operational within several months and that preliminary isolated measurements can be done to test the system. After these preliminary measurements prove to be successful the system will be tested in an actual urban environment.

The results of measurements with this new high-resolution DF system will contribute to the creation and improvement of more realistic radio channel simulators, as well as improve the understanding of the physical mechanisms governing radio propagation in urban microcells. Of particular importance are the results from *mobile* measurements, which can provide more information about the change in composition of the radio propagation in the mobile channel. This, in turn, will provide a basis for the design of radio systems that are better matched to the real-world behaviour of urban radio channels, and for more efficient planning of microcellular radio networks.

Acknowledgements

This master thesis project has been conducted between November 2003 and April 2004 within the Propagation Research Group at the Communications Research Centre (CRC) in Canada in close collaboration with the Radio Communications (ECR) group at the Eindhoven University of Technology (TU/e) in Eindhoven. The project was continued and finalised at the TU/e from May 2004 until August 2004.

First I would like to thank Dr. Robert Bultitude and Dr. Yvo de Jong from CRC and Dr. Matti Herben from TU/e for their support and ideas in the radio propagation and signal processing field. A message of thanks also to the people of the Radio Communications Technologies Group, and especially Tricia Willink and Joe Schlesak who provided the opportunity for Dr. Yvo de Jong to support me throughout this project. Furthermore, I would like to thank all colleagues at CRC that supported me with their ideas and work during the six months of my visit at CRC.

Finally, I thank Mostafa Hajian from Delft University of Technology (TUDelft), for recommending the FEKO software package and for providing us with one of their drooping-radial monopole antennas.

Contents

1	Introduction	1
1.1	Background	1
1.2	Previous work	3
1.3	Problem formulation	4
1.4	Objectives	5
1.5	Thesis outline	5
2	Measurement system	7
2.1	Introduction	7
2.2	Current measurement system	7
2.2.1	Channel sounder	7
2.2.2	Synthetic circular array	9
2.2.3	High-resolution algorithm	9
2.3	New measurement system	10
3	Antenna array configuration	13
3.1	Introduction	13
3.2	Uniform circular array design	14
3.3	Y-shaped array design	15
3.3.1	Uniform element spacing	15
3.3.2	Non-uniform element spacing	15
3.4	3-D tilted cross array design	17
3.4.1	Uniform element spacing	17
3.4.2	Non-uniform element spacing	19
3.5	Impedance switching	19
3.6	Performance comparison	20
3.6.1	Array performance	21
3.6.2	Description of the FEKO EM simulation software	25
3.6.3	Element performance	25
3.6.4	Conclusion	32
4	High-resolution DOA estimation	33
4.1	Introduction	33
4.2	Overview of high-resolution algorithms	33
4.2.1	Spectral estimation	34
4.2.2	Non-spectral estimation	35
4.3	Unitary ESPRIT	36

4.3.1	Standard ESPRIT	36
4.3.2	Unitary extension of standard ESPRIT	38
4.3.3	Application to 3-D array (3-D Unitary ESPRIT)	41
4.3.4	Solving invariance equations using an improved SLS technique	45
4.3.5	Power estimation	49
4.4	Simulation results	49
4.4.1	Assumptions	50
4.4.2	Signal estimation	51
4.4.3	Estimation accuracy	55
4.4.4	Resolution	58
4.5	Conclusion	60
5	Implementation issues	61
5.1	Introduction	61
5.2	Antenna array	61
5.2.1	Antenna elements	61
5.2.2	Support structure	63
5.2.3	Antenna switching	64
5.3	Impedance switching	65
5.3.1	Complex impedance	65
5.3.2	Prove of concept	66
5.3.3	Carbon support structure	69
5.3.4	Expected results	72
5.4	Doppler Considerations	74
5.5	Conclusion	76
6	Conclusions and recommendations	77
6.1	Conclusions	77
6.2	Recommendations	78
A	FEKO modelling	81
A.1	Skirted monopole	81
B	Switched-impedance simulation results	84
B.1	Uniform Y-shaped array	84
B.2	Non-uniform Y-shaped array	88
B.3	Uniform 3D tilted cross array	91
B.4	Non-uniform 3D tilted cross array	94
	References	97

Chapter 1

Introduction

1.1 Background

All wireless communication systems, among them cellular radio networks, transmit their signals over the wireless channel. This means that the capabilities of these systems are fundamentally determined by the properties of the radio channel. When a signal is sent by the transmitter, different propagation mechanisms cause multiple waves, with different power levels and propagation delays to arrive at the receiver via several paths of different length, as illustrated in figure 1.1.

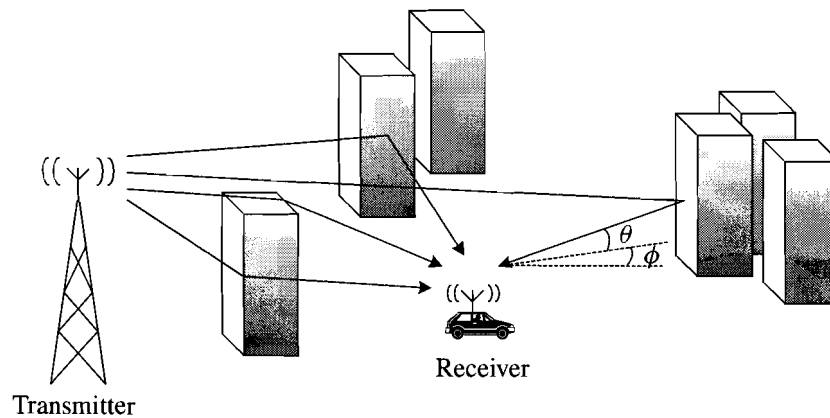


Figure 1.1: Multipath environment in mobile communications.

One of those propagation mechanisms is reflection, which can occur if a wave impinges on an object that is large compared to the wavelength. Diffraction can occur if the radio path between transmitter and receiver is obstructed by a surface with edges, which can cause a wave to bend around an obstacle. These edges are present in for example, vegetation and buildings with irregular surfaces. Furthermore, propagating radio waves can be attenuated by different obstacles or scattered by objects that are smaller than their wavelength. When mobility is considered as well, the radio propagation becomes rather complex, because the properties of radio channel vary with time and the location of the receiver, which can cause rapid fluctuations in the received power.

In today's mobile cellular systems the line-of-sight (LOS) propagation path is often blocked, which means that radiowave propagation via other mechanisms such as reflection,

diffraction and scattering becomes significant in urban microcell configurations. To guarantee a wide coverage and a high quality-of-service (QoS) and at the same time create a cellular system that is very efficient regarding the number of base-stations, accurate prediction of relevant radio channel parameters, such as path-loss, are important. This process is generally referred to as propagation prediction [1].

During the planning of cellular systems all coverage and interference calculations are based on propagation prediction, which makes it a very important issue in network planning. In contrast to the planning of macrocells, empirical propagation prediction models do not provide an acceptable prediction accuracy for microcell environments. Therefore the so-called deterministic propagation models, that can provide location specific channel predictions, are often used. Most of these deterministic models consider reflection and diffraction as the main propagation phenomena. Ray-based propagation prediction, which uses straight trajectories to describe the propagation of radio waves, has become an important method and provides better prediction results compared to the statistical models, when urban microcell scenarios are considered. Still, it is difficult to achieve the same prediction accuracy that can be achieved for macrocells. This has led to the idea that only considering reflection and diffraction may be insufficient to model the urban radio channel. Therefore, it is important to obtain a better and more fundamental understanding of the dominant propagation mechanisms in the mobile radio channel.

The radio channel impulse response is very important in obtaining a better understanding of the propagation effects, since it describes the radio propagation channel. Estimates of the channel impulse response are usually obtained using a channel sounding measurement system. Additionally, performing these measurements under mobile conditions will provide more information about the global behaviour of the radio propagation. This can be of great importance, since the users of the cellular network are often mobile themselves. For a better understanding about what causes the different propagation effects to occur, the direction at which the different waves reach the receiver can provide important information. These direction-of-arrivals (DOAs) can be measured by incorporating the channel sounding system with an antenna array.

The simplest way to incorporate an antenna array in the channel sounder is by means of a virtual array. This virtual array can be constructed by mechanically positioning the antenna of the channel sounder at different locations and subsequently measure the complex-impulse-responses (CIRs) at those locations, e.g. in a circular configuration as described in [1]. Because only one antenna element is present in this virtual array, the performance of the antenna is not influenced by other array elements. This technique can quite easily be implemented, but it has the disadvantage of being rather slow. Moreover, to prevent measurement errors, the properties of the radio channel should not change significantly during the sampling of a complete array, this makes mobile direction-finding (DF) hardly possible with this configuration.

Alternatively, the antenna array can also be constructed out of actual antenna elements. By sampling the electrical signals at each of the elements in the array, high-speed measurements can be performed, which makes it possible to perform mobile measurements without introducing large measurement errors. Sampling all antenna elements at the same time, however requires multiple receivers and a high data processing speed. Furthermore, in this multiple antenna array configuration a number of antenna elements are positioned at close proximity, which introduces electromagnetic coupling effects between the array elements, generally referred to as mutual coupling. These mutual coupling effects change the elec-

tromagnetical properties of the antennas and can deteriorate the performance of the total measurement system.

A very interesting type of antenna array that can be constructed by merging the previous two array types is the switched antenna array. This array is also constructed out of actual antenna elements, but instead of sampling all elements at the same time, a single receiver is used together with a RF-switch that samples each of the antenna elements in sequence, while the other elements in the array remain passive. While high measurement speeds are still possible, this configuration prevents the need for multiple receivers and gives way to an interesting technique that can help to minimise the mutual coupling effects between the array elements. This so called impedance switching technique changes the electromagnetic properties of the passive antennas by terminating them in a specific impedance, different from the 50Ω system impedance [2]. This makes the passive antennas less "visible" for the active antenna and can therefore help to suppress the mutual coupling effects and maintain accurate DOA estimations.

Estimating the DOAs of incident waves on an antenna array is long known to be possible with a technique called beamforming. In this technique, the output signals of the array elements are phase-shifted and combined in such a way that they add up coherently in a given direction. Sweeping this beam over a certain area and measuring the received power can indicate the possible directions of the incident waves. Although this technique can easily be applied to any array geometry, DF systems that are based on beamforming usually do not have a high-resolution performance. This resolution performance is generally defined as the ability to resolve two closely spaced sources. In systems that use beamforming to determine the DOAs, the resolution is roughly limited by the half-power-beamwidth (HPBW) of the antenna array pattern. To obtain more accurate estimates, high-resolution techniques have to be used that are known to offer a significantly better resolution performance. High-resolution techniques can provide this better resolution performance, because they use additional information obtained by multiple spatial sampling of the incoming wavefront and the additional assumptions made about the signals, such as a limited number of incident waves. If the assumptions about the signals are more specialised and conformed to the measured data, better resolution performance can be achieved.

The results of measurements with such a high-resolution DF system will contribute to the creation and improvement of more realistic radio channel simulators, as well as improve the understanding of the physical mechanisms governing radio propagation in urban microcells. Of particular importance are the results from *mobile* measurements, which can provide more information about the change in composition of the radio propagation in the mobile channel. This, in turn, will provide a basis for the design of radio systems that are better matched to the real-world behaviour of urban radio channels, and for more efficient planning of microcellular radio networks.

1.2 Previous work

At the Eindhoven University of Technology (TU/e) previous work described by De Jong [1], presents a virtual uniform circular array (UCA) in combination with a high-resolution algorithm named MUSIC that can be used for channel sounding measurements in micro cellular environments. The system is able to resolve the delay-profiles and DOAs of incident waves that arrive at low elevation angles. Part of the work focussed on obtaining a better physical understanding of radiowave propagation in micro cellular environments by means

of advanced experiments.

One of the recommendations of this work mentioned that two-dimensional propagation prediction models are inadequate for so called "small-cell" configurations, in which the base station antenna is located approximately at the rooftop level and over-rooftop propagation is no longer negligible. The current measurement equipment is mainly capable of performing two-dimensional measurements. To investigate three-dimensional propagation effects in the wireless channel, a new measurement system is necessary that can perform three-dimensional DOA estimations.

To investigate the global behavior of radiowave propagation in micro cellular environments it is important to perform measurements in which the receiving-end of the measurement system is moving along a trajectory. The present equipment is not capable of measuring delay profiles at typical urban speeds and does not allow mobile DF. To clear these limitations, higher measurement speeds are necessary.

At this moment, there is an ongoing project that concerns the design and implementation of a new and improved mobile channel sounding system that can perform high-speed delay-profile and three-dimensional DOA estimations. The new system will be an evolved version of the current measurement system described by De Jong. The work presented in this thesis reports on the results of the design and implementation of this new system.

1.3 Problem formulation

The current channel sounder operates at a frequency of 2.25GHz with an occupied bandwidth of 100MHz, and is equipped with a synthetic UCA. This array is a planar geometry, which means the resolution in the elevation plane at low elevation angles is poor and there exists a two-fold ambiguity with respect to the positive and negative elevation angles. To obtain more resolution in the elevation and to clear the ambiguity problem, a new channel sounder will have to be equipped with an antenna array geometry that extends into three dimensions.

To allow the receiving-end of equipment to move at typical urban speeds without introducing significant errors, the measurement speed of the system has to be sufficiently high. In order to perform these high-speed measurements, it is inevitable that the array has to be equipped with actual array elements instead of a single antenna that acts as a virtual array. A maximum of 32 antenna elements can be used in the new antenna array, which is caused by the time that is available to sample all elements in the array before the array has travelled a significant distance. The antenna elements used in the antenna array will consist of the drooping-radial monopole antenna as described in [3]. The new system will operate at the same frequency of 2.25GHz as the current system, which means that the antenna elements have to be tuned at this frequency.

Sampling all antenna elements simultaneously requires the use of multiple receivers and a very high speed data collection system. To prevent a highly complex and expensive system, antenna switching techniques need to be used to overcome this problem.

Using an array with actual antenna elements will introduce mutual coupling effects between the array elements, which affects the radiation pattern and input impedance of the active antenna and can cause severe performance degradation. An impedance switching technique that minimises these effects, as described in [2], can be used in order to create a reliable system.

To perform high-resolution DOA estimations, a high-resolution estimation algorithm

must be used that fits with a three-dimensional array geometry. Because measurements are usually performed in highly correlated environments, it is important that the algorithm is capable of distinguishing correlated sources.

It is expected that the limitations of the current channel sounding system can be mitigated with the aid of techniques described above and also by making appropriate changes to the current data-collection and data-processing system.

1.4 Objectives

The objective of this thesis is to develop a three-dimensional switched antenna array in combination with a suitable high-resolution algorithm that can be used to perform mobile DOA estimations with equal resolution in azimuth and elevation. In order to find a suitable 3-D antenna array design, different planar array geometries with uniform and non-uniform element spacing shall be investigated that may provide better angular resolution capabilities. Knowledge from the analysis of the planar arrays can be used in the design of a 3-D array geometry.

To suppress the mutual coupling effects between the antenna elements in the array, the effect of complex impedance loadings on the non-active antenna elements must be investigated. The effects can be simulated with computer software and later verified with measurements.

To perform accurate estimations, different high-resolution algorithms should be investigated and the potential of different signal processing techniques, such as forward/backward averaging and spatial smoothing can be analysed. If feasible, the current channel sounding system shall be modified and equipped with the new 3-D array geometry and preliminary measurements shall be performed.

The results of measurements with the new measurement system can improve the understanding of the physical mechanisms governing radio propagation in urban microcells. Moreover, the results can contribute to the verification and improvement of current ray tracing tools which can lead to more realistic radio channel simulators. Of particular importance are the results from *mobile* measurements, which can provide more information about the change in composition of the radio propagation. Additionally, the new system can very effectively be used for performance analyses of smart-antenna and MIMO-based systems. This, in turn, will provide a basis for the design of radio systems that are better matched to the real-world behaviour of urban radio channels, and for more efficient planning of micro-cellular radio networks.

1.5 Thesis outline

This thesis is organized as follows. Chapter 2 gives a description of the channel sounding system currently used at the TU/e and introduces the modifications that are needed to create the new and improved channel sounder.

Chapter 3 describes the development of the 3-D antenna array from the analysis of different planar array geometries. Simulation results will be presented that support the design considerations.

Chapter 4 gives a detailed description of the 3-D Unitary ESPRIT algorithm that is used in combination with the 3-D antenna array. Simulation results will be presented that indicate

the performance capabilities.

Chapter 5 discusses the implementation issues of the 3-D antenna array. Preliminary measurement results regarding the impedance switching technique are presented and the expected results taking into account the mutual coupling and shadowing effects are presented.

Finally, chapter 6 concludes the entire work and recommendations will be given.

Chapter 2

Measurement system

2.1 Introduction

For a better fundamental understanding of the dominant propagation mechanisms in mobile radio channels, it is important to perform measurements in which the different propagation delay times and directions-of-arrivals (DOAs) of the individual multipath components can be determined. The use of a channel sounding system makes it possible to determine these channel characteristics. This chapter will first give a short overview of the current TU/e measurement system and its capabilities. After that, a high-level description of the new measurement system will be given.

2.2 Current measurement system

In the work described by De Jong [1], the channel sounding measurement system that is currently being used at the TU/e is described. The current system is capable of estimating the delay-profiles and DOAs of propagating radio waves in a static configuration. In figure 2.1 the different parts of this system are shown.

2.2.1 Channel sounder

To analyse multipath propagation, time delay profiles which correspond to the complex impulse response (CIR) of a radio channel are widely used. An obvious way to measure the CIR is by transmitting a short RF-pulse and observe the received pulse or pulses. Collecting data from these high-resolution pulses is however, very difficult because of the large bandwidths that are required. A preferred method to determine an estimate of the CIR is by using a pseudonoise (PN) correlation method. The current TU/e measurement system is built up around a wideband radio channel sounder, which is based on this PN correlation method. In this method, a pseudonoise code sequence with a chiprate equal to $f_c = 1/T_c$ Hz is used as the baseband modulation signal to modulate the transmitted carrier. Here, T_c denotes the bit period of the sequence in seconds. The TU/e measurement system uses a transmitter that produces a 50Mbit/s reference PN sequence with a period of 511 bits. This sequence then modulates a 2250MHz carrier using binary phase-shift keying (BPSK). The output signal is then amplified to a power of 30dBm after which it is filtered and radiated via an antenna. At the receiver side the filtered and received signal is correlated with a replica of the transmitted PN sequence, as shown in figure 2.2.

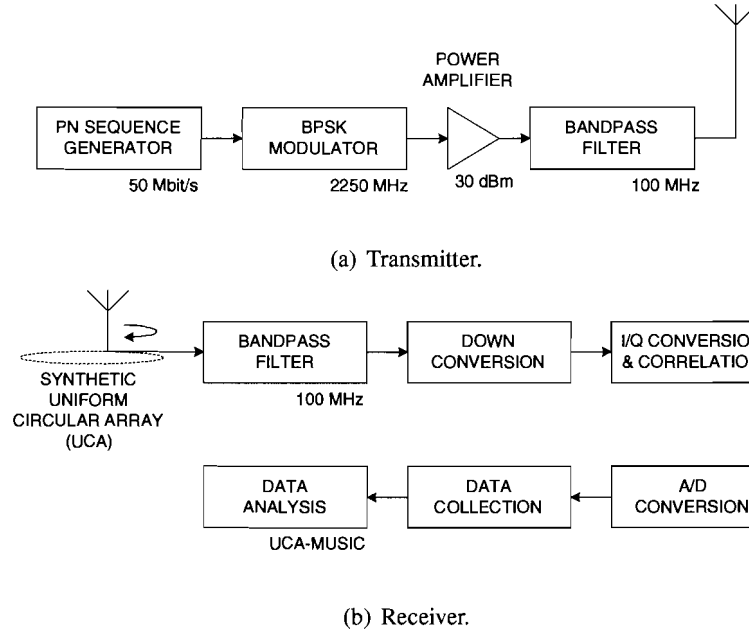


Figure 2.1: Current TU/e wideband radio channel sounder.

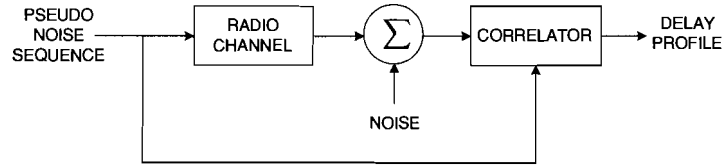


Figure 2.2: PN correlation method.

This correlation, or autocorrelation since the two signals are related to the same PN sequence, is based on determining the expected value of the product of two time shifted signals. The autocorrelation function can approximately be given by the delta function and therefore gives an estimate of the delay profile of the transmission channel. For a periodic PN binary sequence $a(t)$ with period T the autocorrelation function can be defined as

$$x(\tau) = \frac{1}{T} \int_0^T a(t)a(t - \tau)dt. \quad (2.1)$$

This function is not exactly a delta function, but a triangular function with a spread of $\pm T_c$ around the correlation peak and is periodic with period T because of the repeating nature of $a(t)$. The correlation of the received signal and the replica signal is performed by multiplying (mixing) the two signals followed by a low-pass integrator which integrates over the time interval 0 to T . Driving the replica signal at a slightly slower rate $f_c - \delta f_c$ than the rate f_c of the received signal causes the autocorrelation function $x(\tau/k)$ to be scaled in time with a factor $k = (f_c/\delta f_c)$. This means that the PN correlation method creates time stretched copies of a signal similar to that received by an ordinary receiver when a short delta-shaped pulse were transmitted through the same radio channel. A receiver that uses this same principle is called a sliding-correlator receiver and is currently used in the measurement system. A big advantage of the PN correlation method is that high-resolution time

delay measurements of the channel are possible without requiring a high sample speed at the receiver output and that the effects of RF-interference on the measurements are minimised

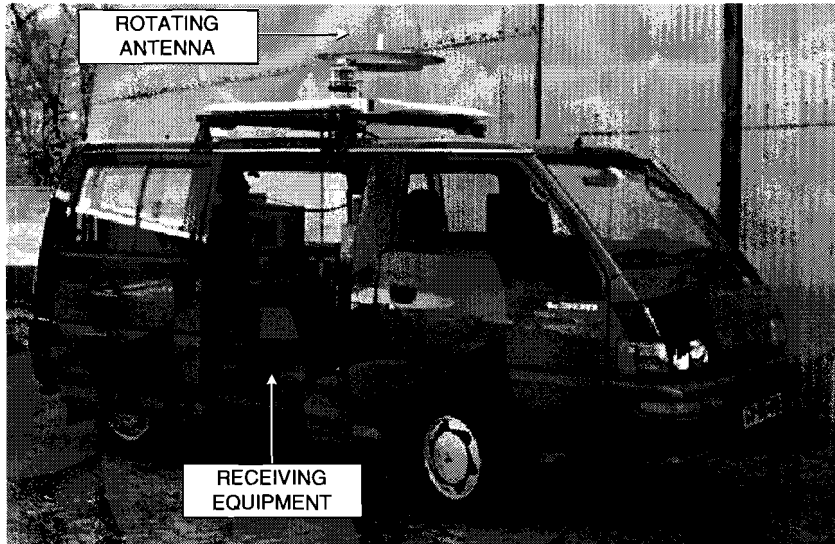


Figure 2.3: TU/e measurement vehicle.

A measurement vehicle, shown in figure 2.3, that acts as the receiver side contains the equipment to demodulate and correlate the received signal from which the CIR of the radio channel can be estimated. The measurement data samples from the receiver are digitised and transferred to harddisk. The total range of the CIRs is $10.22\mu\text{s}$ (511 bits of 20ns each) and the maximum dynamic range is 40dB.

2.2.2 Synthetic circular array

The antenna array used in the measurement system is a synthetic circular array, which consist of a single omni-directional antenna on a rotating arm. The antenna is a 2-dBi sleeve monopole antenna with a omnidirectional radiation pattern in the azimuth plane and a bandwidth of about 200MHz. Under static conditions this antenna is rotated at a constant speed along a horizontal circle with radius $r=0.30\text{m}$. Assuming the radio channel remains stationary during the measurement, this procedure is identical to measuring CIRs at the elements of a uniform circular antenna array (UCA). The system needs 16.0 seconds to move the antenna mechanically along a horizontal circle, which results in the recording of 157 CIRs. Such a complete set of samples taken over the entire array geometry is generally referred to as one "snapshot".

2.2.3 High-resolution algorithm

An angular high-resolution technique named UCA-MUSIC is used to provide better resolution performance than conventional beamformers. In addition to this, beamspace processing is used which helps to reduce the sensitivity to noise and modelling errors and allows to use forward/backward (FB) averaging. This FB averaging technique is used to decorrelate possible correlated signals. To give an estimation of the number of incident signals on the

array a modified version of Akaike's information criterion (FB-AIC) was applied. When the direction of the incident waves is close to horizontal, an azimuth resolution of less than 5 degrees is roughly available using 20 snapshots or more.

2.3 New measurement system

The current measurement system available at the TU/e is capable of estimating DOAs of propagating radio waves in a static configuration. Although the system is capable of performing azimuth and elevation DF estimations, the resolution in elevation is relatively poor. The lack of resolution in elevation, the limitation of a static configuration and the relatively slow measurement speed are the main drivers behind the idea of modifying the current channel sounding system.

The modifications concern the receiving side of the system and mainly involve the design of a new antenna array together with a suitable high-resolution signal processing technique. Figure 2.4 shows a diagram of the receiving part of the new measurement system. The new system will be installed on the same measurement vehicle as shown in figure 2.3.

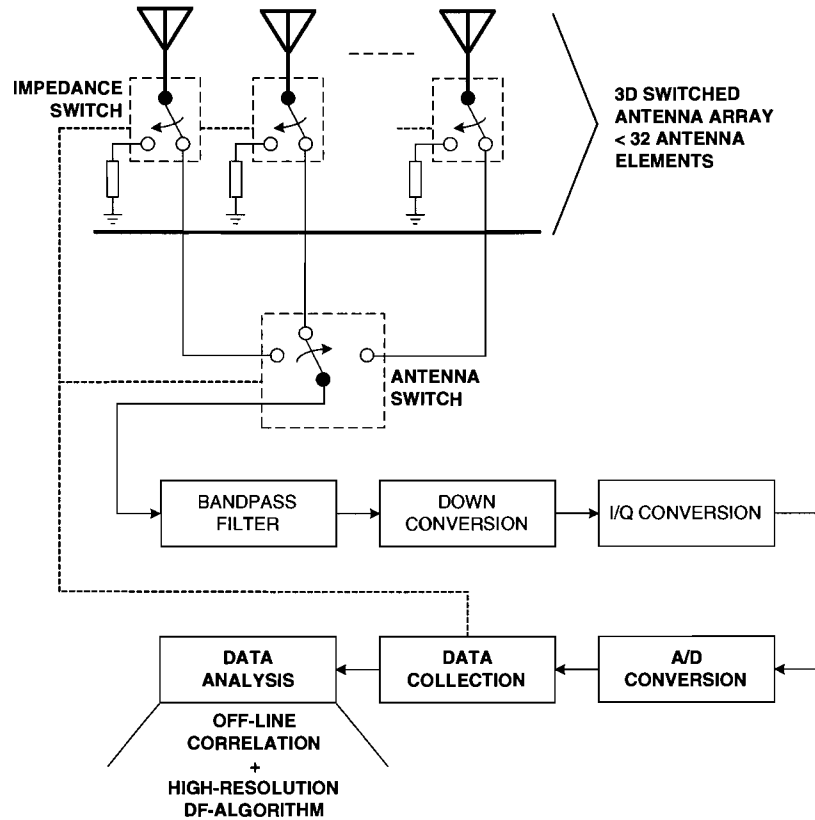


Figure 2.4: Receiving side of the new TU/e wideband radio channel sounder.

To improve the elevation resolution, a new antenna array will be developed that instead of planar, will be three-dimensional. The goal is to achieve an angular resolution that is equal in azimuth as well as in elevation, and still equal or better than the azimuth resolution of the current system. In contrast to the *synthetic* circular array, the new array will be a switched antenna array that consists of maximum 32 actual antenna elements. All antenna

elements in the array will be addressed in sequence by a RF-switch that connects each of the elements to the input of the receiver and is addressed by the data collection system.

A well known major problem with having multiple antenna elements positioned in close proximity of each other is that electromagnetic coupling between the elements occurs. In the switched antenna array, only one antenna element is active at a time, while all the other elements are passive. Terminating the passive elements in the 50Ω system impedance would cause a major coupling effect between the elements, since the elements are tuned at the same frequency. To suppress this coupling effect, an impedance switching technique is used in which the passive elements are switched to a specific impedance to make them less "visible" for the active antenna.

To achieve a higher measurement speed, which is needed to perform mobile measurements, the total range of the CIRs is decreased to $5.1\mu s$ (255 bits of 20ns each), which is still expected to be sufficient. Furthermore, the correlation in the new system will no longer be done in hardware. Instead, the receiver signal is sampled directly, and then correlated off-line. This requires faster data acquisition compared to the current system, which means the A/D convertor and the data collection system need to be upgraded as well.

To perform high-resolution DOA estimation, a suitable algorithm will be used that fits with the new 3-D antenna array and is capable of performing Df in azimuth and elevation. Additionally, signal processing techniques can be used to improve the estimation results.

Chapter 3

Antenna array configuration

3.1 Introduction

The overall performance capabilities of a DF system are in the first place determined by the choice of the geometry of the antenna array. This makes it obvious to start the design of a DF system by determining the most suitable antenna array geometry.

To create an antenna array with high-resolution properties, the overall size of the array, named the aperture, has to be large. In contrast, the array elements have to be placed sufficiently close to each other to prevent grating lobes (side-lobe-levels (SLLs) equal to the main lobe level) from occurring in the radiation pattern. Furthermore, the shape or geometry of the antenna array has a great influence on the uniformness in performance of the array. Having only a limited number of antenna elements available, this means that several trade-offs have to be made in the design of an suitable antenna array for DOA estimation.

A variety of array designs can be found in the literature that are used for DOA estimation [4–7]. The linear array is the simplest and most obvious design, although it has disadvantages regarding the uniformness in performance and the limitation of performing only one dimensional estimations. Planar antenna arrays solve this one-dimensional restriction and are capable of estimating DOAs in azimuth and elevation. From a design perspective, planar arrays are more interesting because they give the designer more degrees of freedom to come to an "optimal" design. A very well known and often used planar array design is the circular array. This array has drawn much attention because of its uniformity in azimuth performance [5]. In the next sections, the circular array will be used as a reference to compare other array designs.

Although horizontally positioned planar arrays are capable of estimating DOAs in azimuth as well as in elevation, the resolution at low elevation angles (between -20 and 20 degrees) is often poor. Also, planar arrays suffer from the ambiguity of being unable to distinguish waves coming from either positive or negative elevation angles. To improve the resolution in elevation and to solve the two-fold ambiguity, the array design has to be transposed into the third dimension. From a circular array point of view, an obvious candidate for such an array would be a cylindrical or spherical array [4]. One of the disadvantages however is the number of antenna elements that are needed to cover an entire sphere or cylinder with a reasonable aperture. Therefore other array geometries have to be investigated that can effectively perform two-dimensional DOA estimations with only a limited number of antenna elements.

A well known, major problem with antenna arrays is the electromagnetic coupling be-

tween the elements in the array, often referred to as mutual coupling. This mutual coupling phenomenon affects the amplitude and phase of the radiation pattern and the input impedance of the antenna elements. The effect becomes significant as the interelement spacing is decreased and can be rather drastic if the interelement spacing drops below half a wavelength [8]. Since ignoring the presence of mutual coupling will degrade the array performance, techniques that minimise the mutual coupling effects are vital. Theoretically, it is possible to eliminate the effects of mutual coupling by correcting the voltages at the terminals of the array elements by using an impedance matrix [3,9]. In order to avoid significant performance degradation, this correction matrix must be very accurately known over the entire system bandwidth, which can be a great challenge in practice.

In [2], an impedance switching technique is described that can suppress the mutual coupling effects in switched antenna arrays. From simulations on a two element antenna array, it is shown that by terminating the passive antenna with an inductive load, instead of the system impedance of 50Ω , the mutual coupling effects can virtual be eliminated. To reduce the mutual coupling effects in antenna array configurations with more than two elements, this impedance switching technique may be very promising and therefore has to be investigated on different array geometries.

In this chapter, several antenna array designs are discussed. The Y-shaped array geometry with uniform and non-uniform element separation is used as a basis in the design of a three-dimension antenna array. Next, an impedance switching technique is discussed that can minimise the mutual coupling effects between the antenna elements in an array configuration. After that, simulations are performed using MATLAB to investigate the DF performance of the different array geometries. The effect of the impedance switching technique on the antenna elements in the different array configurations is investigated by performing simulations using an EM modelling tool called FEKO. Finally, the chapter will be concluded.

3.2 Uniform circular array design

The uniform circular array is the only planar array geometry where the performance in the azimuth plane is independently of azimuth angle, ϕ , [5]. Because of this uniform performance the circular array is often used in DF systems. The circular array presented here will mainly be used as a reference design to compare the performance of other array designs. The circular antenna array visualised in figure 3.1 consist of 31 elements that are uniformly spaced at a distance of $\delta = 0.5\lambda$, where the wavelength is defined as $\lambda = \frac{c}{f}$, with c the speed of light and f the frequency of the radio signal. To obtain an equal comparison between the different array geometries and because the other array geometries presented in this chapter are limited to 31 elements, the number of elements in the circular array is chosen to be 31. Spacing the elements at a maximum distance $\delta = 0.5\lambda$ minimizes the number of grating lobes in the antenna radiation pattern [10], which can otherwise lead to spurious DOA estimates. The angular estimation accuracy and the resolution are two important performance criteria that improve with increasing array dimensions. Therefore the aperture can give a first indication of the performance capabilities of an antenna array. The azimuth aperture of the uniform circular array can be determined as

$$d = 2r = 2 \left(\frac{31}{4\pi} \right) = 4.93\lambda. \quad (3.1)$$

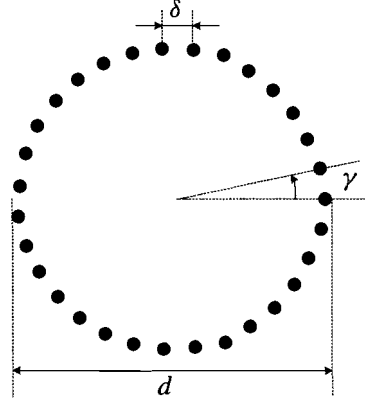


Figure 3.1: Uniform circular antenna array, with the black circles indicating the antenna element positions.

3.3 Y-shaped array design

The Y-shaped antenna array has recently drawn some attention because of its unique properties [7, 11]. Compared to other planar array structures such as the L, X and T shaped arrays the Y-shaped antenna array holds the best DF performance capabilities [5]. Due to its unique shape the Y-shaped antenna array exhibits the largest array aperture when the same number of elements are used [7]. This section discusses an uniformly spaced and a non-uniformly spaced version of the Y-shaped array.

3.3.1 Uniform element spacing

The uniformly spaced 31 element Y-shaped array is visualised in figure 3.2. The array consist out of three 11 element linear arrays with a shared centre element and are rotated 120° around the centre.

It is known that to prevent grating lobes from appearing in the radiation pattern, the element spacing in a linear array needs to be a little less than 0.5λ [12]. Since the Y-shaped array is composed out of three linear arrays the same condition holds. The new element separation distance δ can be determined using the Hansen-Woodyard condition [12] as

$$\delta = \frac{\lambda}{2} \left(1 - \frac{1}{N_Y} \right) \quad (3.2)$$

with N_Y being the number of elements on one of the three array arms. Since the three arms share the same centre element, this means that $N_Y = 11$ and $\delta = \frac{5}{11}\lambda$.

With $l = \delta(N - 1)$ and $\gamma = 120^\circ$ it can be seen from figure 3.2 that the azimuthal aperture of the uniform Y-shaped array varies six times over the entire azimuth range between

$$d_1 = \frac{2l \cos(30^\circ)}{\lambda} = 7.87\lambda, \text{ and} \quad d_2 = \cos(30^\circ)d_1 = 6.82\lambda.$$

3.3.2 Non-uniform element spacing

Non-equally spaced linear arrays have some advantages over equally spaced linear arrays when used in DF systems. As a result of the unequal spacing, fewer elements are needed

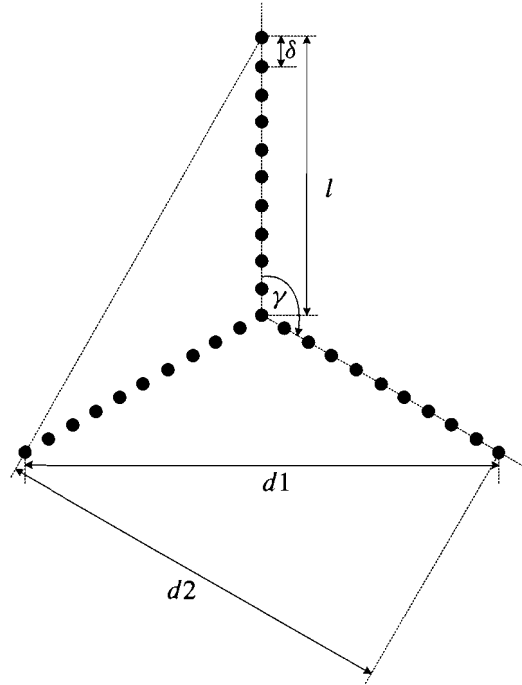


Figure 3.2: Uniform Y-shaped antenna array configuration.

to create a certain aperture compared to the equally spaced array. The result is that very accurate estimations are possible at a relatively low cost. Placing the elements further apart also decreases the mutual coupling between the elements, which is very helpful in determining accurate estimates. Because the Y-shaped array is composed out of three linear arrays, non-uniform spacing can be applied in a similar way as with linear arrays.

The disadvantage of unequally spacing is that high side-lobes, or even grating lobes may occur, which can lead to spurious estimates. By changing the exact locations of the antenna elements it is however possible to find a configuration with the lowest SLLs [13].

There is no straightforward solution in determining the optimal sensor positions in a non-uniform linear array. This is caused by the fact that the SLLs depend on the elements positions in a highly non-linear manner, and that in general there is no analytical method to determine the highest SLL, or the angular direction where the highest SLL may occur. Therefore, in many cases, an array geometry is created empirical, then analyzed and adopted to come to an optimal array. A number of optimisation techniques for determining or optimizing the sensor positions of an array are found in the literature [13–19]. Many of these techniques have one common drawback, the computational complexity of the search. This complexity can be decreased by using discrete sensor placements and by limiting the total size of the array.

The Dynamic Programming technique described by Skolnik [14], proved to be computationally efficient in determining the "optimal" sensor placements in a non-uniform array. The technique determines solutions which approximate the optimum configuration of elements spacings for achieving a radiation pattern with the lowest SLLs, however, the degree of approximation to optimum is unknown. It does this by converting a single N -dimensional optimisation problem into a sequence of N one-dimensional optimisation problems. Simulations showed that the result of lowering the SLLs by optimised non-uniform element

positioning resulted in a more uniform distribution of the SLLs over the entire radiation pattern.

To limit the complexity of the search, a sensor placement grid of 0.1δ was chosen and the total size of the array was limited to 12δ . This maximum array size results from the maximum available area on top of the measurement van. Using the Dynamic Programming technique to determine the optimal sensor positions that have the lowest SLLs, results in the non-uniform sensor placement shown in figure 3.3.

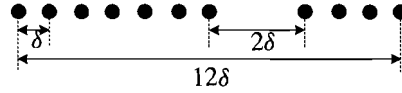


Figure 3.3: Non-uniform element spacing of one of the 3 arms in the Y-shaped antenna array design, the leftmost element is positioned in the centre of the array.

This non-uniform Y-shaped array geometry is in fact an uniform Y-shaped array with its outer four elements on each of the array arms shifted two positions outward. With $l = 12\delta$, the aperture varies between $d_1 = 9.45\lambda$ and $d_2 = 8.18\lambda$.

3.4 3-D tilted cross array design

In this section, the Y-shaped array geometry is used as a starting point in creating a three-dimensional array structure. Similar as to the Y-shaped array, non-uniform element spacing is applied as well.

3.4.1 Uniform element spacing

To achieve more elevation resolution at low elevation angles, it is a necessary requirement that the array geometry is extended into the third dimension. A way to extend the uniformly spaced Y-shaped array into the third dimension is to move the centre of the array into the z direction to create a pyramid-shaped array, as visualised in figure 3.4.

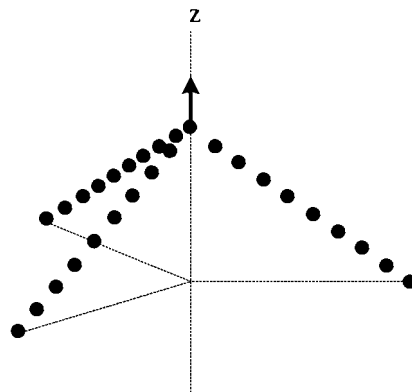


Figure 3.4: Extending the Y-shaped planar array into the third dimension.

This array clearly shows an increase in elevation aperture at low elevation angles. While this array design satisfies the requirement for more resolution in elevation, it does not satisfy

the centro-symmetry property, which is one of the requirements for using a promising high-resolution DF algorithm called Unitary ESPRIT, which will be explained in more detail in the next chapter.

Expanding the array design from figure 3.4 further, it is possible to create a 3-D array design that does satisfies the centro-symmetry requirement. The new array design is constructed by virtually extending the three arms of the pyramid array as shown in figure 3.5. The resulting 3-D array structure is a 3-D cross array that is tilted 45° around the x-axis and 35.26° around the y-axis, which results in the three legs ending in the same xy-plane. One disadvantage of this array however, is that the azimuth aperture has become half the size of the array shown in figure 3.4.

Similar as with the uniformly spaced Y-shaped array the elements are spaced according to the Hansen-Woodyard condition at $\delta = \frac{5}{11}\lambda$.

The azimuth aperture with this three-dimensional array varies between $d_1 = 3.21\lambda$ and $d_2 = 2.78\lambda$.

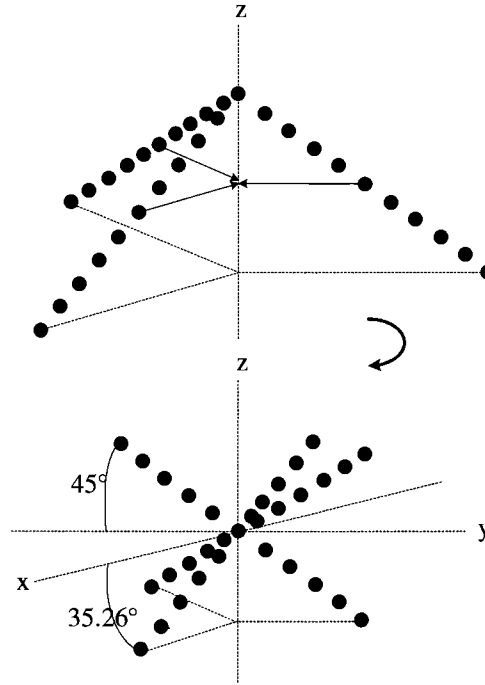


Figure 3.5: Extension of the pyramid shaped array to form a 3-D tilted cross array.

Instead of using a tilted 3-D cross array, it would be more straightforward to use a non-tilted 3-D cross array, since it also satisfies the centro-symmetry requirement. However, tilting the array geometry gives it some interesting advantages in the performance. As mentioned before, most incident waves will arrive at relatively low elevation angles ($\theta < 20^\circ$). One advantage of tilting the array is that the DOA performance in low elevation angles will be more uniform. An other advantage is that in the case of low SNR levels, large errors in the estimation will mainly occur at elevation angles higher than 30° . This is caused by the fact that the location of possible grating lobes are shifted upward in elevation, whereas with the 3-D cross array these locations would occur around 0° elevation. Simulation results in section 4.4.3 clearly confirm this effect.

3.4.2 Non-uniform element spacing

To increase the aperture for more resolution in the DOA estimation, similar as with the Y-shaped array the elements in the 3-D tilted cross array are spaced in a non-uniform order. The possible element positions are limited by a 0.05λ sensor placement grid as well as by placing one element in the centre and an placing an other element at 10λ on each of the arms. Again, the maximum array size is determined from the maximum area available on top of the measurement van. Having only four elements left to be placed at the grid points, only a limited number of calculations are needed to search all possible locations to find the optimal position of the elements. Therefore, instead of using an optimisation technique, the limited complexity of the search allows the use of an exhaustive search to determine the optimal sensor positions that correspond to a radiation pattern with the lowest possible SLLs. The resulting element spacing in each of the arms of the non-uniform 3-D tilted cross array is shown in figure 3.6. In this case, the azimuth aperture varies between $d_1 = 6.42\lambda$ and $d_2 = 5.56\lambda$.

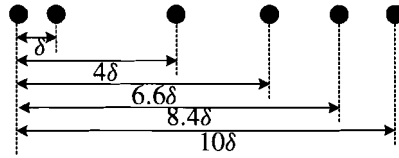


Figure 3.6: Non-uniformly element spacing of one of the 6 arms in 3-D tilted cross antenna array, the leftmost element is positioned in the centre of the array.

3.5 Impedance switching

This section describes the impedance switching technique that can suppress the mutual coupling effects between the array elements and refers to [2].

Mutual coupling is well-known to be the result of displacement currents induced in the passive antennas due to the current that flows in the active antenna. In general, mutual coupling is strong if the passive antennas are nearby and of resonant size, i.e. if they have similar dimensions. The distances between the antenna elements are imposed by design considerations as described in the previous sections, and the minimum antenna spacing can usually not be made larger than half the wavelength. The electric dimensions of the passive antennas, however, can be changed through the impedance in which their feedpoints are terminated. The result of changing the impedance of the passive antennas is that the current distribution of the active antenna does not match the electrical length of the passive antenna. Therefore, the current distribution in the passive antennas becomes small, and considerable suppression of mutual coupling can be achieved.

As an example, consider a two-element antenna array, shown schematically in figure 3.7. This array consists of two half-wavelength dipole antennas. One of the antennas is driven by a narrowband voltage signal through a $50\text{-}\Omega$ transmission line, the other element is passive. The thin lines in this figure represent the envelopes of the current distributions along the wires. In figure 3.7 (a) the passive element is short-circuited, and is resonant at the same frequency as the active dipole. This causes a considerable current to be induced in the passive dipole, which will effect the input impedance and radiation pattern of the

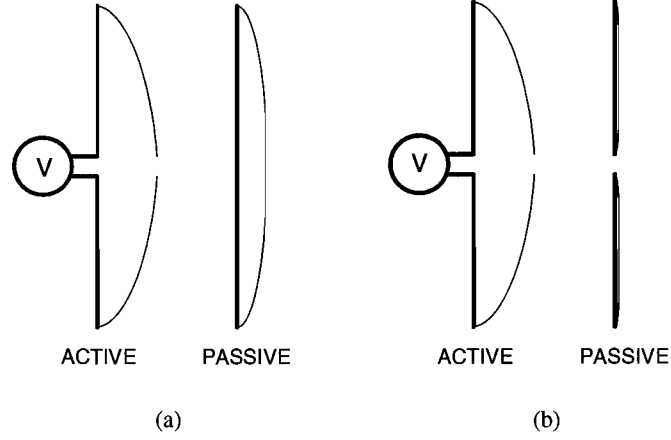


Figure 3.7: Current distributions in two nearby dipole antennas, with the passive antenna (a) short-circuited and (b) open-circuited.

active antenna. In figure 3.7 (b), the dipole is terminated in an open circuit, so that it becomes identical to two separate quarter-wavelength wires. Now, the current distribution of the active antenna does not match the lengths of the wires of the passive antenna and the induced current in the passive antenna, and therefore the effect of the mutual coupling will be minimal.

In [2], different values of the termination impedance of the passive antenna were considered. Using the drooping-radial monopole antenna as described in appendix B, an impedance of $j250\Omega$ was found by trial and error to be the best result and to virtually eliminate the mutual coupling effects.

Since the new channel sounding system only passes a single antenna signal to the receiver at a time, the other elements in the array are passive, and can be terminated in $j250\Omega$ to reduce the mutual coupling effects. In the next section simulations are performed to investigate the impedance switching technique in the different array configurations.

3.6 Performance comparison

To compare the performance of the different antenna array designs presented in the previous sections, the array designs are implemented in Matlab code and in the EM simulation tool called FEKO, and subsequently simulations are performed.

Simulations in Matlab are performed to get an idea of the overall array performance. In these simulations the antenna elements are assumed to have an omni-directional antenna pattern and no mutual coupling effects are included. These simulations are discussed in section 3.6.1.

The FEKO simulation software, described in section 3.6.2, is used to investigate the mutual coupling effects between the antenna elements using the impedance switching technique described in section 3.5. The results of these simulations are presented in section 3.6.3.

3.6.1 Array performance

In table 3.1 the azimuth apertures of the different array designs are summarised to give a first impression of the DF capabilities. It can be seen that compared to the circular array the Y-shaped array geometry significantly enlarges the aperture, especially when non-uniform element spacing is used. As a result the aperture of the Y-shaped array exhibits a minor six-fold variation in the DOA estimation performance. Due to its extension into the third dimension, the 3-D tilted cross array shows a smaller azimuth aperture. This change in azimuth resolution can be attributed to the increased resolution in elevation. Using non-uniform element spacing the aperture of the 3-D-tilted cross array can be enlarged, although this can result in higher SLLs as will be seen later.

Table 3.1: Azimuth aperture size, measured in wavelengths, of different array geometries with each having 31 antenna elements.

Array Geometry	Azimuth aperture (in wavelengths)
	max. / min.
Circular	4.93 / 4.93
Uniform Y-shaped	7.87 / 6.82
Non-uniform Y-shaped	9.45 / 8.18
Uniform 3-D tilted cross	3.21 / 2.78
Non-uniform 3-D tilted cross	6.42 / 5.56

To investigate the overall DF performance capabilities of the antenna array designs more closely, a technique called beam-forming is used. The beam-forming technique is based on applying different phase shifted signals to each of the N antenna elements in such a way that the signals add up coherently for a given direction in space. The applied phase shift ζ_n for each element can be determined from multiplying $\beta = \frac{2\pi}{\lambda}$ with the projection of the element position vector $\mathbf{p}_n(r_n, \theta_n, \phi_n)$ onto the vector $\mathbf{k}(1, \theta, \phi)$ that points into the desired main-beam direction, as visualised in figure 3.8.

Using the coordinate system as defined in figure 3.8 and knowing the exact sensor positions, the resulting phase shift for having the main beam pointed in a specific direction can now be determined as,

$$\begin{aligned}
 \zeta_n &= \beta (\mathbf{k} \bullet \mathbf{p}_n) \\
 &= \beta r_n (\cos \theta \cos \phi \cos \theta_n \cos \phi_n + \cos \theta \sin \phi \cos \theta_n \sin \phi_n + \sin \theta \sin \theta_n) \\
 &= \beta (x_n \cos \theta \cos \phi + y_n \cos \theta \sin \phi + z_n \sin \theta)
 \end{aligned} \tag{3.3}$$

By implementing the array designs presented in the previous sections in Matlab-code and by applying the beam-forming technique, it is possible to create three-dimensional antenna radiation patterns with the main beam of the antenna pattern pointed in a specific direction. The 3-D antenna array pattern can be analysed on specific properties such as the half-power-beam-width (HPBW) and the side-lobe-level (SLL) that will give a better indication of the performance capabilities of the array geometries. Figures 3.9 to 3.11 show the

three-dimensional radiation patterns in dB's of the different array geometries with beam-forming applied to the elements. In all cases the main beam is pointed at $\phi = 20^\circ$ azimuth and $\theta = 20^\circ$ elevation.

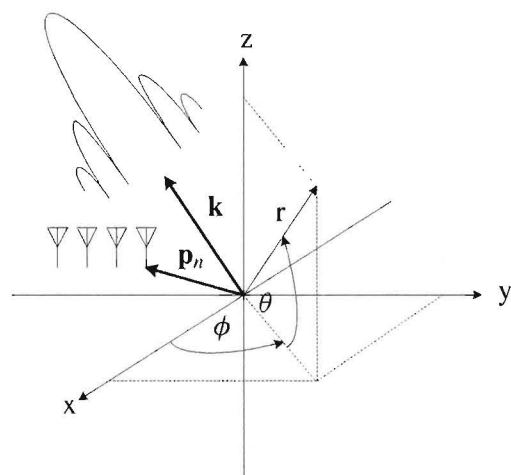


Figure 3.8: Beamforming applied to an antenna array.

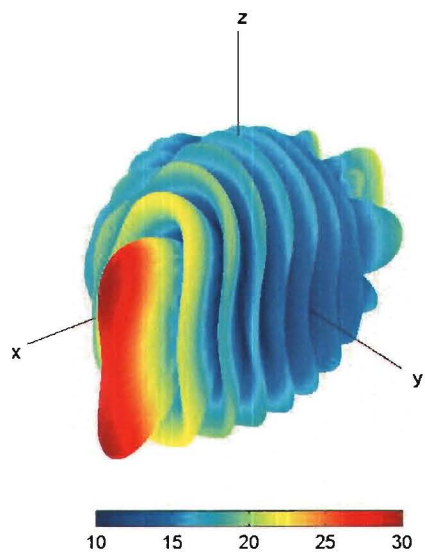


Figure 3.9: 3-D radiation pattern of the circular array with beam-forming applied to the elements.

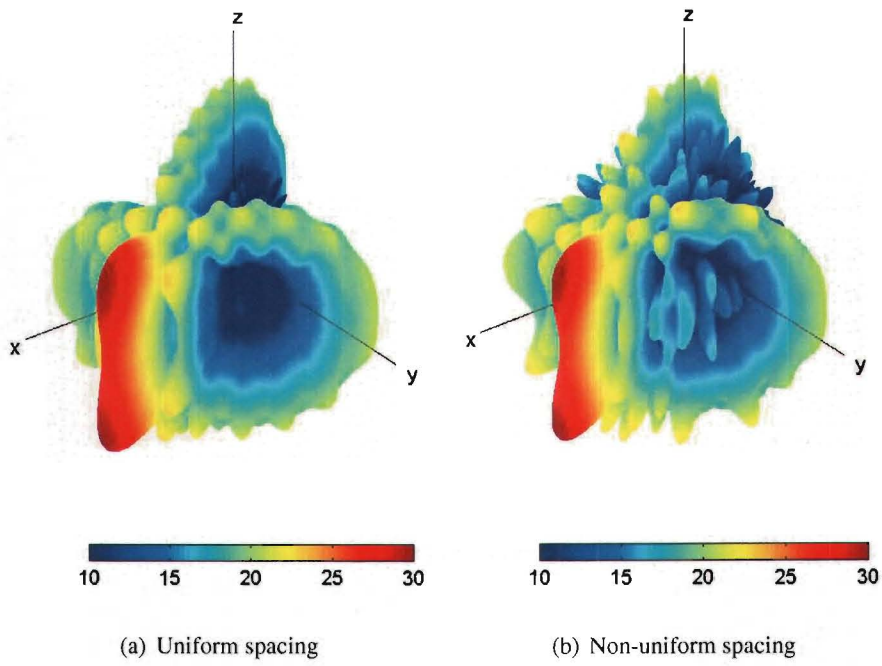


Figure 3.10: 3-D radiation pattern of the (a) uniform and (b) non-uniform Y-shaped array with beam-forming applied to the elements.

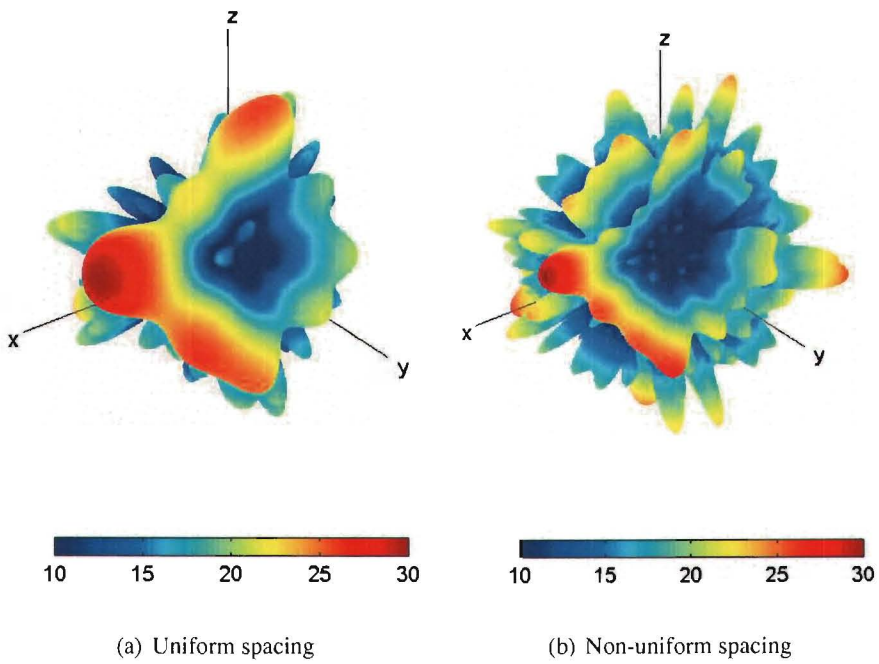


Figure 3.11: 3-D radiation pattern of the (a) uniform and (b) non-uniform 3-D tilted cross array with beam-forming applied to the elements.

From these figures the two-fold ambiguity between the positive and negative elevation angles is clearly visible with the planar arrays as a grating lobe in the negative elevation area, whereas with the 3-D arrays this ambiguity has disappeared. Also, the poor resolution in elevation can be observed with the planar arrays.

To investigate the performance of the different arrays over the *entire* azimuth and elevation range, the main beam of the antenna pattern is scanned over all azimuth ($0 - 360^\circ$) and nearly all elevation angles ($-80 - 80^\circ$) and the HPBW and SLLs are determined. The results of these simulations are summarised in figure 3.12 and 3.13.

These simulation results also confirm the poor resolution in elevation and the ambiguity problem with the planar arrays. It is also shown that compared to the uniform circular array, an uniform Y-shaped antenna array with the same number of elements, can improve the HPBW with a small increase in the sidelobe levels. In the case of 31 elements, the azimuth HPBW improves from 8 to 6 degrees, while the SLLs increase 1dB.

Comparing the uniform and the non-uniformly spaced arrays, it can be seen that it is possible to create even more resolution by spacing the elements non-uniformly, although this results in higher SLLs with more variation over the entire range, which can be seen by comparing the maximum and average SLLs.

Looking at the 3-D tilted cross arrays, the elevation resolution is improved significantly and has become much more uniform over the entire range. Also the elevation resolution is equal to the azimuthal resolution over the entire range. The cost of the 3-D configuration however is that beam broadening in azimuth has occurred and the SLLs have increased and are not as constant as with the planar arrays.

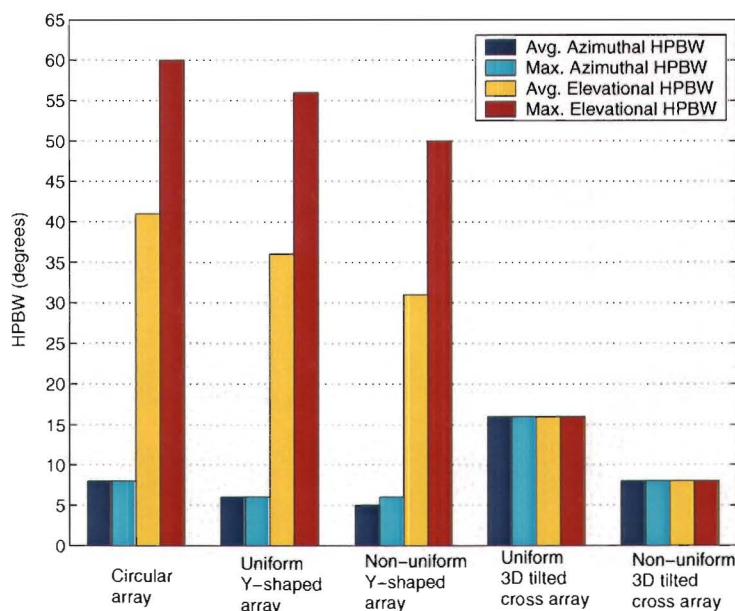


Figure 3.12: Simulation results of the average and maximum values of the azimuthal and elevational HPBW for the different array geometries.

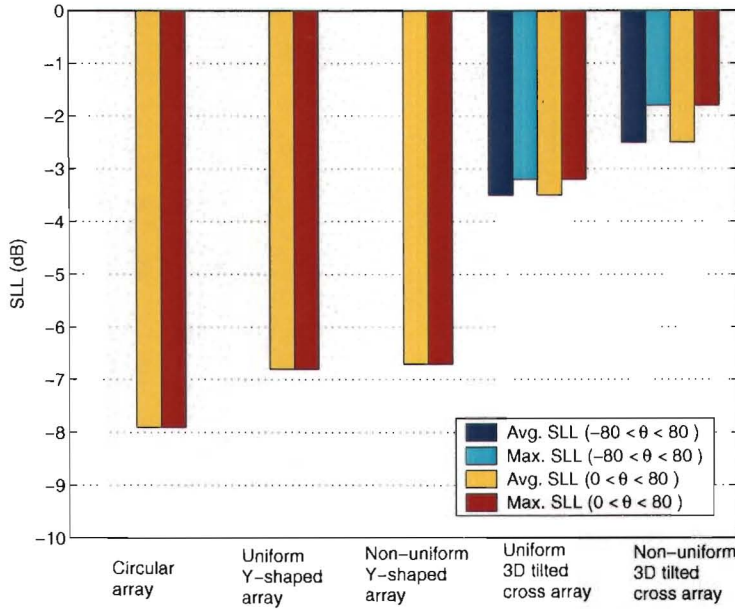


Figure 3.13: Simulation results of the average and maximum values of SLL over the entire range ($-80 < \theta < 80$), and the positive hemisphere ($0 < \theta < 80$) for the different array geometries.

3.6.2 Description of the FEKO EM simulation software

The FEKO EM simulation software [20] can be used for various types of electromagnetic field analysis involving metallic or dielectric objects of arbitrary shapes. The software is based on the methods of moments (MoM), which means that the electromagnetic fields are obtained by first calculating the electric surface currents on conducting surfaces and the equivalent electric and magnetic surface currents on the surfaces of dielectric objects. The currents are calculated using a linear combination of basis functions, where the coefficients are obtained by solving a system of linear equations. From the current distribution, further parameters can be obtained, such as the far field radiation pattern or input impedance of antennas. The objects in the software are modelled as consisting of wires subdivided into segments, and surfaces subdivided into triangles. Only harmonic sources are supported by the software, and consequently calculation is done in the frequency domain.

3.6.3 Element performance

In [2], it is shown that the mutual coupling effects between an active and passive drooping-radial monopole antenna positioned in close proximity of each other can be suppressed by terminating the passive antenna with a complex load of $Z_L = j250\Omega$. In order to investigate this effect on the elements in an array configuration, the different array geometries are implemented in FEKO and simulations are performed. The array configurations are modelled in FEKO using the drooping-radial monopole antenna as defined in appendix A.1. This type of antenna has been used previously at both CRC and TUD; for example see [2, 3]. Figure 3.14 shows the FEKO models of the circular and the 3-D tilted cross array, the elements indicated with a circle are used to produce simulation results presented next.

Simulations are performed in which one antenna element at a time is excited with a unit-

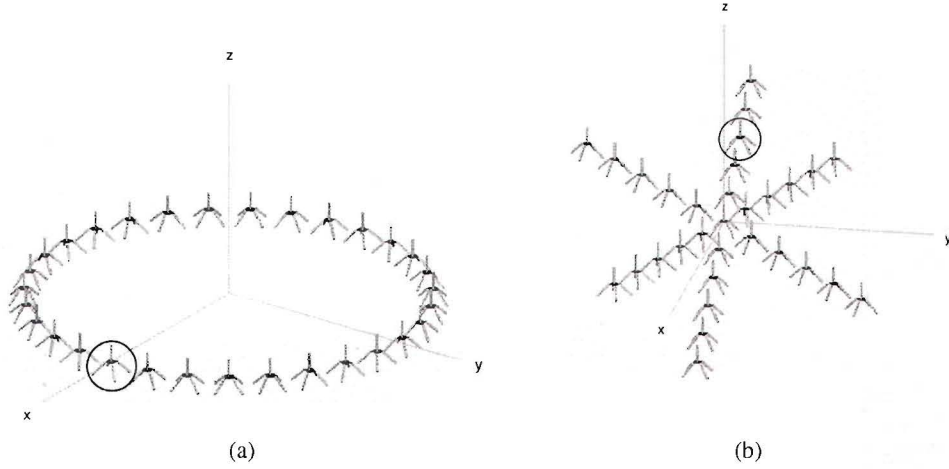


Figure 3.14: FEKO model (a) of the circular and (b) the 3-D tilted cross array.

amplitude harmonic voltage, while the other 30 elements are terminated in either the system impedance of $Z_L = 50\Omega$ or in $Z_L = j250\Omega$. The effect of terminating the inactive antennas with a complex load is investigated by analysing the antenna element radiation and phase pattern and the input reflection (S11). First, simulation results of the circular array and the uniform 3-D tilted cross array are presented in which one element is excited (indicated with a circle in figure 3.14) while the others are terminated. After that, a summary of the results of all elements in all array geometries is presented and comparisons are made. More details on the simulation results can be found in appendix B.

The simulation results of the circular array are shown in figure 3.15, 3.16 and 3.17, which show the azimuth antenna radiation and phase pattern and the input reflection of one of the elements in the array with $Z_L = 50\Omega$ and $Z_L = 250j\Omega$ loading on the passive elements. The results clearly show the performance improvement when using a $j250\Omega$ load at the passive elements in an antenna array. The frequency dependency in the radiation pattern decreases and the distortion on the pattern is improved with more than 2dB. The phase error decreases from more than 35 degrees to approximately 5 degrees and the input reflection also improves significantly.

The simulation results of the 3-D tilted cross array are shown in figure 3.18, 3.19 and 3.20, which show the azimuth antenna radiation and phase pattern and the input reflection of one of the elements in the array with $Z_L = 50\Omega$ and $Z_L = j250\Omega$ loading on the passive elements.

Although these results are less dramatically as with the circular array, there is still a performance improvement when using a $j250\Omega$ load at the passive elements in the antenna array. The distortion on the pattern is improved with approximately 2dB and the phase error is decreased from 25 degrees to approximately 12 degrees. The input reflection shows some improvement as well.

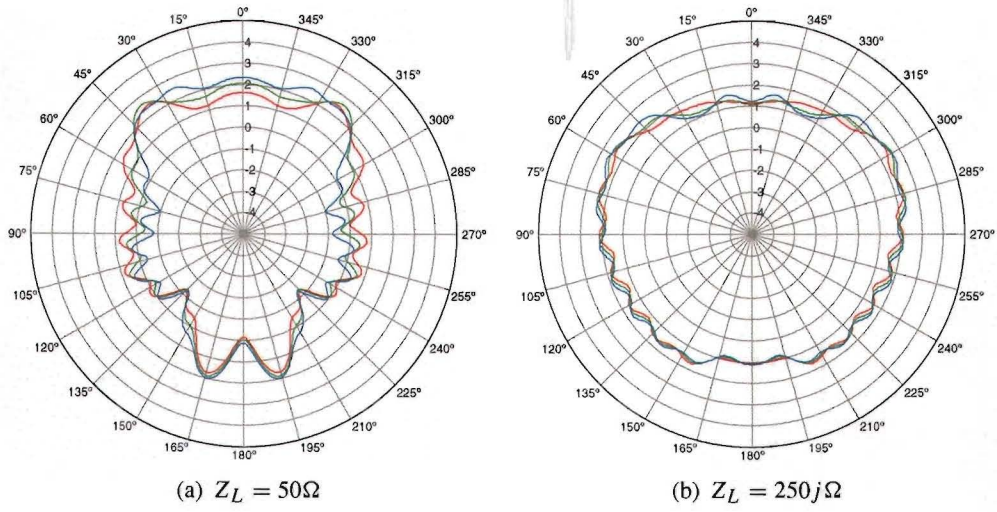


Figure 3.15: H-plane pattern of one of the elements in the circular array at 2200MHz (red), 2250MHz (green) and 2300MHz (blue) with (a) $Z = 50\Omega$ and (b) $Z = j250\Omega$.

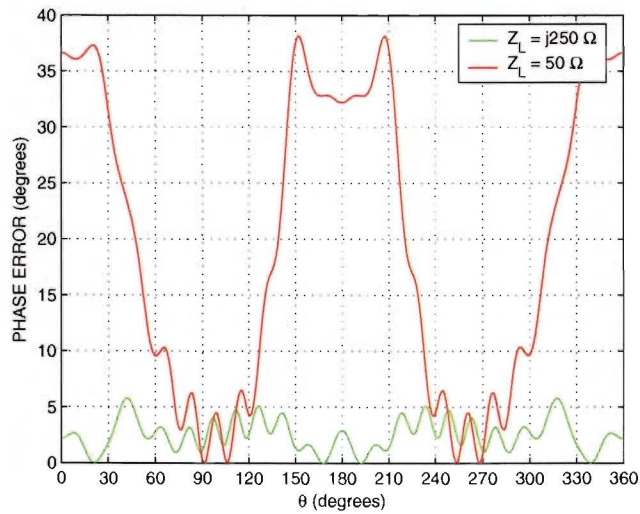


Figure 3.16: Phase error of one of the elements in the circular array with $Z_L = 50\Omega$ (red) and $Z_L = j250\Omega$ (green).

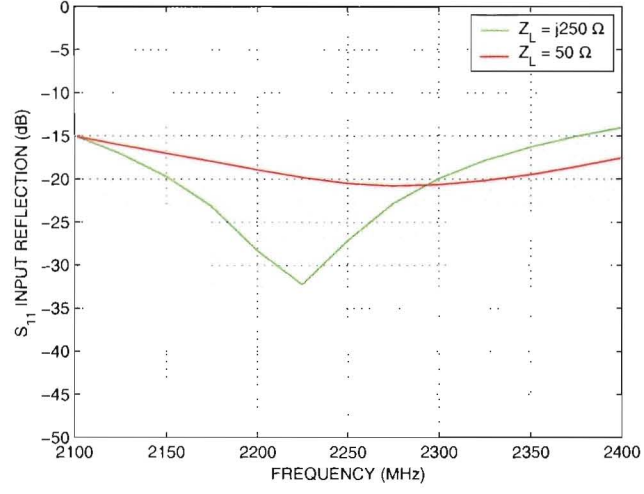


Figure 3.17: Input reflection of one of the elements in the circular array with $Z_L = 50\Omega$ (red) and $Z_L = j250\Omega$ (green).

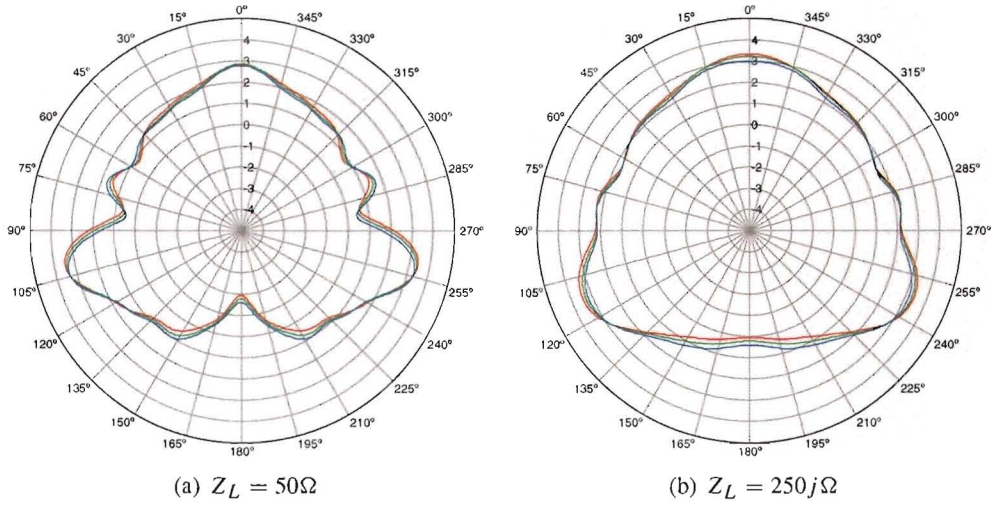


Figure 3.18: H-plane pattern of one of the elements in the uniform 3-D tilted cross array at 2200MHz (red), 2250MHz (green) and 2300MHz (blue) with $Z_L = 50\Omega$ (a) and $Z_L = j250\Omega$ (b).

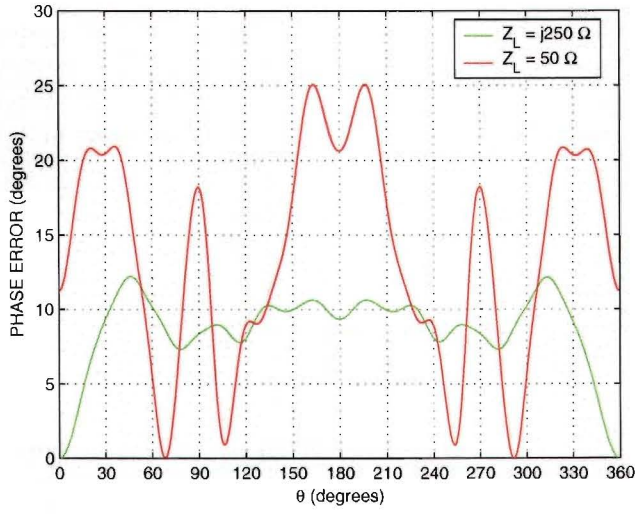


Figure 3.19: Phase error of one of the elements in the 3-D tilted cross array with $Z_L = 50\Omega$ (red) and $Z_L = j250\Omega$ (green).

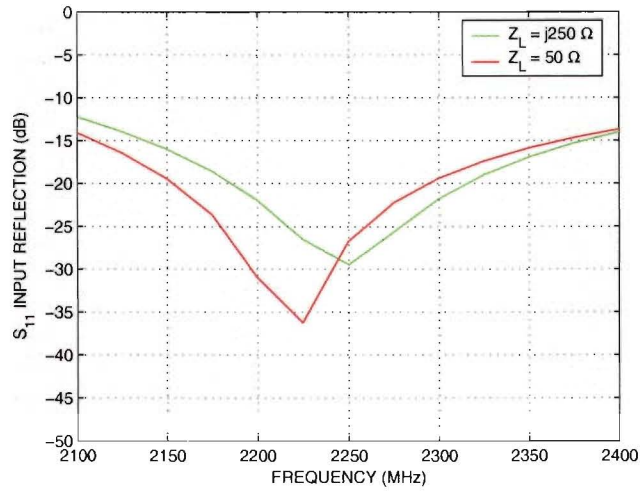


Figure 3.20: Input reflection of one of the elements in the 3-D tilted cross array with $Z_L = 50\Omega$ (red) and $Z_L = j250\Omega$ (green).

Similar simulations are performed on all elements in all array geometries and a summary of the results are presented in figure 3.21, 3.22 and 3.23. Figure 3.21 shows the maximum distortion on the antenna element radiation pattern in the different array geometries. The results show a significant improvement with the uniform Y-shaped array, where as with the other arrays the improvement is less, but still large. The results in figure 3.22 show the maximum phase error. It can be seen that especially with the planar arrays large improvements can be made, but in all cases the phase error can be improved. The input reflection of the antenna elements is shown in figure 3.23. Although less noticeable, in most cases the input reflection improves with the use of the complex impedance loading. For more details on these simulation results the reader is referred to appendix B.

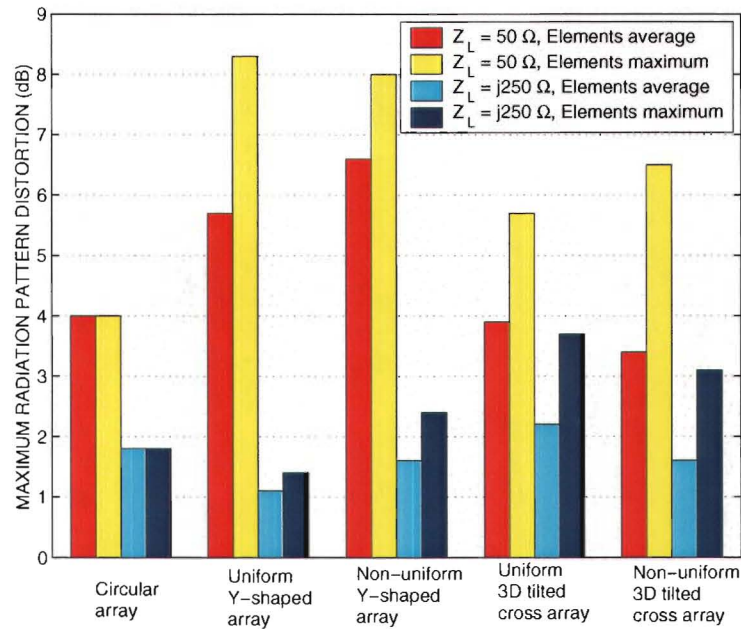


Figure 3.21: Summary of the simulation results of the maximum element pattern distortion for different array geometries.

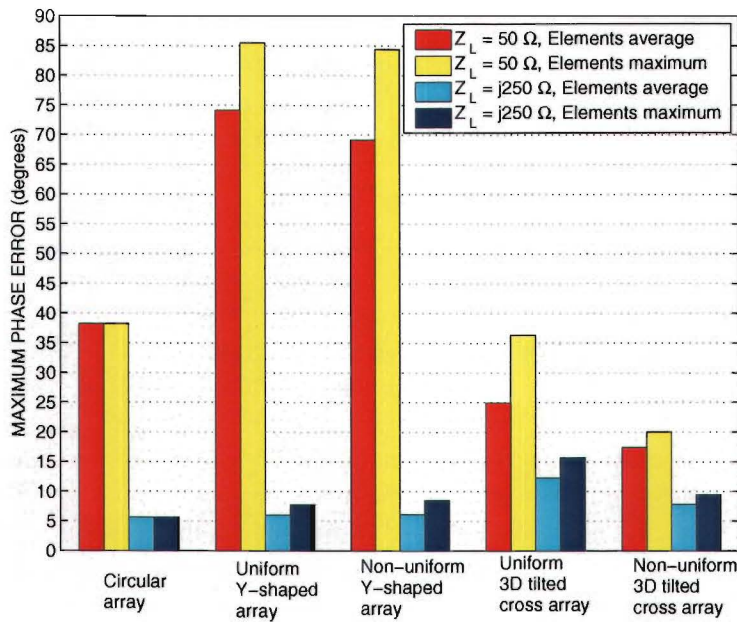


Figure 3.22: Summary of the simulation results of the maximum element phase error for the different array geometries.

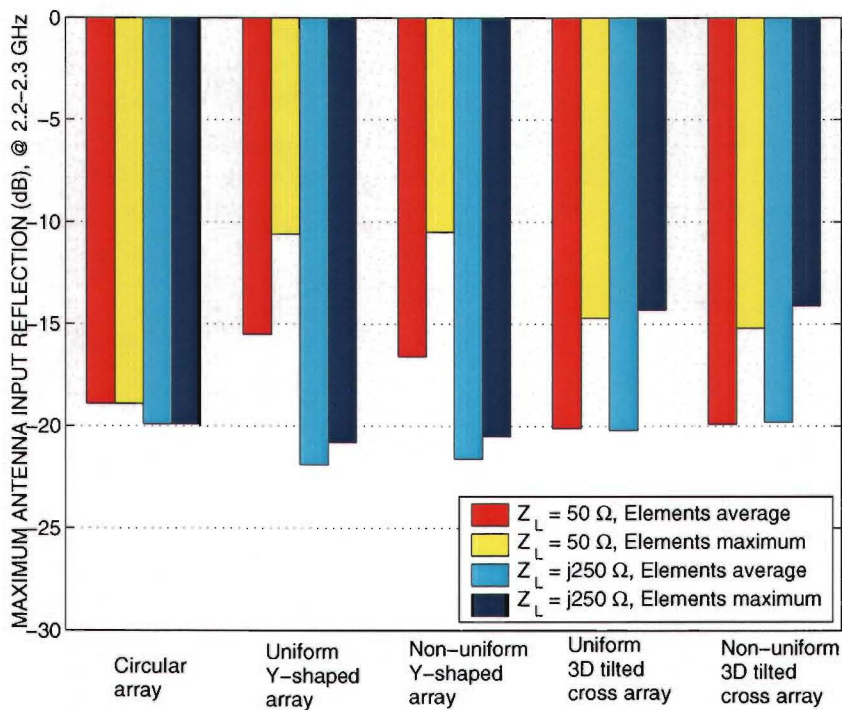


Figure 3.23: Summary of the simulation results of the maximum antenna element input reflection for the different array geometries.

3.6.4 Conclusion

In this chapter it is shown that the horizontally positioned Y-shaped antenna array can provide better resolution with the same number of elements as compared to the UCA. The azimuth HPBW of the Y-shaped array is decreased to six degrees compared to eight degrees of the UCA.

Applying non-uniform element positioning makes it possible to extend the aperture, while minimising the number of grating lobes and maintaining low SLLs. Because there is no straightforward solution in determining the non-uniform element positions, optimisation techniques such as Dynamic Programming can be used to find the optimal positions.

It is confirmed that horizontally positioned planar arrays have a two-fold ambiguity in the elevation estimation and that the resolution in elevation is very poor, i.e. the HPBW lies somewhere in the order of thirty to fifty degrees.

To solve this problem the Y-shaped planar array is extended to the third dimension to form a 3-D tilted cross array, which is capable of performing unambiguous DOA estimates over the entire azimuth and elevation range with equal resolution. The elevation HPBW improves to about sixteen degrees. The cost of improved elevation resolution however is a decrease of azimuthal resolution from six to sixteen degrees and an increase of the SLLs of about 3dB. From all array geometries presented in this chapter, the uniform 3-D tilted cross array proves to be the only geometry that is suitable for the Unitary ESPRIT algorithm, because of its uniform spacing and centro-symmetry properties. The Unitary ESPRIT algorithm applied to this array will be discussed in the next chapter.

Using the FEKO EM simulation package, it is shown that to minimise the mutual coupling effects between the non-active elements and the active element, the switched impedance technique described in [2] proves to be very helpful in all array geometries and especially in the planar geometries. The radiation pattern distortion of the antenna elements in the Y-shaped array can be reduced from about 6dB to about 1dB, whereas with the 3-D tilted cross array this reduces from 4dB to 2dB. The distortion of the phase pattern is with the Y-shaped array reduced from roughly 70 degrees to about 7 degrees and with the 3-D tilted cross array to 25 and 12 degrees.

Chapter 4

High-resolution DOA estimation

4.1 Introduction

In the previous chapter a uniformly spaced 3-D tilted cross array is presented that can be used for azimuth and elevation DOA estimations. In this chapter it is shown that, in cooperation with a suitable high-resolution algorithm, this array is capable of performing accurate and unambiguous DOA estimations.

The chapter starts off with an overview of today's most commonly used methods for DOA estimation. Due to its simplicity and high performance capabilities, one specific method seems to be particularly interesting and suitable for the 3-D tilted cross array, presented in the previous chapter. The algorithm, and the application to the 3-D tilted cross array will be discussed in detail. In addition to this algorithm, a new technique will be presented that significantly improves the performance of the algorithm. Also, a method will be provided that can estimate the power of the incoming waves. Furthermore, simulation results will be presented that show the estimation accuracy and the resolution of the configuration and indicate that accurate high-resolution estimations are possible using the 3-D tilted cross array in combination with a suitable algorithm. Conclusions are drawn in the final section.

4.2 Overview of high-resolution algorithms

High-resolution signal estimation is an interesting technique that is widely used in array signal processing. The technique concentrates on sensor signal processing and uses the spatial information from the sensors positions and the information from the data collected at the sensors in the array to carry out a specific estimation task, e.g. DOA estimation. A variety of estimation algorithms that can be used to estimate the incident signal properties are available in the literature. To discuss all different techniques that are available would be impracticable, therefore, today's most popular high-resolution techniques are discussed.

The most popular estimation methods can roughly be classified into two main categories namely: spectral estimation and non-spectral estimation methods. Subsequently, spectral estimation methods can be subdivided into non-parametric-based and parametric subspace-based techniques, whereas non-spectral estimation methods can be subdivided into parametric subspace-based and Maximum Likelihood-based techniques. Figure 4.1 shows a number of estimation techniques and gives an overview of the different categories.

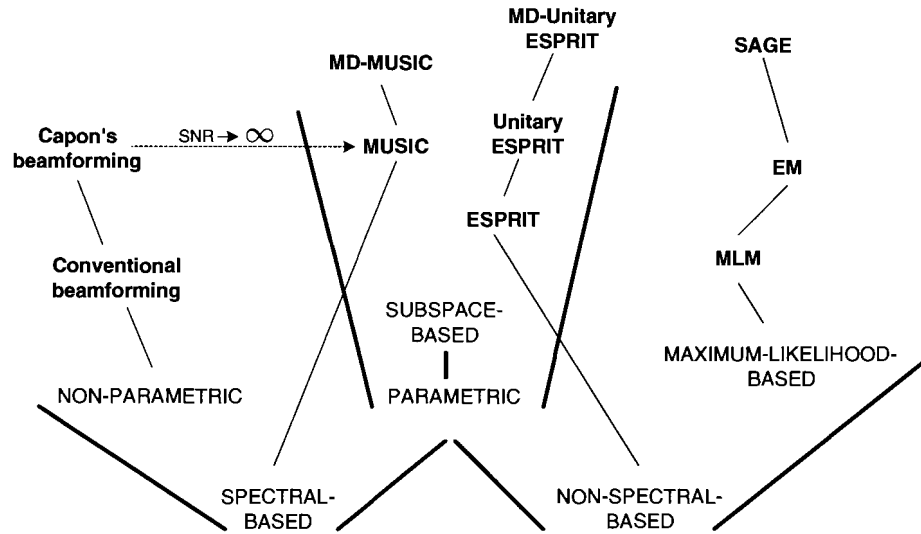


Figure 4.1: Overview of the most popular high-resolution DOA estimation techniques.

Parametric based techniques rely on certain assumptions made on the observed data, such as the number of incident waves. Non-parametric based techniques do not make such assumptions a priori, therefore parametric based techniques generally yield much better resolution capabilities.

Subspace based techniques use the eigendecomposition of the array output covariance matrix to partition the space spanned by its eigenvectors into two subspaces, namely, the signal subspace, and the noise subspace. The signal subspace is spanned by the eigenvectors corresponding to the large eigenvalues and is orthogonal to the noise subspace, which in turn is associated with the smaller eigenvalues of the covariance matrix. This decomposition has led to a number of interesting high-resolution algorithms.

4.2.1 Spectral estimation

In this type of method, a spectrum-like function of the parameters of interest, e.g. DOA, is formed. The locations of the highest, separated peaks in the spectrum function are then identified as the DOA estimates. Within this type of algorithm, one can distinguish non-parametric and parametric subspace-based methods. Non-parametric based DF techniques are often identified as beamforming techniques. These beamforming techniques use the idea to "steer" the mainlobe of the antenna array pattern in the directions of interest and measure the output power. These type of methods can be applied to any type of array configuration, but they generally do not yield high-resolution capabilities. A well know beamforming technique is defined by Capon [21].

Parametric subspace-based methods, such as the Multiple Signal Classification (MUSIC) algorithm [22], offer significant performance improvements compared to beamforming type of spectral estimation methods [21]. That is why the introduction of the MUSIC algorithm in 1986 caused a high interest in the subspace based approach and at that time made MUSIC an alternative to most existing methods. The MUSIC method is a relatively simple and efficient eigenstructure method that also uses a spectrum-like function to determine the

DOAs. It is shown in [23], that the MUSIC method can be interpreted as a Capon-type method, but one that uses a covariance matrix that corresponds to an infinite SNR. This explains the superior resolution of MUSIC compared to that of Capon's beamformer. MUSIC has many variations and is one of the most studied methods in its class. It has the advantage that it can be applied to any array geometry, although it does require intensive computation, because spectrum functions have to be analysed. If the technique is extended into multiple dimensions (MD), multidimensional spectrum functions have to be analysed, which causes a significant increase in the computation intensity.

4.2.2 Non-spectral estimation

In contrast to the previous techniques, non-spectral estimation methods do not use spectrum like functions to determine the DOAs. Instead, they generate distinct values that indicate the estimated DOAs. Two main categories can be distinguished in this type of methods, namely, maximum likelihood (ML) and subspace-based techniques.

The ML method (MLM) has drawn much attention because of its superior performance capabilities, particularly when the SNR or the number of samples is small, or sources are correlated. In ML type of methods, the DOAs are estimated by maximizing the log-likelihood function. The likelihood function is the joint probability density function (PDF) of all observations (the sampled data), given the unknown parameters, in this case the DOAs. Maximising the log-likelihood function is a nonlinear multidimensional optimisation problem and requires iterative schemes for solutions. There are many such schemes available in the literature [24]. A simple and stable iterative method for this job is the Expectation Maximization (EM) algorithm. Unfortunately, the slow convergence makes it less suitable for practical implementations. Recently the Space Alternating Generalized EM (SAGE) algorithm [25], which is an extension of the EM algorithm has drawn more attention. Under certain conditions the SAGE algorithm has a much faster convergence speed than EM. Although these and other techniques can limit the computational complexity of the ML method, the extension of the ML technique into n dimensions still results in a $n \cdot d$ dimensional search, where d denotes the number of incident waves. This causes a much higher computational complexity compared to the multidimensional MUSIC algorithm, where only a n dimensional search is required [26].

When uniform linear arrays (ULA) or uniform rectangular arrays (URA) are used, non-spectral parametric subspace-based estimation methods, also called *subspace fitting* methods can be used that have the same statistical performance as the ML method. The computational cost for these type of methods is much less than for the ML method. A very well known algorithm in this class is the ESPRIT algorithm [27], which stands for Estimation of Signal Parameters via Rotational Invariance Techniques. This computationally efficient and robust algorithm is based on defining two identical sub-arrays that are shifted with a known displacement vector and uses the eigenvalue decomposition of the estimated covariance matrix to solve a number of invariance equations. It is shown that ESPRIT is the most computational efficient algorithm in its class, and is able to achieve near optimal performance for an appropriate choice of subarrays [28].

The Unitary ESPRIT algorithm [29,30], which is a recent extension of the standard ESPRIT algorithm, uses the fact that the operator that represents the phase delays between the two subarrays is unitary. If centro-symmetric array configurations are used, the estimated phase factors can be constrained to the unit circle and the ESPRIT algorithm can be formulated in terms of real-valued computations, which results in a substantial reduction of the

computational complexity. Moreover, Unitary ESPRIT also incorporates forward-backward averaging, which increases the performance, especially for correlated source signals [31]. Recently, it was shown that the Unitary ESPRIT algorithm can be extended into two or more dimensions [32, 33], which makes this algorithm very suitable for DF using a three-dimensional array structure. Also, it is interesting to note that the 3-D DF performance of Unitary ESPRIT is similar to the performance of the SAGE algorithm, as is shown in [34].

After analysing numerous DF techniques, the Unitary ESPRIT algorithm seems to have one of the highest performance capabilities, together with a low computational complexity. Especially in a multidimensional DF system this is a great advantage, because it prevents multidimensional searches. The requirement for centro-symmetry seems to fit perfectly with the 3D tilted cross array structure presented in the previous chapter, which resulted in the decision to use the Unitary ESPRIT algorithm. The next section describes the Unitary ESPRIT algorithm in more detail.

4.3 Unitary ESPRIT

As mentioned before, the Unitary ESPRIT technique is an extension to the standard ESPRIT technique. Before going into detail on the Unitary part of the algorithm and the application to the 3-D array, the standard ESPRIT technique will be explained first.

4.3.1 Standard ESPRIT

The ESPRIT algorithm uses the shift-invariant structure available in the signal subspace and estimates the DOAs through subspace decomposition and eigenvalue calculation. The shift-invariant structure is created by dividing the N elements of the antenna array into two identical overlapping subarrays. Each of the subarrays consists of $N - 1$ elements sensor-sets displaced by a known constant displacement vector Δ , as shown in Figure 4.2. The displacement vector also sets the reference direction, i.e. all angles are measured with reference to this vector. The magnitude of this vector is δ .

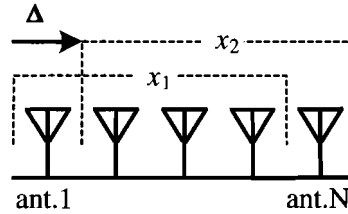


Figure 4.2: Overlapping sub-arrays (x_1 and x_2) displaced by Δ and each consisting of $N - 1$ antenna elements.

When analyzing a single uniformly spaced linear array consisting of two subarrays, the outputs $\mathbf{x}_1(t)$ and $\mathbf{x}_2(t)$ can be written as

$$\mathbf{x}_1(t) = \mathbf{A}_1 \mathbf{s}(t) + \mathbf{n}_1(t) \quad (4.1)$$

$$\mathbf{x}_2(t) = \mathbf{A}_1 \Phi \mathbf{s}(t) + \mathbf{n}_2(t), \quad (4.2)$$

with $\mathbf{s}(t)$ containing the d source signals, $\mathbf{n}_1(t)$ and $\mathbf{n}_2(t)$ containing the noise on each of the subarray elements and \mathbf{A}_1 is a $(N - 1) \times d$ matrix which contains the d so called steering

vectors in its columns that correspond to the d directional sources associated with the first subarray. The steering vectors of the second subarray are given by $\mathbf{A}_1 \Phi$. Where Φ is an $d \times d$ diagonal matrix of the phase differences between the two overlapping sensor sets, with its diagonal elements given by $e^{j\mu_i}$, i.e.

$$\Phi = \begin{bmatrix} e^{j\mu_1} & 0 & \dots & 0 \\ 0 & e^{j\mu_2} & \dots & 0 \\ \vdots & \vdots & \ddots & \vdots \\ 0 & 0 & \dots & e^{j\mu_d} \end{bmatrix}, i = 1, \dots, d. \quad (4.3)$$

In the case of a single ULA the spatial frequency estimates μ_i are given by

$$\mu_i = \frac{\delta 2\pi \sin(\phi_i)}{\lambda}, i = 1, \dots, d. \quad (4.4)$$

From (4.3) and (4.4) it can be seen that if Φ is known, the angles of arrival ϕ_i are known.

Similar as to other subspace-based algorithms, ESPRIT uses the eigendecomposition of the array covariance matrix to find the multidimensional signal subspace. The covariance matrix of \mathbf{x}_1 can be expressed as

$$\mathbf{R}_{x_1} = E\{\mathbf{x}_1 \mathbf{x}_1^H\} = \mathbf{A} \mathbf{R}_s \mathbf{A}^H + \sigma^2 \mathbf{I} \quad (4.5)$$

where \mathbf{R}_s is the covariance matrix of the signal vector \mathbf{s} , σ^2 is the noise power at each antenna element and \mathbf{I} is the $(N - 1) \times (N - 1)$ identity matrix. The superscript "H" denotes conjugate transpose, and $E\{\cdot\}$ denotes statistical expectation.

Using an eigenvalue decomposition (EVD), \mathbf{R}_{x_1} can be written as

$$\mathbf{R}_{x_1} = \mathbf{U} \mathbf{\Lambda} \mathbf{U}^H \quad (4.6)$$

where \mathbf{U} is the matrix formed by the eigenvectors of \mathbf{R}_{x_1} , and $\mathbf{\Lambda}$ is a diagonal matrix containing the respective eigenvalues. The first d highest eigenvalues correspond to the first d eigenvectors that span the d dimensional signal subspace. The noise subspace is spanned by the eigenvalues associated with the smaller eigenvalues and is orthogonal to the signal subspace. Similar expressions can be derived for the covariance matrix of \mathbf{x}_2 .

Now, let \mathbf{U}_1 and \mathbf{U}_2 be two $(N - 1) \times d$ matrices with in their columns d eigenvectors corresponding to the largest eigenvalues of the two covariance matrices \mathbf{R}_{x_1} and \mathbf{R}_{x_2} , respectively. These two sets of eigenvectors span the same d -dimensional signal space and are therefore related by an unique nonsingular ($\det \neq 0$) transformation matrix Ψ in the following, so called invariance equation,

$$\mathbf{U}_{x_2} = \mathbf{U}_{x_1} \Psi. \quad (4.7)$$

In a similar way these matrices are related to the array steering vectors \mathbf{A}_1 and $\mathbf{A}_1 \Phi$ by an unique nonsingular transformation matrix \mathbf{T} as

$$\mathbf{A}_1 = \mathbf{U}_{x_1} \mathbf{T} \quad (4.8)$$

$$\mathbf{A}_1 \Phi = \mathbf{U}_{x_2} \mathbf{T}. \quad (4.9)$$

Substitution of (4.8) and (4.9) into (4.7) leads to

$$\Psi = \mathbf{T} \Phi \mathbf{T}^{-1}. \quad (4.10)$$

This implies that the eigenvalues of Ψ are equal to the diagonal elements of Φ and that the columns of \mathbf{T} are eigenvectors of Ψ . Thus, an eigendecomposition of Ψ determines Φ from which the DOAs can be determined using (4.4).

It should be noted that in practical applications only *estimates* of the true covariance matrix are available, and therefore it is not possible to obtain zero-variance estimates of the DOAs. An estimate of the true covariance matrix can be obtained by averaging over N number of datasets (snapshots). Then an estimate for \mathbf{R} can be determined as

$$\mathbf{R}(n) = \frac{1}{N} \sum_{n=0}^{N-1} \mathbf{x}(n)\mathbf{x}(n)^H. \quad (4.11)$$

If more snapshots are available, \mathbf{R} will approach its true value and its eigenvectors and eigenvalues will become more accurate, which will lead to more accurate estimations.

An other consequence of only having an estimate of \mathbf{R} , is that the eigenvalues become all different with probability one and it is no longer straightforward to distinguish the eigenvalues that belong to either the signal or the noise subspace.

As a result, it is no longer straightforward to estimate the dimension of the noise subspace, and therefore it is only possible to get an *estimate* for the number of sources d . These estimates can be obtained from applying certain criteria such as a method based on AIC (Akaike's information criterion) and Rissanen's MDL principle (minimum description length) [24].

4.3.2 Unitary extension of standard ESPRIT

The standard ESPRIT algorithm operates on complex data, which means all computations in the algorithm are complex. To reduce the computational complexity, Unitary ESPRIT transforms the complex input data matrix \mathbf{X} into a real-valued representation [30]. This means all other computations are real-valued.

Unitary ESPRIT also incorporates Forward-Backward (FB) averaging, which effectively helps to decorrelate possibly correlated source pairs [1, 21]. The FB-averaging requires the array configuration to be centrosymmetric. This centrosymmetry property can be mathematically described as

$$\mathbf{\Pi}_N \mathbf{A} = \mathbf{A}^* \quad (4.12)$$

where,

$$\mathbf{\Pi}_N = \begin{bmatrix} 0 & \cdots & \cdots & & 1 \\ \vdots & \ddots & & & \\ \vdots & & 1 & & \vdots \\ & 1 & & \ddots & \vdots \\ 1 & & \cdots & \cdots & 0 \end{bmatrix} \in \mathbb{R}^{N \times N}, \quad (4.13)$$

and $(.)^*$ denotes the complex conjugate.

Again, consider a single uniformly spaced linear array that satisfies the centrosymmetry property. Before discussing the real-valued transformation, the centrosymmetry property is used to incorporate FB averaging.

The number of snapshots q can be "doubled" by applying FB averaging on the $N \times q$ complex data matrix \mathbf{X} . The *new* set of snapshots are created by mirroring the elements with respect to the centre (rotate columns), flip the order of the snapshots (rotate rows) and

correct for the phase by taking the complex conjugated version of \mathbf{X} , as visualized in figure 4.3.

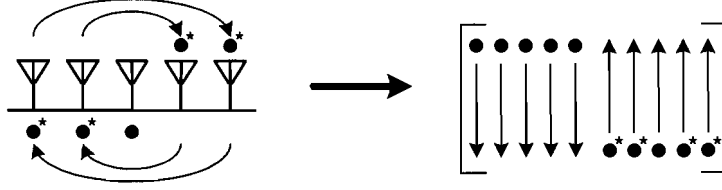


Figure 4.3: A second set of snapshots is created by applying forward backward averaging.

The new $N \times 2q$ measurement matrix results in

$$[\mathbf{X} \quad \mathbf{\Pi}_N \mathbf{X}^* \mathbf{\Pi}_q] \in \mathbb{C}^{N \times 2q}, \quad (4.14)$$

Now, the real-valued transformation can be applied by using the so called centro-Hermitian property. A complex matrix $\mathbf{M} \in \mathbb{C}^{k \times l}$ is called centro-Hermitian if $\mathbf{\Pi}_k \mathbf{M}^* \mathbf{\Pi}_l = \mathbf{M}$. Since (4.14) is centro-Hermitian for every \mathbf{X} , the new measurement matrix is forced to be centro-Hermitian. It is shown in [30] that centro-Hermitian matrices of size $N \times q$ form a $N \cdot q$ -dimensional linear space over \mathbb{R} . This property can be used to map the complex data matrix \mathbf{X} to its real valued equivalent \mathbf{Z} with the help of the so-called left $\mathbf{\Pi}$ -real transformation matrices \mathbf{Q} defined as

$$\mathbf{Q}_{2K} = \frac{1}{\sqrt{2}} \begin{bmatrix} \mathbf{I}_K & j\mathbf{I}_K \\ \mathbf{\Pi}_K & -j\mathbf{\Pi}_K \end{bmatrix} \quad (4.15)$$

if N is even, or

$$\mathbf{Q}_{2K+1} = \frac{1}{\sqrt{2}} \begin{bmatrix} \mathbf{I}_K & 0 & j\mathbf{I}_K \\ 0^T & \sqrt{2} & 0^T \\ \mathbf{\Pi}_K & 0 & -j\mathbf{\Pi}_K \end{bmatrix} \quad (4.16)$$

if N is odd.

The real-valued data matrix \mathbf{Z} can now be written as

$$\mathbf{Z} = \mathbf{Q}_N^H [\mathbf{X} \quad \mathbf{\Pi}_N \mathbf{X}^* \mathbf{\Pi}_q] \mathbf{Q}_{2q} \in \mathbb{R}^{N \times 2q}. \quad (4.17)$$

After applying the real-valued transformation, the signal-subspace \mathbf{E}_s , can be estimated and the invariance equations can be solved, which is similar to estimating \mathbf{U} and solving $\mathbf{\Psi}$ in (4.6) and (4.7) respectively.

The d signal-subspace eigenvectors $\mathbf{E}_s \in \mathbb{R}^{N \times d}$ can be estimated by performing an eigenvalue decomposition (EVD) on

$$\mathbf{Z} \cdot \mathbf{Z}^H \in \mathbb{R}^{N \times N}. \quad (4.18)$$

If we rewrite (4.7) and replace \mathbf{A}_1 and $\mathbf{A}_1 \mathbf{\Phi}$ with $\mathbf{J}_1 \mathbf{A}$ and $\mathbf{J}_2 \mathbf{A}$ respectively, the invariance equation becomes

$$\mathbf{J}_2 \mathbf{A} = \mathbf{J}_1 \mathbf{A} \mathbf{\Phi}, \quad (4.19)$$

where

$$\mathbf{A} = \begin{bmatrix} \mathbf{A}_1 \\ \mathbf{A}_1 \mathbf{\Phi} \end{bmatrix} \quad (4.20)$$

and, \mathbf{J}_1 and \mathbf{J}_2 are selection matrices that select the first and last $N - 1$ components of an $N \times 1$ vector corresponding to the two sub-arrays of the ULA.

It is shown in [33], that the invariance equation (4.19) can be rewritten in terms of real-valued matrices as

$$\mathbf{K}_2 \mathbf{D} = \mathbf{K}_1 \mathbf{D} \mathbf{\Omega} \quad (4.21)$$

where

$$\mathbf{D} = \mathbf{Q}_N^H \mathbf{A} \quad (4.22)$$

$$\mathbf{K}_1 = \mathbf{Q}_{N-1}^H (\mathbf{J}_1 + \mathbf{\Pi}_{N-1} \mathbf{J}_1 \mathbf{\Pi}_N) \mathbf{Q}_N \quad (4.23)$$

$$\mathbf{K}_2 = \mathbf{Q}_{N-1}^H j (\mathbf{J}_1 - \mathbf{\Pi}_{N-1} \mathbf{J}_1 \mathbf{\Pi}_N) \mathbf{Q}_N. \quad (4.24)$$

The diagonal elements of $\mathbf{\Omega}$ in (4.21) now contain real-valued eigenvalues. It can be shown that the eigenvalues ω_i of the complex matrix $\mathbf{\Psi}$ can be determined from the diagonal elements of $\mathbf{\Omega}$ via a linear fractional transformation [33]. This results in

$$\mu_i = 2 \arctan(\omega_i). \quad (4.25)$$

Without additive noise, or with an infinite number of snapshots, \mathbf{E}_s and \mathbf{D} span the same d -dimensional subspace, i.e., there is a nonsingular matrix \mathbf{T} of size $d \times d$ such that $\mathbf{D} = \mathbf{E}_s \mathbf{T}$. However, with additive noise and with a limited number of snapshots, it is only possible to obtain an estimate of \mathbf{E}_s , which means that

$$\mathbf{D} \approx \mathbf{E}_s \mathbf{T}. \quad (4.26)$$

If (4.26) is substituted in (4.21) the real-valued invariance equation can be written as

$$\mathbf{K}_1 \mathbf{E}_s \mathbf{\Upsilon} \approx \mathbf{K}_2 \mathbf{E}_s \quad (4.27)$$

with $\mathbf{\Upsilon} = \mathbf{T} \mathbf{\Omega} \mathbf{T}^{-1}$. If $\mathbf{\Upsilon}$ is solved from (4.27) and its eigenvalues ω_i are determined by performing an EVD, then it is possible to determine μ_i from (4.25) and give an estimate for the DOAs using (4.4).

Several techniques are available to solve $\mathbf{\Upsilon}$ from the invariance equation, such as Least Squares (LS), Total Least squares (TLS) [33, 35], or Structured Least Squares (SLS) techniques [36].

Next, the successive steps of the Unitary ESPRIT algorithm are summarised.

1. Real Valued Transformation and Forward Backward averaging

Transform measurement matrix \mathbf{X}

$$\mathbf{Z} = \mathbf{Q}_N^H \begin{bmatrix} \mathbf{X} & \mathbf{\Pi}_N \mathbf{X}^* \mathbf{\Pi}_q \end{bmatrix} \mathbf{Q}_{2q} \in \mathbb{R}^{N \times 2q}.$$

2. Signal Subspace Estimation

Estimate signal subspace by determining $\mathbf{E}_s \in \mathbb{R}^{N \times d}$ as the eigenvectors of

$$\mathbf{Z} \cdot \mathbf{Z}^H \in \mathbb{R}^{N \times N}.$$

3. Solve invariance equation

Determine Υ from

$$\mathbf{K}_1 \mathbf{E}_s \Upsilon \approx \mathbf{K}_2 \mathbf{E}_s$$

by means of LS, TLS or SLS techniques [33, 35, 36].

4. Compute spatial frequency estimates

Compute ω_i , $1 \leq i \leq d$ as the eigenvalues of Υ and determine μ_i from

$$\mu_i = 2 \arctan(\omega_i).$$

5. Determine DOA estimates

Determine ϕ_i from

$$\phi_i = \arcsin \left(\frac{\lambda \mu_i}{2\pi \delta} \right).$$

4.3.3 Application to 3-D array (3-D Unitary ESPRIT)

As mentioned earlier, the Unitary ESPRIT algorithm requires the antenna array geometry to have uniform element spacing and to be centro-symmetric. This last requirement states that the element positions have to be symmetrical with respect to the origin. The uniformly spaced 3-D tilted cross array that is presented in the previous chapter satisfies these requirements.

To apply Unitary ESPRIT to the 3-D tilted cross array, the algorithm has to be extended to three dimensions. For the sake of simplicity, the algorithm will be derived for a *non-tilted* 3-D cross array. When the algorithm is then applied to the 3-D tilted cross array, the correct DOA estimates can be obtained by rotating the coordinate system 45° around the x-axis and 35.26° around the y-axis. The 3-D *non-tilted* cross array is shown in Figure 4.4.

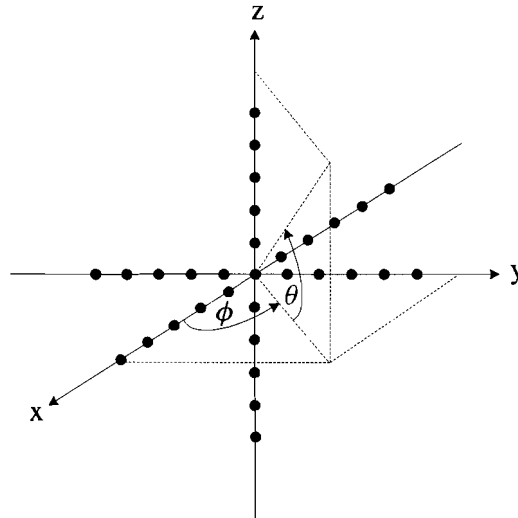


Figure 4.4: 3-D cross array, the black dots represent the antenna elements.

Since the array consists out of three linear arrays, one on each axis, the array steering vector of this array geometry can be divided into three parts, i.e.

$$\mathbf{a} = \begin{bmatrix} \mathbf{a}^{(x)} \\ \mathbf{a}^{(y)} \\ \mathbf{a}^{(z)} \end{bmatrix}. \quad (4.28)$$

When d impinging signals are considered, the array steering vector matrix can be written as

$$\mathbf{A} = [\mathbf{a}_1 \dots \mathbf{a}_d]. \quad (4.29)$$

If it is assumed that all N antenna elements on each arm of the array have isotropic antenna radiation patterns the array response of the three axes can be written as

$$\mathbf{a}_i^{(\zeta)} = \begin{bmatrix} e^{-j\mu_i^{(\zeta)}(N-1)/2} \\ \vdots \\ e^{+j\mu_i^{(\zeta)}(N-1)/2} \end{bmatrix}, \quad \zeta \in \{x, y, z\}. \quad (4.30)$$

The coefficients $\mu_i^{(\zeta)}$ in (4.30) can be determined from the projection of the elements positions $\mathbf{e}_m(r_m, \theta_m, \phi_m)$ onto a vector from the origin that points into the direction of the incident signal $\mathbf{k}_i(1, \theta_i, \phi_i)$ and multiplied with $\beta = \frac{2\pi}{\lambda}$.

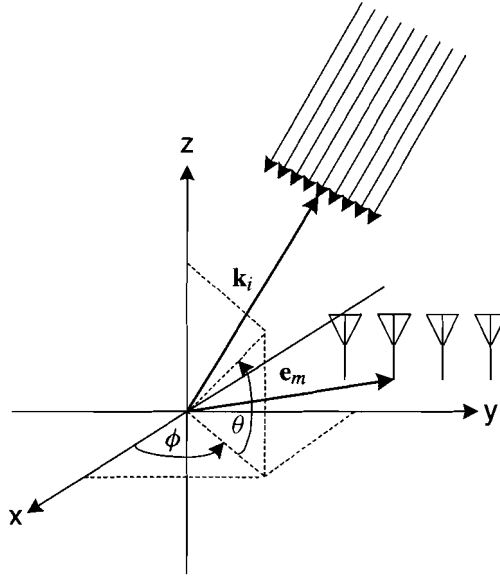


Figure 4.5: Element positions \mathbf{e}_m and a vector \mathbf{k}_i that points into the direction of the incident wave.

With \mathbf{e}_m and \mathbf{k}_i defined as

$$\mathbf{e}_m(r_m, \theta_m, \phi_m) = r_m \cos(\theta_m) \cos(\phi_m) \mathbf{e}_x + r_m \cos(\theta_m) \sin(\phi_m) \mathbf{e}_y + r_m \sin(\theta_m) \mathbf{e}_z \quad (4.31)$$

$$\mathbf{k}_i(1, \theta_i, \phi_i) = \cos(\theta_i) \cos(\phi_i) \mathbf{e}_x + \cos(\theta_i) \sin(\phi_i) \mathbf{e}_y + \sin(\theta_i) \mathbf{e}_z. \quad (4.32)$$

and the element spacing for all elements defined as δ , μ_i can be determined from

$$\mu_i = \frac{2\pi}{\lambda} \delta \{ \cos(\theta_i) \cos(\theta_m) \cos(\phi_i - \phi_m) + \sin(\theta_i) \sin(\theta_m) \}. \quad (4.33)$$

For the 3D cross array geometry described above this results in

$$\mu_i^{(x)} = \frac{2\pi}{\lambda} \delta \cos \phi_i \cos \theta_i \quad (4.34)$$

$$\mu_i^{(y)} = \frac{2\pi}{\lambda} \delta \sin \phi_i \cos \theta_i \quad (4.35)$$

$$\mu_i^{(z)} = \frac{2\pi}{\lambda} \delta \sin \theta_i. \quad (4.36)$$

These last three equations are used in the final part of the 3-D Unitary ESPRIT algorithm to estimate the DOAs from the spatial frequency estimates. In order to do this, the Unitary ESPRIT algorithm has to be extended to three dimensions.

The extension of Unitary ESPRIT to two dimensions is discussed by Zoltowski in [32]. The procedure for the two dimensional case is similar to one dimensional Unitary ESPRIT, except that in the 2D case the spatial frequency estimates $\mu_i^{(x)}$ and $\mu_i^{(y)}$ have to be determined simultaneously. This is necessary to get paired estimation results if the number of waves $d > 1$. If the results would not be paired, it would be impossible to determine which angular elevation estimates correspond to which angular azimuth estimates. In the 2-D case this is achieved by calculating the eigenvalues of the complex matrix $\Upsilon^{(x)} + j\Upsilon^{(y)}$, thereby, automatically pairing the eigenvalues. If, however, the situation changes to three or more dimensions, this pairing of the spatial frequency estimates has to be extended to the higher dimensional case. Simultaneously determining the spatial frequency estimates can be achieved by using a Jacobi-type method.

Before going into detail on the paired spatial frequency estimation, the first three steps of the Unitary ESPRIT algorithm are extended for the three dimensional case as follows.

1. Real Valued Transformation and Forward Backward averaging

The forward-backward averaging and the real valued transformation can be applied on each of the three arms of the array independently by using (4.17). By stacking the three resulting vectors, which is possible because the three arms all have the same phase centre [32], the composite real valued snapshot vector \mathbf{Z}_q can now be defined as

$$\mathbf{Z}_q = \begin{bmatrix} \mathbf{z}_q^{(x)} \\ \mathbf{z}_q^{(y)} \\ \mathbf{z}_q^{(z)} \end{bmatrix} \in \mathbb{R}^{N \times 1} \quad (4.37)$$

with q being the number of snapshots, \mathbf{Z} can be written as

$$\mathbf{Z} = [\mathbf{Z}_1 \ \dots \ \mathbf{Z}_q]. \quad (4.38)$$

2. Signal Subspace Estimation

The signal subspace $\mathbf{E}_s \in \mathbb{R}^{N \times d}$, is estimated by determining the d eigenvectors of

$$\mathbf{Z} \cdot \mathbf{Z}^H \in \mathbb{R}^{N \times N}$$

with d the number of impinging signals on the array. As mention before, it is only possible to get an *estimate* for the number of sources d . These estimates can be obtained by applying certain criteria such as a method based on AIC (Akaike's information criterion) and Rissanen's MDL principle (minimum description length) [24].

3. Solve the Invariance Equations

For the three arms the real-valued representation of the invariance equations can be written as

$$\mathbf{K}_1^{(\zeta)} \mathbf{E}_s \mathbf{\Upsilon}^{(\zeta)} \approx \mathbf{K}_2^{(\zeta)} \mathbf{E}_s \in \mathbb{R}^{N-1 \times d}, \quad \zeta \in \{x, y, z\} \quad (4.39)$$

with the selection matrices $\mathbf{K}_1^{(\zeta)}$ and $\mathbf{K}_2^{(\zeta)}$ defined as

$$\mathbf{K}_1^{(\zeta)} = \mathbf{Q}_{N-1}^H \left(\mathbf{J}_1^{(\zeta)} + \mathbf{\Pi}_{N-1} \mathbf{J}_1^{(\zeta)} \mathbf{\Pi}_N \right) \mathbf{Q}_N \quad (4.40)$$

$$\mathbf{K}_2^{(\zeta)} = \mathbf{Q}_{N-1}^H j \left(\mathbf{J}_1^{(\zeta)} \mathbf{1} - \mathbf{\Pi}_{N-1} \mathbf{J}_1^{(\zeta)} \mathbf{\Pi}_N \right) \mathbf{Q}_N \quad (4.41)$$

where $\mathbf{J}_1^{(\zeta)}$ selects the correct rows for the x, y and z dimension of an arbitrary matrix with vertical dimension N . From (4.39) $\mathbf{\Upsilon}^{(x)}$, $\mathbf{\Upsilon}^{(y)}$ and $\mathbf{\Upsilon}^{(z)}$ can be solved by means of LS, TLS or SLS techniques.

Now that $\mathbf{\Upsilon}^{(\zeta)} \in d \times d$ can be determined for each of the three dimensions, the next step is to create the paired spatial frequency estimates, $\mu_i^{(\zeta)}$, $1 \leq i \leq d$, which are the eigenvalues of $\mathbf{\Upsilon}^{(\zeta)}$, $\zeta \in \{x, y, z\}$.

Taking a closer look at the three $\mathbf{\Upsilon}^{(\zeta)}$'s, determined in the previous step, it becomes clear that in the noiseless case each $\mathbf{\Upsilon}^{(\zeta)}$ has different sets of eigenvalues, corresponding to distinct sets of spatial frequencies $\mu_i^{(\zeta)}$, but they all have the same set of eigenvectors. Therefore, $\mathbf{\Upsilon}^{(\zeta)} = \mathbf{T} \mathbf{\Omega}^{(\zeta)} \mathbf{T}^{-1}$ with the *same* \mathbf{T} for $\zeta \in \{x, y, z\}$. However, the measurement data is affected with noise and only a limited number of measurements is available, which means that the three matrices $\mathbf{\Upsilon}^{(\zeta)}$ do not share the exact same set of eigenvectors. Simply performing an EVD in each of the three cases would generate three different sets of eigenvectors. Determining the eigenvalues using one of these three sets of eigenvectors is obviously not the best solution, since this would discard information contained in the other two matrices.

By using a Jacobi-type method to calculate the Simultaneous Schur Decomposition (SSD) [33], it is possible to simultaneously determine the best approximation for the eigenvalues of $\mathbf{\Upsilon}^{(\zeta)}$, $\zeta \in \{x, y, z\}$ and create paired estimates using information from all three matrices.

The method starts off with the fact that $\mathbf{\Upsilon}^{(\zeta)}$, like any real-valued matrix, can also be written as

$$\mathbf{\Upsilon}^{(\zeta)} = \mathbf{\Theta}^{(\zeta)} \mathbf{U}^{(\zeta)} \mathbf{\Theta}^{(\zeta)T}. \quad (4.42)$$

Here, $\mathbf{\Theta}^{(\zeta)}$ is an orthogonal matrix, i.e. $\mathbf{\Theta}^{(\zeta)} \mathbf{\Theta}^{(\zeta)T} = \mathbf{I}$, and $\mathbf{U}^{(\zeta)}$ is upper triangular with the eigenvalues of $\mathbf{\Upsilon}^{(\zeta)}$ on its diagonal. This decomposition is called the Schur decomposition

[37]. The eigenvalues of $\mathbf{Y}^{(\zeta)}$ are determined as the diagonal elements of

$$\mathbf{U}^{(\zeta)} = \mathbf{\Theta}^{(\zeta)T} \mathbf{Y}^{(\zeta)} \mathbf{\Theta}^{(\zeta)}. \quad (4.43)$$

If $\mathbf{\Theta}^{(\zeta)}$ is the same for $\zeta = x, y, z$, the eigenvalues of the three $\mathbf{Y}^{(\zeta)}$ -matrices and, therefore, also the corresponding spatial frequencies, are automatically paired. This means that, $\mathbf{\Theta}^{(x)}$, $\mathbf{\Theta}^{(y)}$ and $\mathbf{\Theta}^{(z)}$ are forced to be the same. Because of the noise and the limited number of measurements, the three matrices \mathbf{Y}_ζ do not share the exact same set of eigenvectors and there is no orthogonal matrix for which $\mathbf{U}^{(\zeta)}$ is upper triangular for all ζ . Therefore, instead, the algorithm returns the orthogonal matrix $\mathbf{\Theta}$, which minimises the lower-triangular entries of $\mathbf{U}^{(\zeta)}$, $\zeta = x, y, z$. That means that an approximate simultaneous upper-triangularisation is performed that reveals the average eigenstructure. It can be shown that this process is identical to minimising the following cost function

$$\psi(\mathbf{\Theta}) = \sum_{\zeta=x,y,z} \|\mathbf{L}(\mathbf{\Theta}^T \mathbf{Y}^{(\zeta)} \mathbf{\Theta})\|_F^2 \quad (4.44)$$

with $\mathbf{L}(\cdot)$ defined as an operator that extracts the strictly lower triangular part of its matrix-valued argument by setting the upper triangular part and the elements on the main diagonal to zero and $\|\cdot\|_F$ defined as the Frobenius-norm, which calculates the square root of the sum of the absolute squares of its elements.

To calculate a possible orthogonal matrix $\mathbf{\Theta}$, the SSD method uses a Jacobi-type method, which brings the matrix $\mathbf{U}^{(\zeta)}$ more or less quickly to diagonal form [33]. This iterative method performs transformations with plane rotation matrices, each one of which makes a larger than average off-diagonal element (and its transpose) zero. This unfortunately destroys previous zeros, but nevertheless reduces the sum of the off-diagonal elements, so that convergence to a diagonal matrix occurs. Usually, about five iterations are sufficient to reduce the cost function to a minimum and $\mathbf{\Theta}$ is determined. As a result, $\mathbf{U}^{(\zeta)}$ is now automatically determined with $u_{ii}^{(\zeta)}$, $1 \leq i \leq d$, being the diagonal elements of $\mathbf{U}^{(\zeta)}$. The paired spatial frequency estimates can then be estimated as

$$\mu_i^{(\zeta)} = 2 \arctan(u_{ii}^{(\zeta)}). \quad (4.45)$$

From these spatial frequency estimates the DOA estimates can now be determined using

$$\phi_i = \arg(\mu_i^{(x)} + j\mu_i^{(y)}) \quad (4.46)$$

$$\theta_i = \arg\left(j\mu_i^{(z)} + \sqrt{(\mu_i^{(x)})^2 + (\mu_i^{(y)})^2}\right) \quad (4.47)$$

which are derived from (4.34)–(4.36).

4.3.4 Solving invariance equations using an improved SLS technique

From the previous sections it has become clear that the Unitary ESPRIT algorithm is mainly based on calculating a basis of the estimated signal subspace \mathbf{E}_s , after which a set of over-determined equations –the so called invariance equations– are formed by applying the appropriate selection matrices to the basis matrix of the estimated signal subspace. Solving these invariance equations is the core of the Unitary ESPRIT algorithm, from which the DOA estimations are determined. The invariance equations are usually solved via Least Squares

(LS) or Total Least squares (TLS) [33, 35]. These solutions, however, are not optimal since they do not take the relationship between the entries on the left-and right-hand side of the invariance equation into account. A recently developed Structured Least Squares (SLS) technique [36] is a method that does take into account the specific relationship between the entries on the left-and right-hand side of the invariance equations and solves these equations by preserving its structure.

The SLS method offers a significant improvement of the estimation accuracy. In [36] is shown that in critical scenarios, e.g., if the SNR is low, if only a small number of snapshots available, or if highly correlated source signals are present, the SLS method outperforms the LS solution method.

By first analysing the one dimensional case, recall that in (4.27) the invariance equation is defined as

$$\mathbf{K}_1 \mathbf{E}_s \Upsilon \approx \mathbf{K}_2 \mathbf{E}_s \in \mathbb{R}^{N-1 \times d}.$$

In the SLS method it is assumed that, from the fact that the columns of \mathbf{E}_s are corrupted by noise, the estimate of the unknown signal subspace \mathbf{E}_s is subject to error. It is therefore possible to allow a small change, $\Delta \mathbf{E}_s$, of the basis of the estimated signal subspace.

The new signal subspace can now be written as

$$\mathbf{E}_s(k+1) = \mathbf{E}_s(k) + \Delta \mathbf{E}_s(k), \quad (4.48)$$

where k denotes the number of iteration steps needed to determine the new \mathbf{E}_s . This new signal subspace $\mathbf{E}_s(k+1)$ can be an improved signal subspace, if it is determined such that the Frobenius-norm of the resulting residual matrix

$$\mathbf{R}(\mathbf{E}_s, \Upsilon) = \mathbf{K}_1 \mathbf{E}_s \Upsilon - \mathbf{K}_2 \mathbf{E}_s \quad (4.49)$$

derived from (4.27), is minimised. At the same time, the Frobenius-norm of the matrix $\Delta \mathbf{E}_s$, that represents the signal subspace change, should be kept as small as possible.

The SLS technique can now be explained as a technique that determines the matrices $\Delta \mathbf{E}_s$ and $\Delta \Upsilon$ such that they minimise the following expression

$$\left\| \begin{bmatrix} \mathbf{R}(\mathbf{E}_s, \Upsilon) \\ \kappa \cdot \Delta \mathbf{E}_s \end{bmatrix} \right\|_F \quad (4.50)$$

with the weighting factor κ defined as $\kappa = \sqrt{(M-1)/(\alpha M)}$, $\alpha > 1$, such that the minimization is independent of the two matrix sizes in (4.50).

As described in [36], it is possible to derive an iterative algorithm to solve (4.50) by linearising $\mathbf{R}(\mathbf{E}_s, \Upsilon)$. With $\mathbf{E}_s(k)$ and $\Delta \mathbf{E}_s(k)$ at the $k^{(th)}$ iteration step defined in (4.48) and $\Upsilon(k)$ and $\Delta \Upsilon(k)$ defined as

$$\Upsilon(k+1) = \Upsilon(k) + \Delta \Upsilon(k), \quad (4.51)$$

the linearised minimization of (4.50) reduces to the solution of

$$\begin{bmatrix} \text{vec}\{\Delta \Upsilon(k)\} \\ \text{vec}\{\Delta \mathbf{E}_s(k)\} \end{bmatrix} = -\mathbf{Z}^{-1} \cdot \begin{bmatrix} \text{vec}\{\mathbf{R}(k)\} \\ \kappa \cdot \text{vec}\{\mathbf{E}_s(k) - \mathbf{E}_s(0)\} \end{bmatrix} \quad (4.52)$$

with the block-upper triangular matrix \mathbf{Z} defined as

$$\mathbf{Z} = \begin{bmatrix} \mathbf{I} \otimes \mathbf{K}_1 \mathbf{E}_s(k) & [\Upsilon^T(k) \otimes \mathbf{K}_1] - [\mathbf{I} \otimes \mathbf{K}_2] \\ \mathbf{0} & \kappa \cdot \mathbf{I} \end{bmatrix}, \quad (4.53)$$

where \otimes denotes the Kronecker matrix product. The initial solution $\mathbf{E}_s(0)$ can simply be determined using LS or TLS techniques.

The one-dimensional SLS technique described above, can only separately solve the three invariance equations defined in (4.39). To solve the three invariance equations simultaneously the 1-D SLS method has to be extended to three dimensions. This results in the 3-D SLS which is derived in similar fashion as the 2-D extension of SLS described in [36].

The 3-D SLS technique then determines the matrices $\Delta \mathbf{E}_s$, $\Delta \mathbf{\Upsilon}^{(x)}$, $\Delta \mathbf{\Upsilon}^{(y)}$ and $\Delta \mathbf{\Upsilon}^{(z)}$ such that they minimise the following expression

$$\left\| \begin{bmatrix} \mathbf{R}^{(\zeta)}(\mathbf{E}_s, \mathbf{\Upsilon}^{(\zeta)}) \\ \kappa \cdot \Delta \mathbf{E}_s \end{bmatrix} \right\|_F, \quad \zeta \in \{x, y, z\} \quad (4.54)$$

Similar as to (4.50), it is possible to derive an iterative algorithm to solve (4.54). The problem then reduces to the solution of

$$\begin{bmatrix} \text{vec}\{\Delta \mathbf{\Upsilon}^{(\zeta)}(k)\} \\ \text{vec}\{\Delta \mathbf{E}_s(k)\} \end{bmatrix} = -\mathbf{Z}^{-1} \cdot \begin{bmatrix} \text{vec}\{\mathbf{R}^{(\zeta)}(k)\} \\ \kappa \cdot \text{vec}\{\mathbf{E}_s(k) - \mathbf{E}_s(0)\} \end{bmatrix}, \quad \zeta \in \{x, y, z\}, \quad (4.55)$$

with the block-upper triangular matrix \mathbf{Z} derived in similar fashion as for the 2-D case described in [36].

Besides giving better estimation results for \mathbf{E}_s and $\mathbf{\Upsilon}^{(\zeta)}$, this 3-D SLS can be extended to incorporate a solution to a specific rank deficiency problem, which can be explained as follows.

Recall that in order to determine the signal properties of all d incident waves, \mathbf{E}_s should span the entire d dimensional signal subspace, in other words \mathbf{E}_s must have rank d . This condition also ensures that the set of invariance equations, as defined in (4.39), have a unique solution and all $\mathbf{\Upsilon}$'s can be uniquely determined and share the same set of eigenvectors. This, in turn ensures that the spatial frequency estimates, from which the DOA can be determined, are unique.

One necessary condition that prevents \mathbf{E}_s to become rank deficient and generally limits the number of resolvable paths is that $d \leq N - 1$ [23], where N denotes the number of antenna elements. With the array configuration defined here, however, in some situations it is still possible that \mathbf{E}_s becomes rank deficient, even though the previous condition is met. This situation can occur whenever two or more arriving waves have the same projection on one of the axis in the array. In that case, \mathbf{E}_s becomes rank deficient, which is caused by the fact that $\mu_i^{(\zeta)}$, defined in (4.34)–(4.36), becomes the same for two or more i 's.

For example, it can immediately be seen from equations (4.34)–(4.36) that one of the situations where rank deficiency will occur is the situation where two or more waves arrive at the same elevation angle, i.e. they share the same θ and $\mu_i^{(z)}$. If this happens, one of the invariance equations will have infinitely many solutions and $\mathbf{\Upsilon}^{(z)}$ will not be uniquely determined. As a result, the elevation angle estimates will have a significant error.

Although \mathbf{E}_s may become rank deficient in some situations, it is mentioned before that there can only be one set of solutions where the matrices $\mathbf{\Upsilon}^{(x)}$, $\mathbf{\Upsilon}^{(y)}$, $\mathbf{\Upsilon}^{(z)}$ share the same set of eigenvectors. This fact, can be used to solve the rank deficiency problem.

A necessary and sufficient condition for two matrices \mathbf{V} and \mathbf{W} to share the same set of eigenvectors is that $\mathbf{VW} = \mathbf{WV}$ [38]. In the case of the 3-D cross array this leads to the

following set of equations

$$\mathbf{F}_{x,y} = \mathbf{\Upsilon}^{(x)} \mathbf{\Upsilon}^{(y)} - \mathbf{\Upsilon}^{(y)} \mathbf{\Upsilon}^{(x)} = 0 \quad (4.56)$$

$$\mathbf{F}_{y,z} = \mathbf{\Upsilon}^{(y)} \mathbf{\Upsilon}^{(z)} - \mathbf{\Upsilon}^{(z)} \mathbf{\Upsilon}^{(y)} = 0 \quad (4.57)$$

$$\mathbf{F}_{z,x} = \mathbf{\Upsilon}^{(z)} \mathbf{\Upsilon}^{(x)} - \mathbf{\Upsilon}^{(x)} \mathbf{\Upsilon}^{(z)} = 0. \quad (4.58)$$

These equations impose extra conditions that can be used in solving the invariance equations.

In [38], a technique is shown that can solve the rank deficiency problem by using equations (4.56)–(4.58) and by writing the solutions of the invariance equations as a sum of a particular and homogenous solution. Subsequently the problem is solved using a Newton-Raphson iteration scheme. Although this method works fine in theory, it is highly unpractical, since it requires the particular and homogenous solutions of the invariance equation to be determined accurately.

To find a better solution to the rank deficiency problem, the conditions in equations (4.56)–(4.58) are used in the 3-D SLS technique, which have resulted in a new extended SLS method.

The new extended 3-D SLS technique determines the matrices $\Delta \mathbf{E}_s$, $\Delta \mathbf{\Upsilon}^{(x)}$, $\Delta \mathbf{\Upsilon}^{(y)}$ and $\Delta \mathbf{\Upsilon}^{(z)}$ such that they minimise the following expression

$$\left\| \begin{bmatrix} \mathbf{R}^{(\zeta)}(\mathbf{E}_s, \mathbf{\Upsilon}^{(z)}) \\ \mathbf{F}_{x,y}(\mathbf{\Upsilon}^{(x)}, \mathbf{\Upsilon}^{(y)}) \\ \mathbf{F}_{y,z}(\mathbf{\Upsilon}^{(y)}, \mathbf{\Upsilon}^{(z)}) \\ \mathbf{F}_{z,x}(\mathbf{\Upsilon}^{(z)}, \mathbf{\Upsilon}^{(x)}) \\ \kappa \cdot \Delta \mathbf{E}_s \end{bmatrix} \right\|_F, \quad \zeta \in \{x, y, z\}. \quad (4.59)$$

The iterative solution to this problem can be written as

$$\begin{bmatrix} \text{vec}\{\Delta \mathbf{\Upsilon}^{(\zeta)}(k)\} \\ \text{vec}\{\Delta \mathbf{E}_s(k)\} \end{bmatrix} = -\mathbf{Z}^{-1} \cdot \begin{bmatrix} \text{vec}\{\mathbf{R}^{(\zeta)}(k)\} \\ \text{vec}\{\mathbf{F}_{(x,y)}(k)\} \\ \text{vec}\{\mathbf{F}_{(y,z)}(k)\} \\ \text{vec}\{\mathbf{F}_{(z,x)}(k)\} \\ \kappa \cdot \text{vec}\{\mathbf{E}_s(k) - \mathbf{E}_s(0)\} \end{bmatrix}, \quad (4.60)$$

where,

$$\mathbf{R}^{(\zeta)}(k+1) = \mathbf{R}^{(\zeta)}(k) + \mathbf{K}_1^{(\zeta)}[\mathbf{E}_s(k) \Delta \mathbf{\Upsilon}^{(\zeta)}(k) + \Delta \mathbf{E}_s(k) \mathbf{\Upsilon}^{(\zeta)}(k)] - \mathbf{K}_2^{(\zeta)} \Delta \mathbf{E}_s(k) \quad (4.61)$$

$$\begin{aligned} \mathbf{F}_{x,y}(k+1) &= \mathbf{F}_{x,y}(k) + \mathbf{\Upsilon}_x(k) \Delta \mathbf{\Upsilon}_y(k) + \Delta \mathbf{\Upsilon}_x(k) \mathbf{\Upsilon}_y(k) \\ &\quad - \mathbf{\Upsilon}_y(k) \Delta \mathbf{\Upsilon}_x(k) - \Delta \mathbf{\Upsilon}_y(k) \mathbf{\Upsilon}_x(k) \end{aligned} \quad (4.62)$$

and $\mathbf{F}_{y,z}(k+1)$ and $\mathbf{F}_{z,x}(k+1)$ can be derived in similar fashion.

The matrix \mathbf{Z} can be defined as

$$\mathbf{Z} = \begin{bmatrix} \mathbf{I} \otimes (\mathbf{K}_1^{(x)} \mathbf{E}_s(k)) & \mathbf{0} \\ \mathbf{0} & \mathbf{I} \otimes (\mathbf{K}_1^{(y)} \mathbf{E}_s(k)) \\ \mathbf{0} & \mathbf{0} \\ \mathbf{\Upsilon}^{(y)T}(k) \otimes \mathbf{I} - \mathbf{I} \otimes \mathbf{\Upsilon}^{(y)}(k) & \mathbf{I} \otimes \mathbf{\Upsilon}^{(x)}(k) - \mathbf{\Upsilon}^{(x)T}(k) \otimes \mathbf{I} \\ \mathbf{0} & \mathbf{\Upsilon}^{(z)T}(k) \otimes \mathbf{I} - \mathbf{I} \otimes \mathbf{\Upsilon}^{(z)}(k) \\ \mathbf{I} \otimes \mathbf{\Upsilon}^{(z)}(k) - \mathbf{\Upsilon}^{(z)T}(k) \otimes \mathbf{I} & \mathbf{0} \\ \mathbf{0} & \mathbf{0} \end{bmatrix}$$

$$\begin{bmatrix}
\mathbf{0} & \mathbf{\Upsilon}^{(x)T}(k) \otimes \mathbf{K}_1^{(x)} - \mathbf{I} \otimes \mathbf{K}_2^{(x)} \\
\mathbf{0} & \mathbf{\Upsilon}^{(y)T}(k) \otimes \mathbf{K}_1^{(y)} - \mathbf{I} \otimes \mathbf{K}_2^{(y)} \\
\mathbf{I} \otimes (\mathbf{K}_1^{(z)} \mathbf{E}_s(k)) & \mathbf{\Upsilon}^{(z)T}(k) \otimes \mathbf{K}_1^{(z)} - \mathbf{I} \otimes \mathbf{K}_2^{(z)} \\
\mathbf{0} & \mathbf{0} \\
\mathbf{I} \otimes \mathbf{\Upsilon}^{(y)}(k) - \mathbf{\Upsilon}^{(y)T}(k) \otimes \mathbf{I} & \mathbf{0} \\
\mathbf{\Upsilon}^{(x)T}(k) \otimes \mathbf{I} - \mathbf{I} \otimes \mathbf{\Upsilon}^{(x)}(k) & \mathbf{0} \\
\mathbf{0} & \kappa \cdot \mathbf{I}
\end{bmatrix} \quad (4.63)$$

By incorporating this new and extended 3D SLS technique in the 3D Unitary ESPRIT algorithm, the invariance equations can be solved more accurately, which in turn leads to more accurate estimation results. Also, a solution to the rank deficiency problem prevents situations in which the invariance equations have infinite many solutions, which can lead to false estimates.

4.3.5 Power estimation

Besides giving accurate DOA estimates, the Unitary ESPRIT algorithm also offers an efficient way to reconstruct the original signal matrix \mathbf{S} , based on reliable DOA estimates. From this signal matrix the individual powers of the sources can be determined.

Rewriting (4.1-4.2) and (4.8-4.9) leads to following equations

$$\mathbf{X} = \begin{bmatrix} \mathbf{X}_1 \\ \mathbf{X}_2 \end{bmatrix} = \begin{bmatrix} \mathbf{A}_1 \\ \mathbf{A}_1 \mathbf{\Phi} \end{bmatrix} \mathbf{S} + \begin{bmatrix} \mathbf{N}_1 \\ \mathbf{N}_2 \end{bmatrix} = \mathbf{A} \mathbf{S} + \mathbf{N} \quad (4.64)$$

$$\mathbf{A} = \begin{bmatrix} \mathbf{U}_1 \mathbf{T} \\ \mathbf{\Phi} \mathbf{U}_2 \mathbf{T} \end{bmatrix} = \mathbf{U}_s \mathbf{T}, \quad (4.65)$$

with \mathbf{S} being the signal source matrix that has to be estimated in order to determine the powers of the estimated DOAs. In [29], it is shown that by using a singular-value-decomposition (SVD), \mathbf{S} can be written as

$$\mathbf{S} = \mathbf{T}^{-1} \mathbf{U}_s^H \mathbf{X}. \quad (4.66)$$

Using (4.65) and the fact that $\mathbf{U}_s = \mathbf{Q}_N \mathbf{E}_s$ [36], (4.66) can be written as

$$\mathbf{S} = \mathbf{A}^{-1} \mathbf{Q}_N \mathbf{E}_s \mathbf{E}_s^H \mathbf{Q}_N^H \mathbf{X}. \quad (4.67)$$

This means that if reliable DOAs are determined from the measurement data in \mathbf{X} , which implies that \mathbf{A} and \mathbf{E}_s can be reliably determined as well, the signal source matrix \mathbf{S} can be determined.

From \mathbf{S} , an estimate of the powers of the incident waves can now be determined as the diagonal elements of

$$\frac{1}{q} [\mathbf{S} \cdot \mathbf{S}^H,] \quad (4.68)$$

where q denotes the number of snapshots.

4.4 Simulation results

To verify the theory of the 3-D Unitary ESPRIT algorithm applied to the 3-D tilted cross array, the algorithm presented in the previous section is implemented in Matlab-code and

subsequently computer simulations are performed. After explaining the assumptions on which the simulations are based, results are presented that show that the algorithm is capable of resolving the angles-of arrival and corresponding powers of several incident waves. Next, simulation results are presented that show the improvement of the extended SLS method that is used to solve the invariance equations in comparison to the standard SLS, LS and TLS methods.

Furthermore, to analyse the performance of the 3-D antenna array in combination with Unitary ESPRIT, the estimation accuracy, expressed as the Root-Mean-Square (RMS) error in degrees of the angular estimation versus the Signal-to-Noise Ratio (SNR) in dB will be used. Also, the estimation accuracy versus the source separation in degrees will be used assuming a two-path environment. Additionally, the resolution in degrees, generally defined as the ability to resolve two closely spaced sources, versus the SNR in dB is used as an important performance measure. Moreover, it will be shown that the number of snapshots that are taken, also determine the performance capabilities of the system.

4.4.1 Assumptions

Throughout the simulations the following assumptions are made:

Plane wave assumption It is assumed that the electromagnetic field around the array can be modelled as the superposition of plane waves. This means the array is situated in the far-field region of the source, which is true if the array size is small compared to the distance of the array to the nearest scattering centre. This distance generally has to be larger than $2D^2/\lambda$, with D being the largest dimension of the antenna array aperture. Beyond this distance is the far-field region where the angular distribution of the energy does not vary with the distance r , and the power level decays according to $1/r^2$. With D being 108λ , this results in a minimum distance of 5.27 meters.

Narrowband assumption To ensure that each multipath wave is received identically at all array elements except for a the phase factor, the maximum array aperture is assumed to be small compared to the distance covered at the speed of light during one bit period, which is 6 meters in the current system [1].

Static sampling assumption The distance travelled by the array during one complete snapshot (sampling of all 31 elements in the array) is assumed to be much less than a wavelength to prevent phase errors between the sequentially sampled elements. This distance is determined to be less than $1/100^{th}$ of a wavelength, as will be shown in section 5.4.

Multipath consistency The multipath properties of the radio channel under test are assumed to be consistent during one complete set of snapshots, from which the DOAs are determined. This distance depends largely on the properties of the multipath environment under test and is assumed to be in the order of 0.5 to 2 meters [39].

Common noise variance It is assumed that the noise has a common variance σ^2 at all sensors and is uncorrelated among all sensors (spatially white noise).

4.4.2 Signal estimation

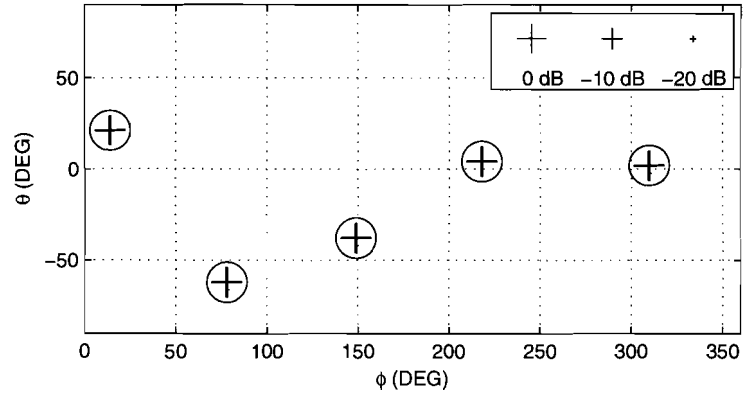
To test if the algorithm is actual capable of resolving the angles-of arrival and corresponding powers of several incident waves, simulation are performed with five sources. Table 4.1 shows the arbitrary position of the sources in azimuth and elevation. The relative power of the individual sources is equal to 0dB in all cases.

Table 4.1: Azimuth and elevation angles of incident waves.

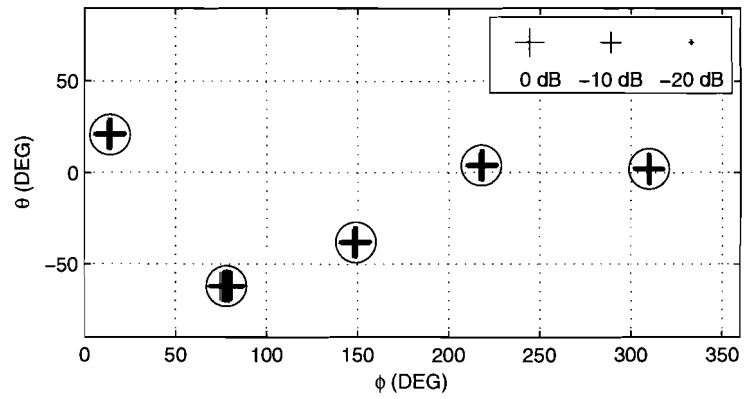
Source no.	1	2	3	4	5
θ (degrees)	21	-62	-38	4	2
ϕ (degrees)	14	78	149	218	310

Figure 4.6 shows the results of signal estimations using 3D Unitary ESPRIT incorporated with the extended SLS method. A total of 100 simulation runs are performed with an SNR of 35, 25 and 15dB and the number of snapshots, q , is made equal to 10. It should be noted that it is assumed that the number of incident sources, in this case five, is know a priori. For the algorithm, this means that it will always present five estimation results. The values for the SNR levels are chosen because they represent the expected maximum (35dB), typical (25dB) and minimum (15dB) values determined from previous measurements [1].

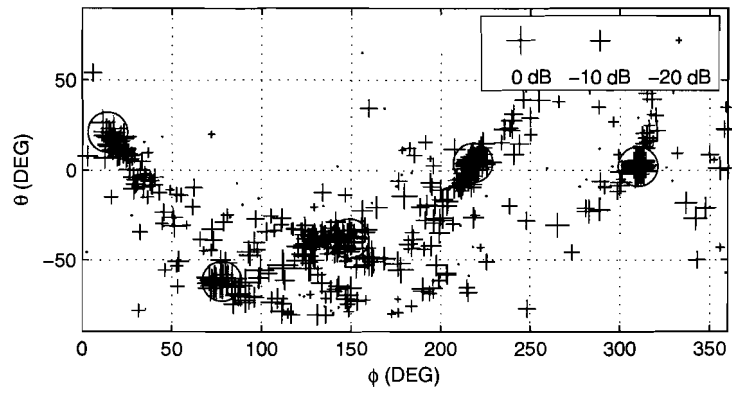
The results show that the algorithm is capable of resolving the true DOAs and corresponding powers of a number of incident waves at 35dB and 25dB SNR. When the SNR becomes 15dB, a number of spurious estimates occurs, which means the sources are not resolved in al of the cases.



(a) SNR=35dB



(b) SNR=25dB



(c) SNR=15dB

Figure 4.6: DOA estimation using five incident waves and 10 snapshots with SNR levels of 35, 25 and 15dB.

Although sometimes not all sources are resolved, the estimated power gives an indication of the reliability of a DOA estimation. This is because large estimation errors generally tend to have a low estimation power, which is confirmed by figure 4.7. This figure shows the estimated signal power, P , versus the maximum RMS-error in the angular estimation. The maximum RMS-error is the maximum of the combined azimuth and elevation RMS-error from either of the two estimated sources, and can thus be defined as

$$\epsilon_{max} = \max \left(\sqrt{(\epsilon_{\theta})^2 + (\epsilon_{\phi})^2} \right). \quad (4.69)$$

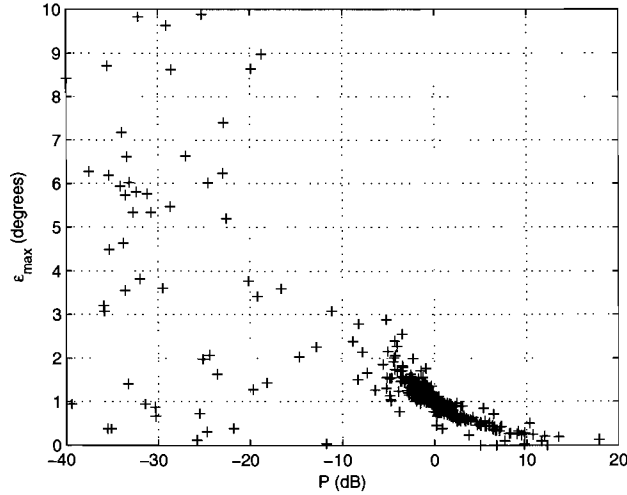
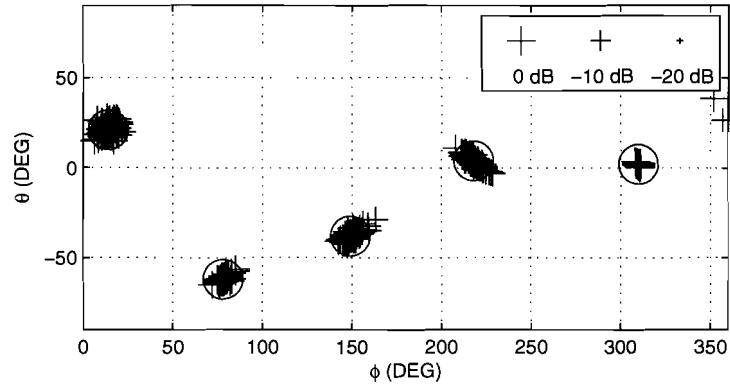


Figure 4.7: Maximum RMS-error versus the estimated power at $(\phi = 0, \theta = 0)$.

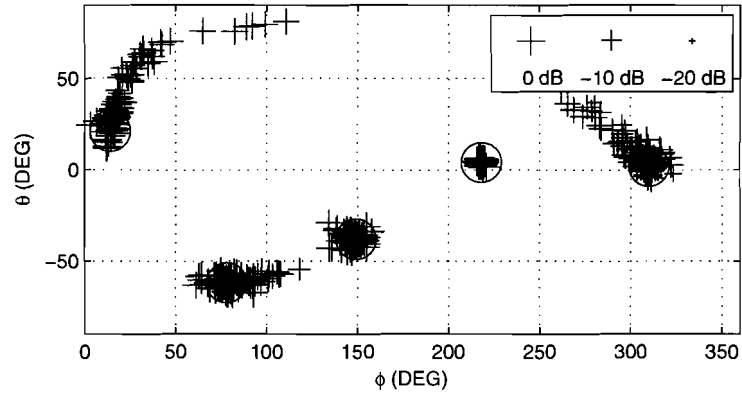
The next simulations presented here are performed to show the difference between the extended SLS method and the standard SLS and the LS and TLS methods.

Figure 4.8 shows the estimation results for a typical SNR of 25dB and 10 number of snapshots, using the standard SLS method and the LS and TLS method. Again, the results of 100 separate simulation runs are presented. Also, in these simulations it is assumed that the number of incident sources is known a priori. The source estimations are indicated with crosses from which the size corresponds with the amount of estimated power. The actual DOA are indicated with circles.

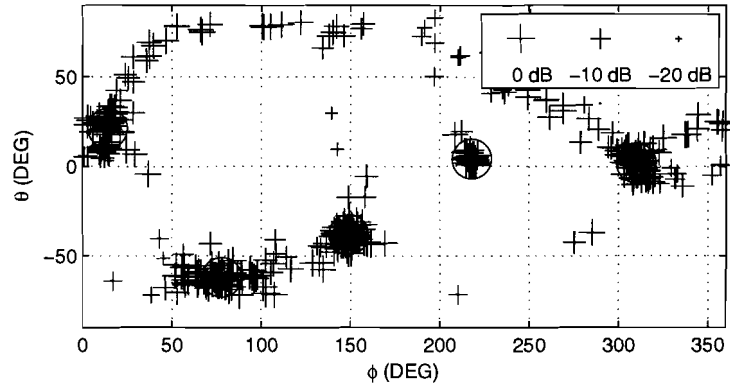
If the results are compared with the extended SLS method presented in the previous simulations, it can be seen that there is a significant performance improvement using the new extended SLS method to solve the invariance equations. While the extended SLS method resolves all signals at SNR=25dB, the standard SLS, LS and TLS methods produce a number of spurious estimates. It is also shown that the LS technique outperforms the TLS technique, which is a somewhat surprising result since TLS is computationally more expensive than LS.



(a) standard SLS



(b) LS



(c) TLS

Figure 4.8: DOA estimation for five incident waves with SNR=25dB and 10 number of snapshots using (a) the standard SLS method, (b) the LS method and (c) the TLS method.

4.4.3 Estimation accuracy

The estimation accuracy of a direction-finding system can be described as the angular difference in elevation and azimuth between the *estimated* and the *initial* direction of a source. This estimation error ϵ can be determined from the combined azimuth and elevation RMS error averaged over K number of simulation runs and can be written as

$$\epsilon = \frac{1}{K} \sum_{i=1}^K \sqrt{(\epsilon_{\theta}^i)^2 + (\epsilon_{\phi}^i)^2}. \quad (4.70)$$

To give an indication of the accuracy at different SNR levels and different number of snapshots, simulations are performed with a single source at $(\theta = 0, \phi = 0)$. The results are visualized in figure 4.9, where $K = 100$.

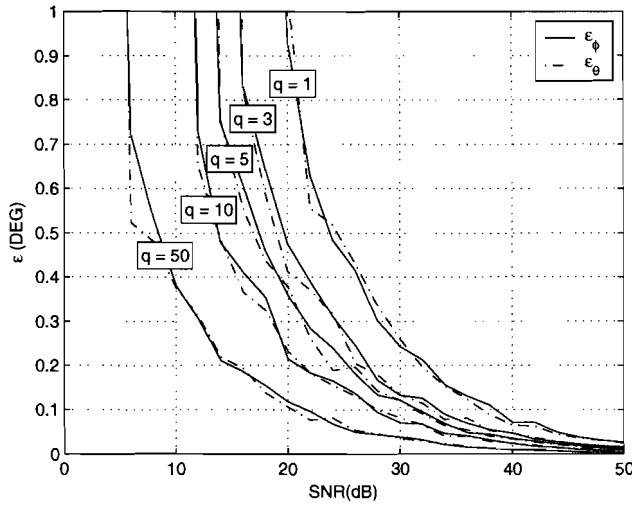


Figure 4.9: RMS-error versus SNR in azimuth and elevation at $(\phi = 0, \theta = 0)$ for different number of snapshots.

The results show that especially at low SNR levels the number of snapshots play a great role in the accuracy of the estimations.

Another point of interest is the degradation of the accuracy when two sources are brought closer to each other. Figure 4.10 shows the estimation error for different separation distances of the two sources with an SNR of 25dB and with different number of snapshots. From figure 4.10 it can be seen that there is a critical point at which the estimation error rises dramatically. This sudden increase in error is caused by the fact that at this point several large errors occur over a number of runs. These large errors overrule the smaller errors and create this rapid increase. This figure can also give a rough indication of the resolution of the system, as will become more clear in the next section. In the case of $q=10$, the resolution is expected to be close to 5 degrees.

To investigate how uniformly distributed the estimation accuracy is over the entire azimuth and elevation range, DOA estimations are simulated with a single source that is swept over the entire azimuth and the positive elevation range at different SNR levels. The estimations are computed from 10 snapshots and statistically averaged over 100 runs. Figure 4.11 and 4.12 show the RMS-error in azimuth and elevation with an SNR of 25dB and 15dB respectively. Only positive elevation angles are used here, because the negative will

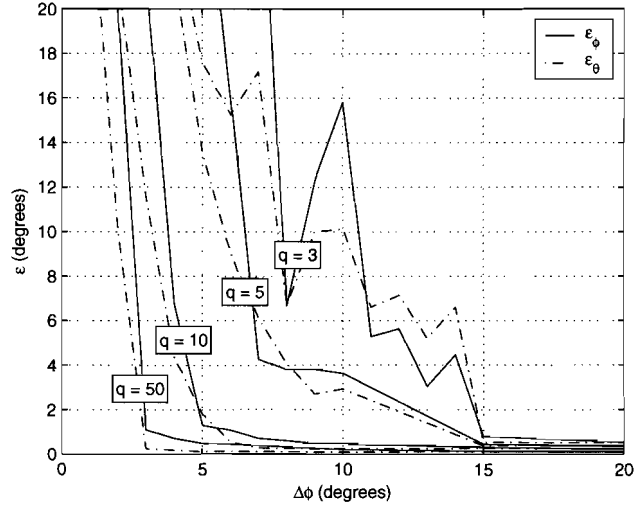


Figure 4.10: RMS-error versus the separation distance at ($\phi = 0, \theta = 0$) for different numbers of snapshots.

produce the same result. In figure 4.11 (b) it is shown that the estimation error lies between 0.1 and 0.2 degrees and is uniformly distributed over the entire range. In figure 4.11 (a) the estimation error in the lower elevation range also lies between 0.1 and 0.2 degrees but increases towards higher elevation angles. This increase is caused by the definition of the azimuth elevation system. The azimuth angle effectively becomes smaller if the elevation angle increases. This causes the difference in errors for higher elevation errors between azimuth and elevation.

In figure 4.12 large errors are visible in three distinctive areas around ($\theta = 35, \phi = 0$), ($\theta = 35, \phi = 120$) and ($\theta = 35, \phi = 240$). These large errors can be explained by the fact that at these locations grating lobes would occur if the spacing between the elements would not be sufficiently large. The presence of more noise in the received signal causes the grating lobes to "re-appear" as larger errors in the spectrum.

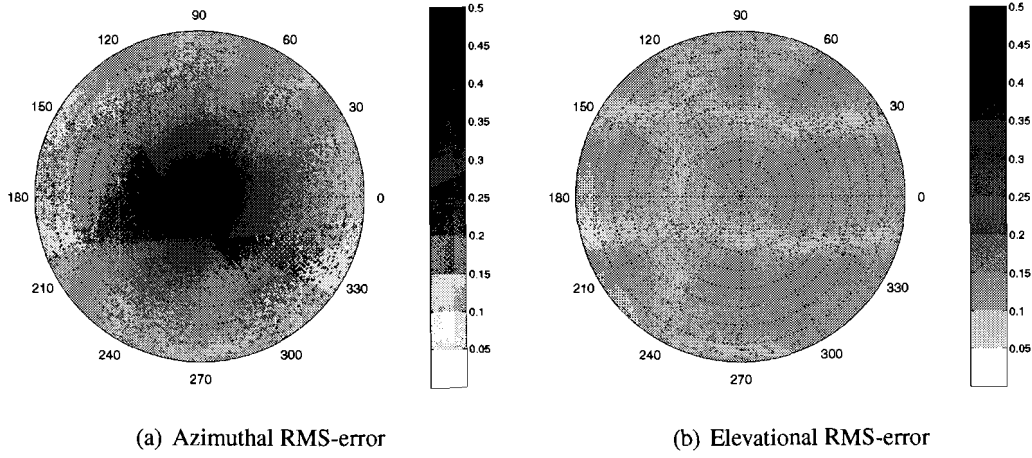


Figure 4.11: Estimation error in degrees for 1 source with 10 snapshots and SNR=25dB. Dotted lines are drawn every thirty degrees azimuth and dotted circles are drawn every ten degrees elevation (outer perimeter corresponds with $\theta = 0^\circ$; centre dot corresponds with $\theta = \pm 90^\circ$).

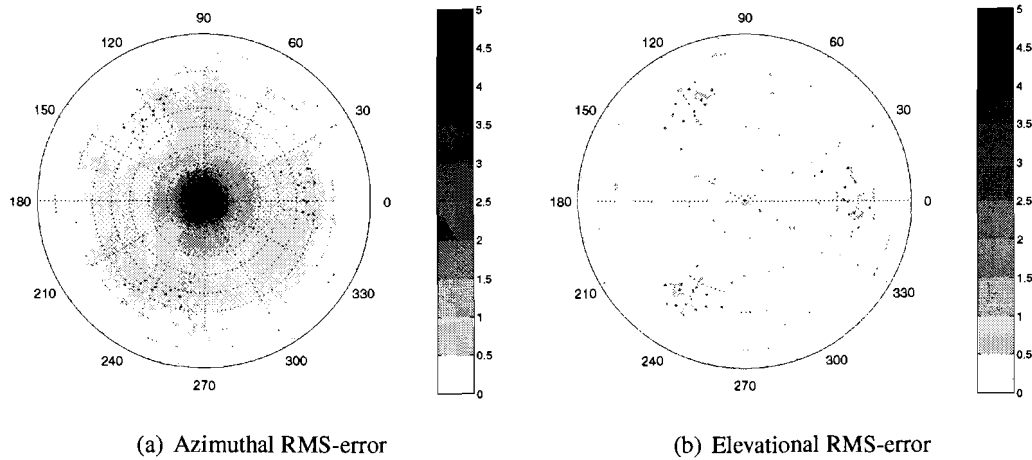


Figure 4.12: Estimation error in degrees for 1 source with 10 snapshots and SNR=15dB. Dotted lines are drawn every thirty degrees azimuth and dotted circles are drawn every ten degrees elevation (outer perimeter corresponds with $\theta = 0^\circ$; centre dot corresponds with $\theta = \pm 90^\circ$).

4.4.4 Resolution

The resolution of a direction finding system is generally defined as the ability to resolve two closely spaced sources with equal power. This resolution can be determined in the azimuth as well as the elevation range. For spectrum based estimation algorithms, this resolution can simply be determined from the spectrum. In [1], it was shown that the resolution threshold lies at the point where the peaks in the spectrum at the true DOAs are greater than the level in the spectrum that lies exactly between those two true DOAs with more than 50% probability. For non-spectrum based estimation algorithms the resolution-threshold can be hard to determine. If the unitary ESPRIT algorithm assumes two sources are present, it will always come up with two estimates, whatever the scenario is. But if two waves are positioned extremely close, the algorithm will usually give one estimate that lies between the two initial positions, and one estimate at some arbitrary position. This effect can help to create a definition for the resolution.

Here, the resolution is defined as the minimum angular separation, $\Delta\phi$, of two sources with equal power, which is still larger than two times the maximum RMS-estimation error, ϵ_{max} , with more than 50% probability. This definition is visualised in figure 4.13.

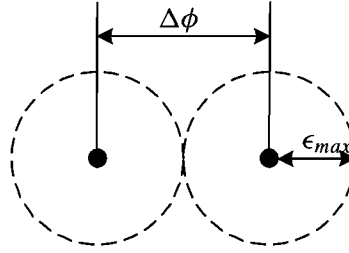


Figure 4.13: Visualisation of the resolution definition, the two black circles indicate the initial source locations and the dotted line represents the allowable error bound.

Using this definition, the resolution of the 3D-tilted cross array used with Unitary ESPRIT is determined. The next figure shows the resolution in the azimuth plane ($\theta = 0$) with an SNR of 25dB and 10 snapshots. From figure 4.14 it can be seen that the resolution varies 6 times about 1 degree in the entire azimuth range, with an average of 3.5 degrees. The expected variation in the performance caused by the difference in aperture as mentioned in chapter 3 is clearly visible in the resolution.

Figure 4.15 shows the resolution in elevation plane ($\phi = 0$) with an SNR of 25dB and 10 snapshots. It can be seen that the resolution in elevation is below four degrees between -30 and 30 degrees and below -50 degrees. One peak in the resolution of about 4.5 degrees can be seen at -40 degrees. This peak, and the other slightly lower peak, are the result of a decrease in elevation aperture. The heights of these two peaks change six times over the entire azimuth range between 4.5 and 4 degrees. Since these peaks are located relatively high in elevation angles, they will not effect the performance significantly.

Figure 4.16 shows the resolution in azimuth ($\theta = 0$) versus the SNR for a different number of snapshots, q . The result shows a similar trend in degradation in the resolution for different values for q . It can clearly be seen that an increased number of snapshots results in a higher resolution performance. The results also show that there is a lower bound for the minimum resolution of about one degree.

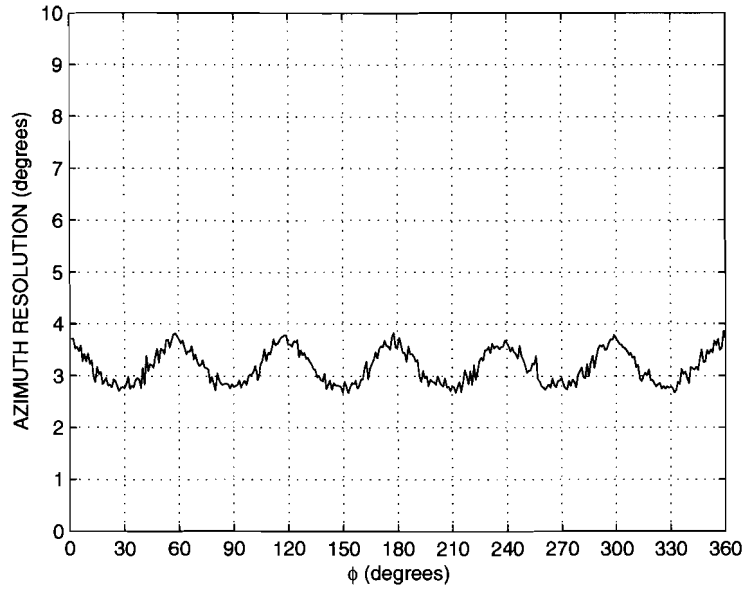


Figure 4.14: Resolution in azimuth at $\theta = 0$ for SNR=25dB and 10 snapshots.

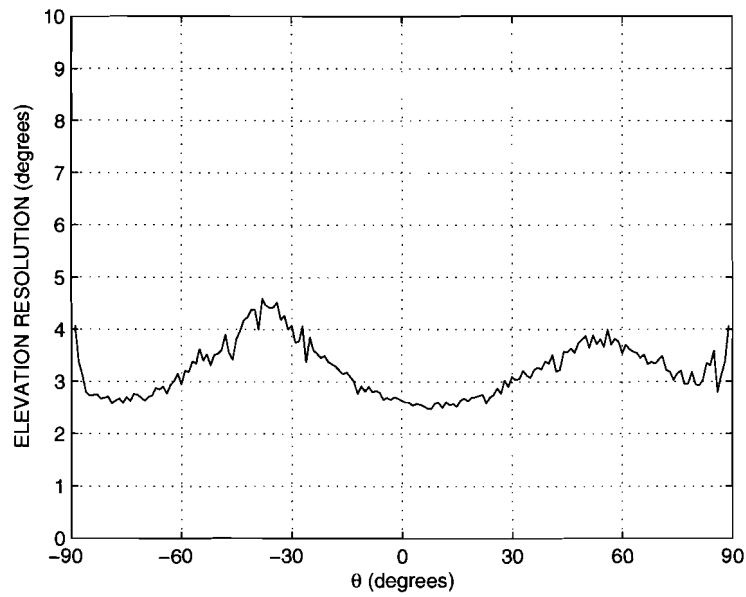


Figure 4.15: Resolution in elevation at $\phi = 0$ for SNR=25dB and 10 snapshots.

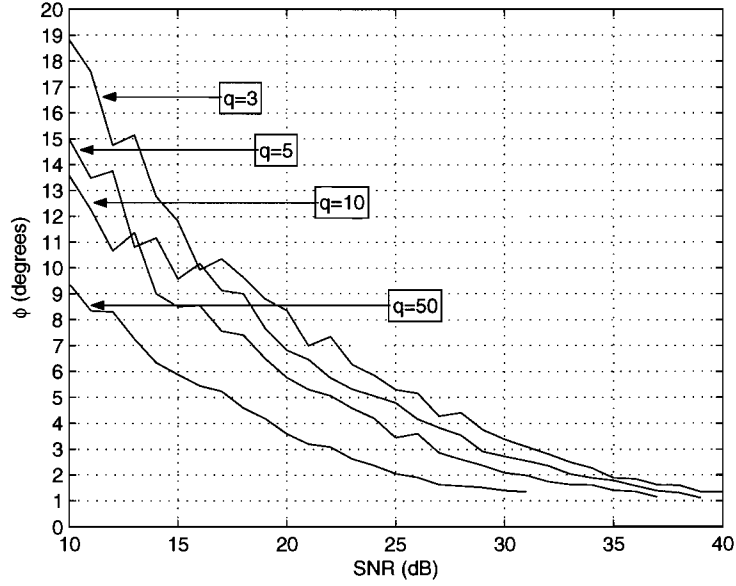


Figure 4.16: Resolution in azimuth versus SNR for $q=3, 5, 10$ and 50 .

4.5 Conclusion

In this chapter it is shown that a variety of high-resolution algorithms are available in the literature. The Unitary ESPRIT algorithm proves to be an efficient high-resolution algorithm that can quite easily be extended to three or more dimensions. Moreover, the Unitary ESPRIT algorithm can be applied to the uniformly spaced 3-D tilted cross array to perform high-resolution DF and signal power estimations over the entire azimuth and elevation range.

To improve the estimation results significantly, an extended SLS method is developed that solves a rank deficiency problem embedded in the algorithm and can solve the invariance equations more accurately.

Simulations have shown that the 3-D tilted cross array in combination with the 3D Unitary ESPRIT algorithm is capable of resolving the true DOAs and the corresponding powers of a number of sources at arbitrary angles. It is also confirmed that the new extended SLS method outperforms all other methods available today.

The estimation accuracy is determined from the simulation results in different scenarios. It is also shown that the 3-D tilted cross array can effectively prevent large estimation errors from occurring in low elevation angles ($-20^\circ < \theta < 20^\circ$).

Simulations show that under typical conditions (SNR=25dB, 10 snapshots) it is possible to obtain less than four degrees resolution in azimuth as well as in elevation.

Chapter 5

Implementation issues

5.1 Introduction

This chapter discusses the implementation of the 3-D antenna array for the new channel sounder. First, the design and implementation of the different parts of the antenna array will be shown together with measurement results that prove the concept of the impedance switching technique. Next, the expected estimation results are presented that take into account the mutual coupling and shadowing effects of the antenna array structure with the impedance switching technique applied to the array. Subsequently, the effects of Doppler are discussed that set a limit to the maximum allowable velocity of the measurement system. Finally, the chapter will be concluded.

5.2 Antenna array

5.2.1 Antenna elements

The antenna elements in the 3-D array are designed as quatre-wavelength drooping-radial monopole antennas. In [3], it is shown that the monopole is a very suitable candidate because of its 50Ω input impedance and its omnidirectional antenna radiation pattern. The initial monopole antenna design described in [3], is further optimised by minor changes as a result of considering the input reflection obtained from the FEKO simulation results. Details on the drooping-radial antenna model used in FEKO can be found in appendix A.1. The final design of the drooping-radial monopole antenna is shown in figure 5.1 (a) and the resulting antenna was built at CRC and is shown in figure 5.1 (b).

During the construction of the monopole antenna elements, hollow wires are used with a outer diameter of 1.5mm and at the antenna feedpoint a female SMA connector is attached to the square support-plane and the active element to allow easy interconnections. An extra margin of 0.05cm is added on top of the length of the active element to be able to tune the individual antennas to the desired frequency of 2.25GHz.

To test the performance of the antenna, the azimuth radiation pattern and the input reflection of the monopole antenna are measured in an anechoic chamber. These measurement results, together with FEKO simulation results are shown in figure 5.2.

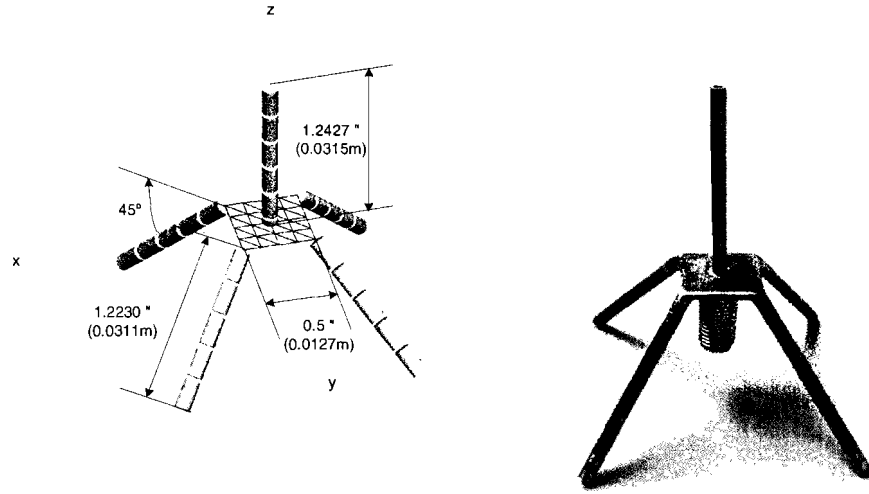


Figure 5.1: Drooping-radial monopole design (a), with the dimensions given in inches (") and in meters (m), and (b) the actual implementation of the antenna.

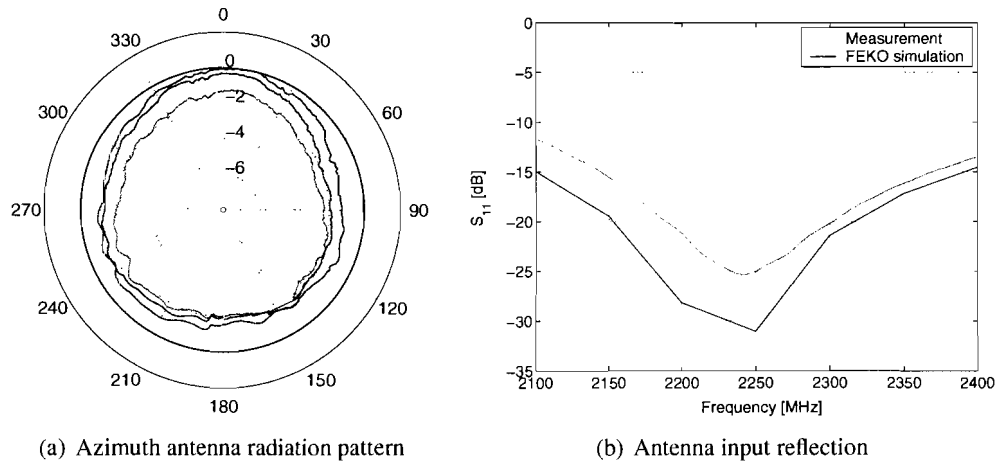


Figure 5.2: Simulation and measurement results of (a) the antenna radiation pattern simulated at 2.25GHz (black) and measured at 2.2GHz (red), 2.25GHz (green) and 2.3GHz (blue), and (b) the antenna input reflection simulated (black) and measured (green).

Because the simulated antenna radiation pattern is identical at the other frequencies, the simulated pattern is only shown at 2.25GHz.

The results in figure 5.2 show that the measurements are largely in agreement with the simulations. The antenna radiation pattern is omnidirectional within 2dB and is consistent over the required 100MHz bandwidth. Most of the 2dB ripple is likely to be caused by scattering effects from parts of the support structure where the antenna was mounted on. This is confirmed by an additional measurement in which the antenna is rotated over 180 degrees in azimuth and the same measurement results were obtained. Extra absorbing material was also added on the support structure to reduce the scattering effects. The results also show that the -15dB bandwidth of the antenna is 200MHz, which is sufficient.

5.2.2 Support structure

In order to position the 31 antenna elements in the 3-D tilted cross configuration and to run cables to each of the antenna elements, a support structure is designed, through which cables can be run and on which the antenna elements are mounted. The initial design of the structure is shown in figure 5.3, with the dimensions given in inches (") and meters (m).

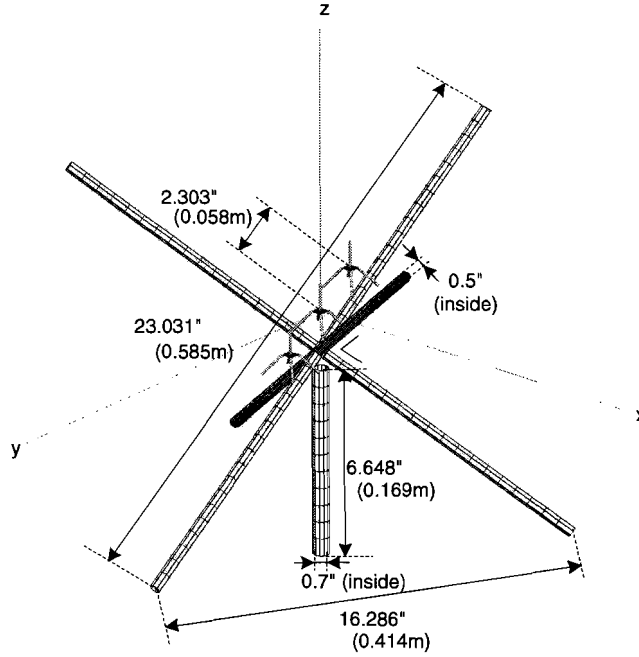


Figure 5.3: Antenna support structure design.

The first implementation of the support structure is built from carbon-fiber tubing material and a polystyrene sphere that holds the carbon tubes. The carbon-fiber material is chosen for its RF absorbing properties, which can help to reduce the scattering effects of incident waves on the cables running through the structure. The polystyrene material is chosen because it is practically RF transparent, and therefore prevents scattering effects.

Through the six diagonal rods, a maximum of five semirigid cables and ten signal cables (two for each antenna) will be run. The minimum diameter d , needed for packing $n = 5$ semirigid cables with a diameter of $d' = 3.58\text{mm}$ in a rod can be calculated as [40]

$$d = d' \left(1 + \sqrt{2(1 + 1/\sqrt{5})} \right) = 9.67\text{mm}. \quad (5.1)$$

Since the diameter of the signal cables can be made small compared to the semirigid, rods with an inner diameter of $d = 0.5'' = 12.7\text{mm}$ are chosen to be sufficient. The cables from the upper three diagonal rods will be run through the centre vertical rod with $d = 0.7'' = 1.78\text{mm}$.

The first version of the array is manufactured with three possible antenna positions to perform initial experiments and to allow for possible design changes. Figure 5.4 shows the support structure populated with two antenna elements, which is used for measurements described in the next section.

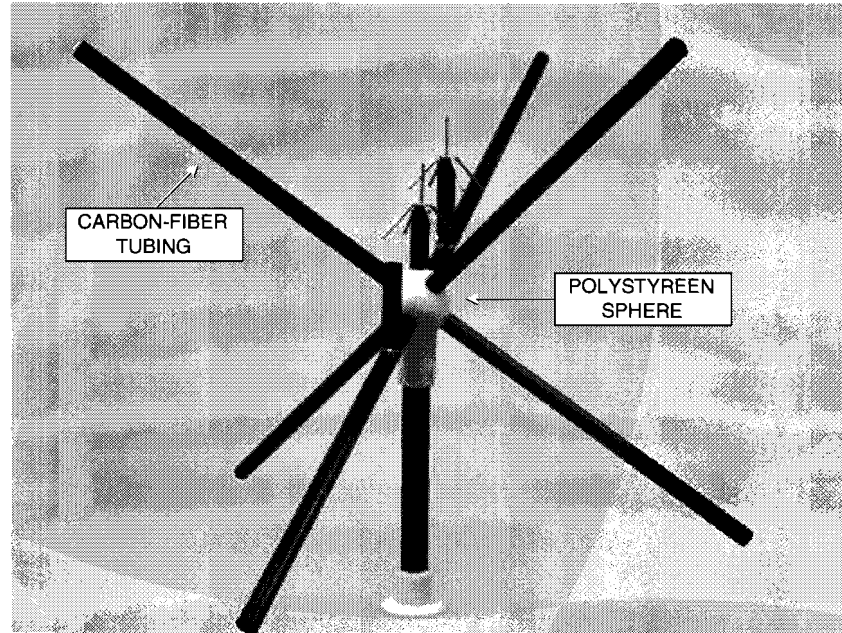


Figure 5.4: Implementation of the carbon-fiber antenna support structure, with three possible antenna element positions.

5.2.3 Antenna switching

The switched antenna array is designed with the idea to connect all antenna elements in the array to the receiver in sequence, as is shown in figure 5.5. To address all 31 antenna elements in sequence, a 31:1 RF switch is used that connects each of the antenna elements to the input of the receiver and is controlled by the data collection system. The antenna switch is mounted on a PCB-board together with the required connectors and will be placed directly underneath the antenna array.

The switched-impedance technique requires the antenna elements to be connected to either the RF receiver via the RF switch or to a complex termination impedance Z_L . To achieve this, each antenna is equipped with an additional 2:1 RF switch that connects the antenna to the complex load, Z_L , in case the antenna is not addressed by the main switch. This switch is mounted on a small PCB-board and attaches directly to the antenna using an SMA-connector. More details on the implementation of the impedance switching technique are presented in the next section.

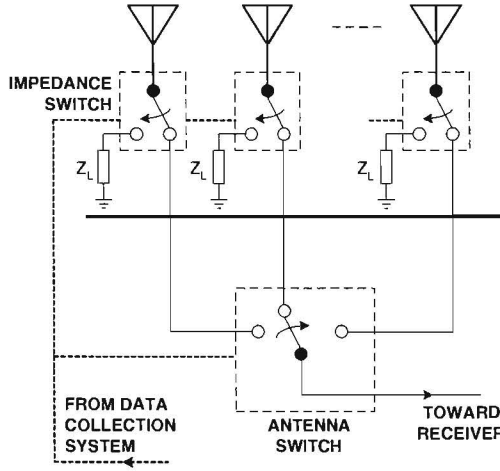


Figure 5.5: Main 31:1 antenna switch and 2:1 impedance switch.

5.3 Impedance switching

5.3.1 Complex impedance

As discussed in section 3.5, it is possible to suppress the mutual coupling effects between the passive and the active antenna elements by terminating the passive elements with a complex load, Z_L . The optimum value for Z_L in the case of the drooping-radial monopole antennas tuned at 2.25GHz is determined from FEKO simulations to be $j250\Omega$. The impedance value of $j250\Omega$ corresponds to an inductor value of 18nH. This is the value seen at the antenna feedpoints. In practice, however, it is inevitable that there is a transmission line between the antenna feedpoints and the actual complex load, which changes the impedance value seen by the antenna.

The input impedance Z_{in} of a lossless transmission line of length l and terminated with Z_L can be determined as [41]

$$Z_{in} = Z_0 \cdot \frac{Z_L \cos \beta l + j Z_0 \sin \beta l}{Z_0 \cos \beta l + j Z_L \sin \beta l} \quad (5.2)$$

with the characteristic impedance of the transmission line $Z_0 = 50\Omega$, and $\beta = \frac{2\pi}{V_f \lambda}$, where V_f is the velocity factor of the transmission line, which indicates the propagation speed of the signal along the transmission line with respect to the speed of light. The velocity factor is almost entirely dependant on the dielectric constant ϵ_r of the insulation material and can be defined as

$$V_f = \frac{1}{\sqrt{\epsilon_r}}. \quad (5.3)$$

Instead of using a lumped element connected to the antenna via a transmission line, the transmission line itself can be used to create the proper impedance seen at the antenna feedpoints. In figure 5.6 the length of a *shorted* piece of transmission line versus the complex impedance seen at the end of the line is shown with a typical value of $VF = 0.7$.

From figure 5.6 it can be seen that the impedance value of $j250\Omega$ can be obtained with many different lengths. It is however an advantage to choose the shortest length of semirigid for which this value can be achieved, since this minimises the frequency spread.

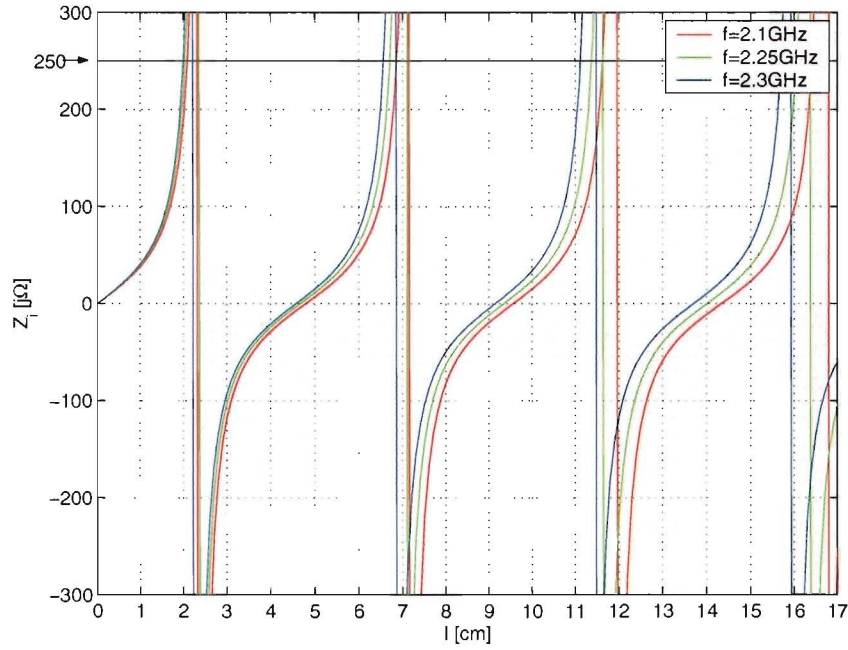


Figure 5.6: Complex impedance versus transmission line length for $f=2.2\text{GHz}$ (red), $f=2.25\text{GHz}$ (green) and $f=2.3\text{GHz}$ (blue).

Using the result in figure 5.6, a piece of semirigid was cut at the about 2cm length and tuned with a network analyser to be $j250\Omega$ at the antenna feedpoints.

5.3.2 Prove of concept

To prove the concept of suppressing the mutual coupling effects using a complex load at the passive elements, measurements are performed that are in line with simulations presented in [2]. The measurements are performed in an anechoic chamber with two antenna elements separated by $d = 0.45\lambda$. One of the elements is passive, and terminated with either the $Z_L = 50\Omega$ system impedance, or with $Z_L = j250\Omega$ by means of the tuned piece of semi-rigid. The active element is driven by a narrowband voltage signal through a $50\text{-}\Omega$ transmission line. The setup is visualised in figure 5.7.

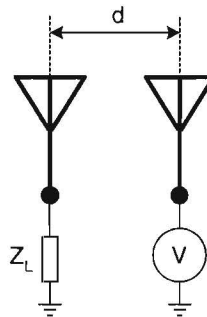


Figure 5.7: Measurement-setup for two antenna elements to prove the concept of mutual coupling suppression.

With this setup, the antenna pattern in elevation (E-plane) and in azimuth (H-plane) as well as the input reflection are measured at different frequencies and the results are presented in figures 5.8 and 5.9.

The results in figure 5.8 show that the antenna radiation pattern can be improved significantly if the passive antenna is terminated with $j250\Omega$ instead of the more common 50Ω . It is clearly visible that the measurement results are in line with the simulations. The additional distortion on the measured pattern is likely to be caused by scattering effect of the measurement setup. The results in 5.9 confirm that the antenna radiation pattern improves while the passive antenna is terminated with $j250\Omega$. Also, the input reflection shows a large improvement and the measurement results are in line with the simulations.

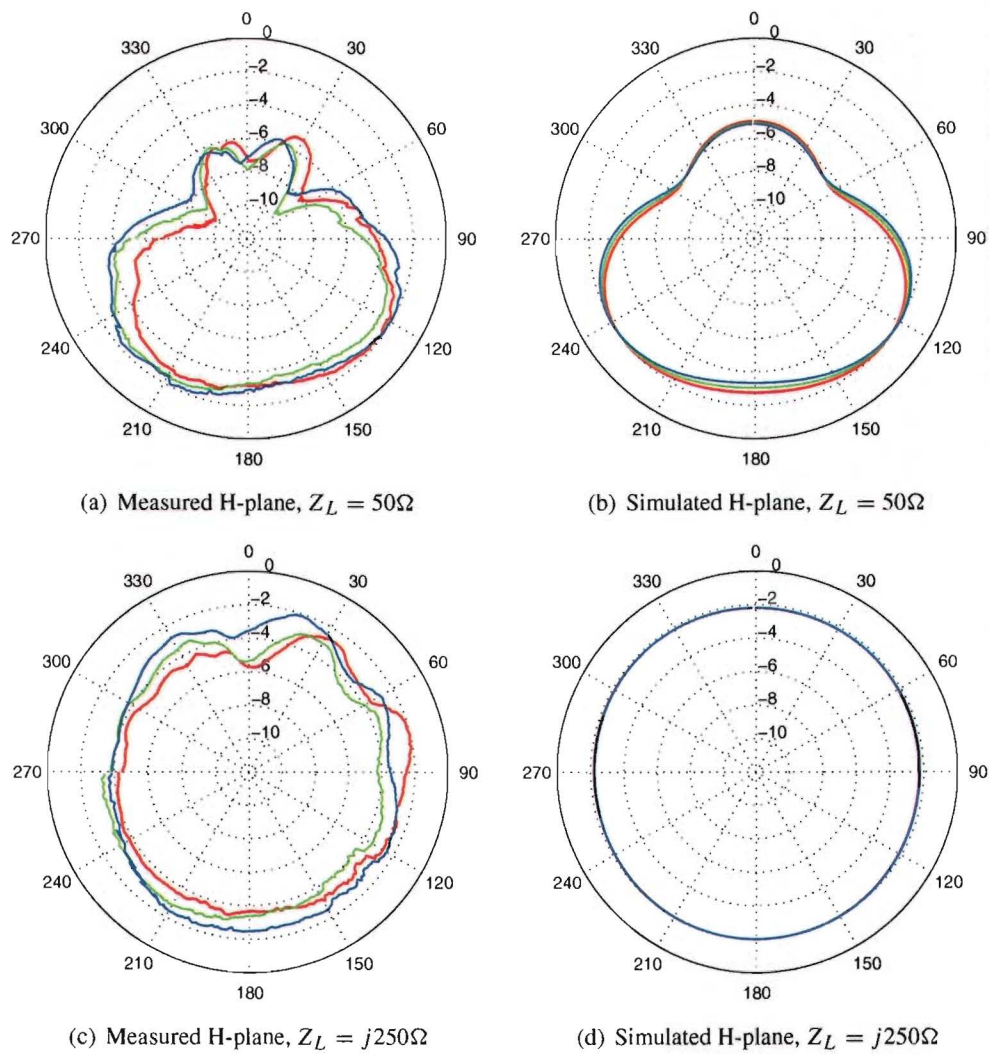
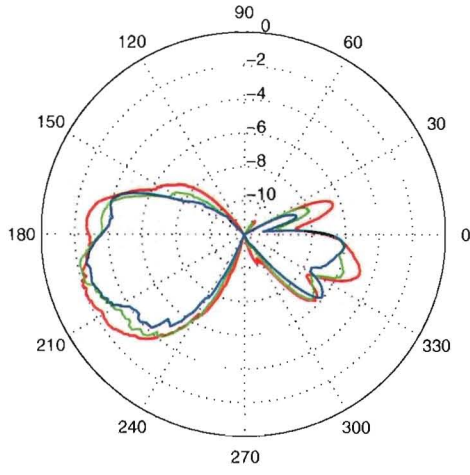
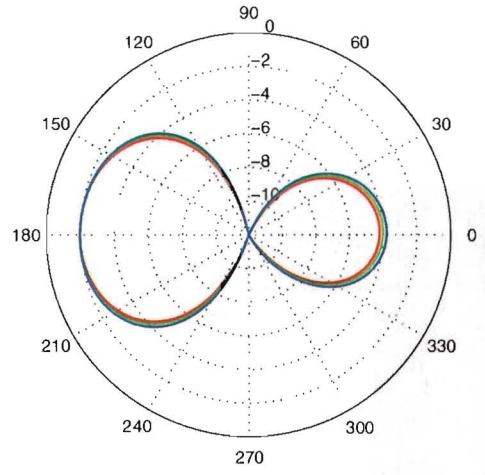


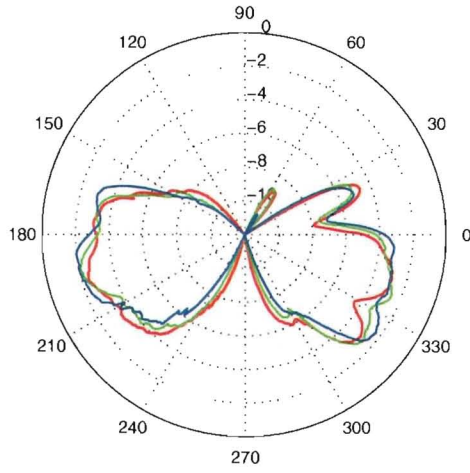
Figure 5.8: Measurement and simulation results of two antenna setup at 2.2GHz (red), 2.25GHz (green) and 2.3GHZ (blue) with $Z_L = 50\Omega$ and $Z_L = j250\Omega$.



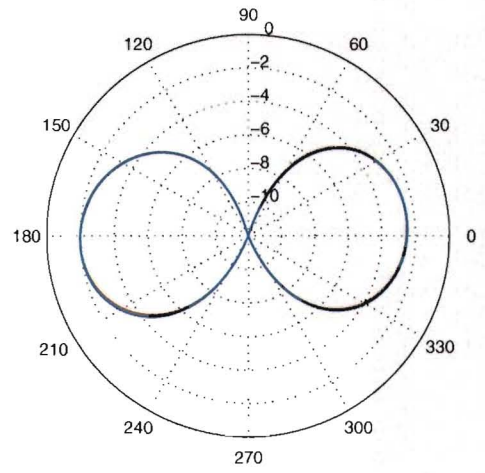
(a) Measured H-plane, $Z_L = 50\Omega$



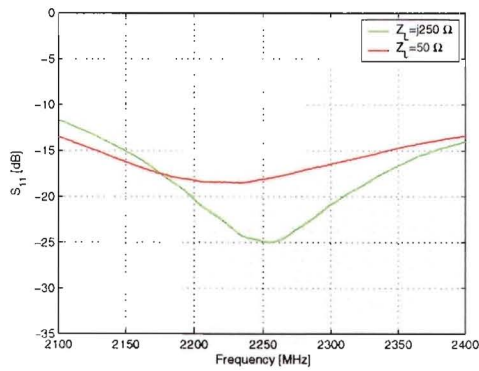
(b) Simulated H-plane, $Z_L = 50\Omega$



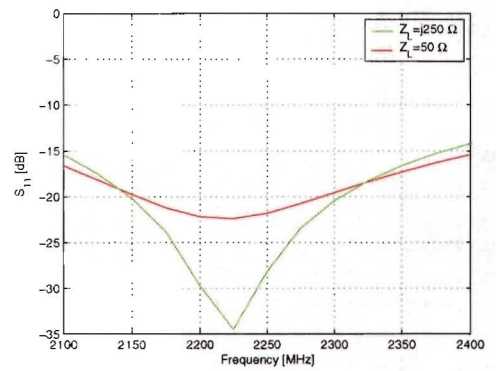
(c) Measured H-plane, $Z_L = j250\Omega$



(d) Simulated H-plane, $Z_L = j250\Omega$



(e) Measured input reflection



(f) Simulated input reflection

Figure 5.9: Measurement and simulation results of two antenna setup at 2.2GHz (red), 2.25GHz (green) and 2.3GHz (blue) with $Z_L = 50\Omega$ and $Z_L = j250\Omega$.

5.3.3 Carbon support structure

To investigate the concept of suppressing the mutual coupling effects in the carbon fiber support structure, similar measurements are performed in the anechoic chamber with two antenna elements located on the carbon fiber support structure. One of the elements positioned in the centre is used as the active element, while the other element is connected to either the $250j\Omega$ tuned load or a 50Ω load and positioned either diagonally above (B) or below (A) the active element, as is shown schematically in figure 5.10 and in figure 5.11. The results of these measurements together with simulation results from FEKO are shown in figures 5.12 and 5.13.

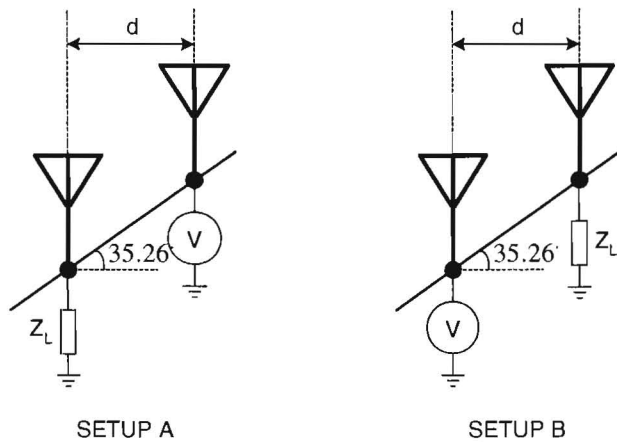


Figure 5.10: Measurement-setup for two antenna elements to prove the concept of mutual coupling suppression.

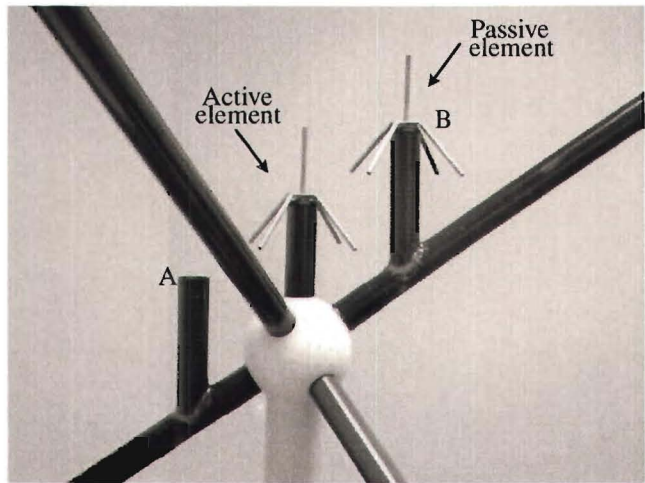
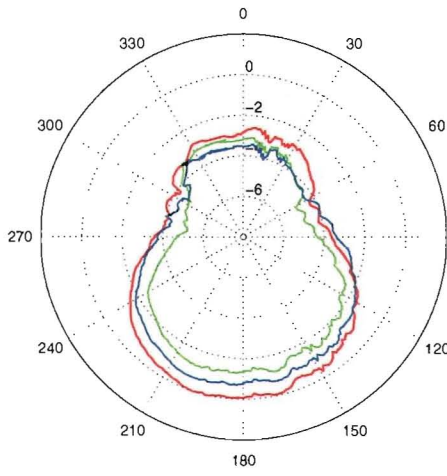
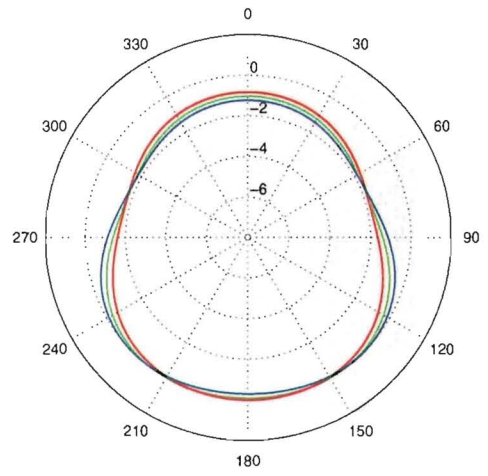


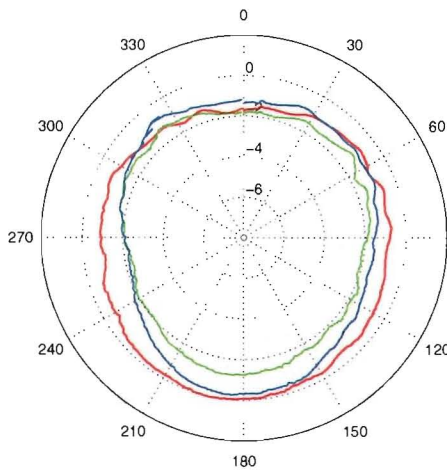
Figure 5.11: Antenna element setup in first array implementation.



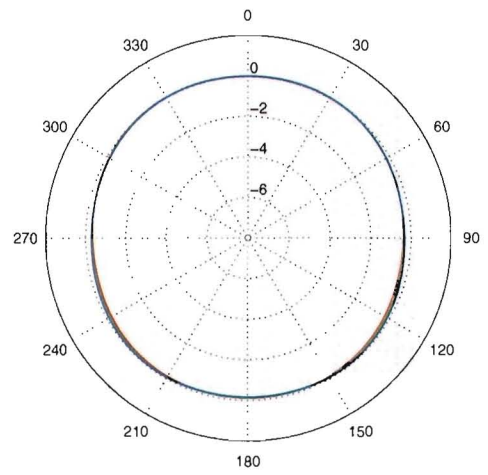
(a) Measured H-plane, $Z_L = 50\Omega$



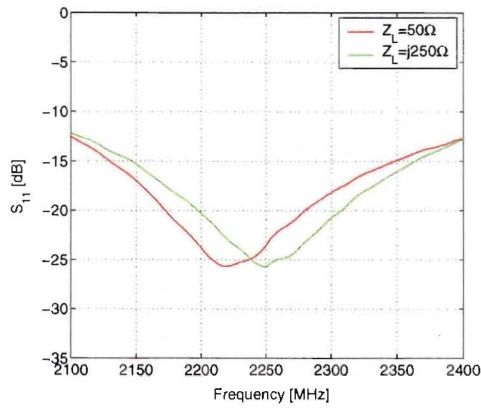
(b) Simulated H-plane, $Z_L = 50\Omega$



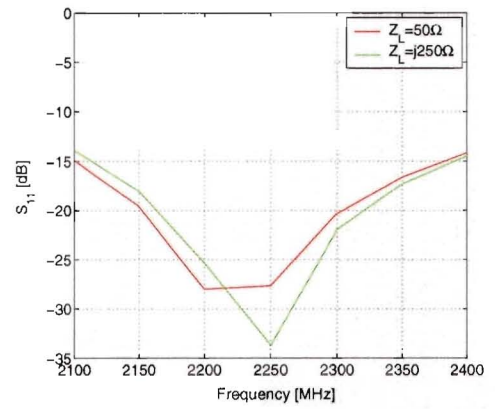
(c) Measured H-plane, $Z_L = j250\Omega$



(d) Simulated H-plane, $Z_L = j250\Omega$

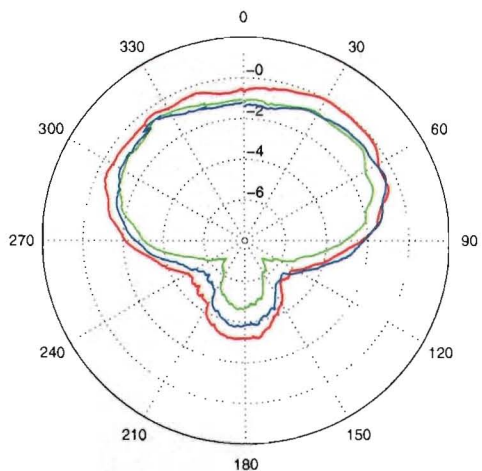


(e) Measured input reflection

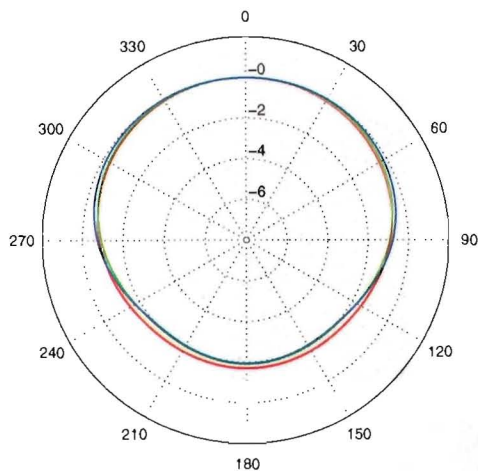


(f) Simulated input reflection

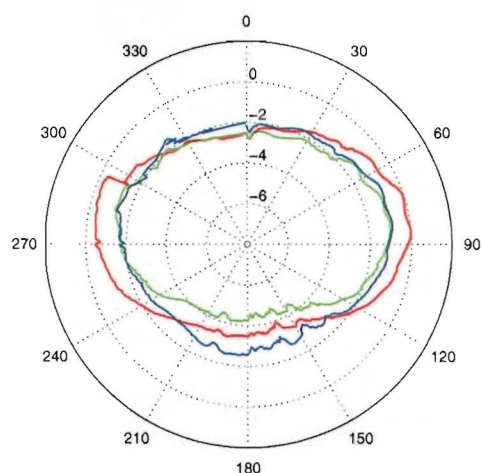
Figure 5.12: Measurement and simulation results of two antenna setup A at 2.2GHz (red), 2.25GHz (green) and 2.3GHz (blue) with $Z_L = 50\Omega$ and $Z_L = j250\Omega$.



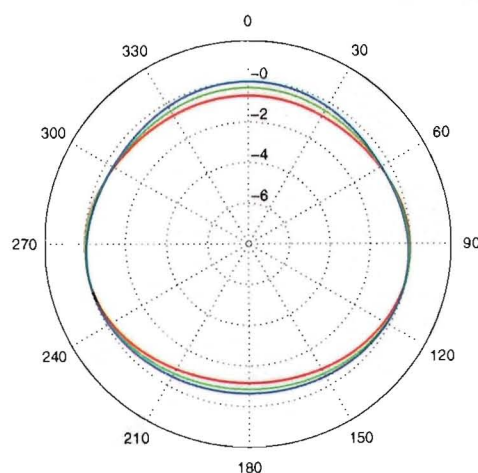
(a) Measured H-plane, $Z_L = 50\Omega$



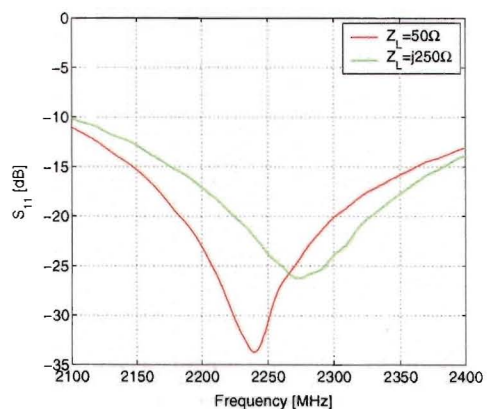
(b) Simulated H-plane, $Z_L = 50\Omega$



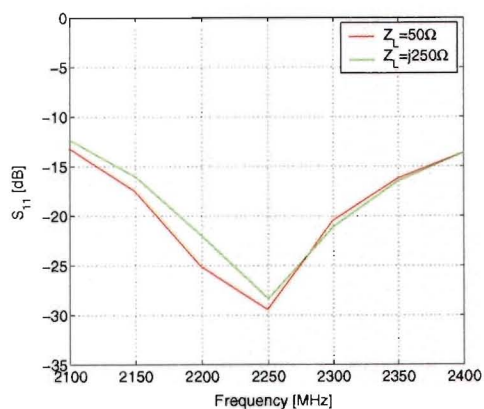
(c) Measured H-plane, $Z_L = j250\Omega$



(d) Simulated H-plane, $Z_L = j250\Omega$



(e) Measured input reflection



(f) Simulated input reflection

Figure 5.13: Measurement and simulation results of two antenna setup B at 2.2GHz (red), 2.25GHz (green) and 2.3GHz (blue) with $Z_L = 50\Omega$ and $Z_L = j250\Omega$.

The results clearly show an improvement of the omni-directionality in the antenna radiation pattern when the $j250\Omega$ load is used on the passive elements. Especially in setup A, the measurement results are in agreement with the simulations. The difference between the simulations and the measurements in setup B can be explained by the fact that the complex impedance connected to the passive element, a 2cm piece of semirigid, is positioned at approximately the same level as the active antenna and therefore more actively disturbs the pattern. In the FEKO simulations, this actual piece is not present.

5.3.4 Expected results

To give an indication of the estimation results with mutual coupling and shadowing effects present, the antenna array and the support structure are modelled in FEKO and the far-field output data from the simulations is used as input in the Unitary ESPRIT algorithm. The antenna array model with support structure modelled in FEKO is shown in figure 5.14.

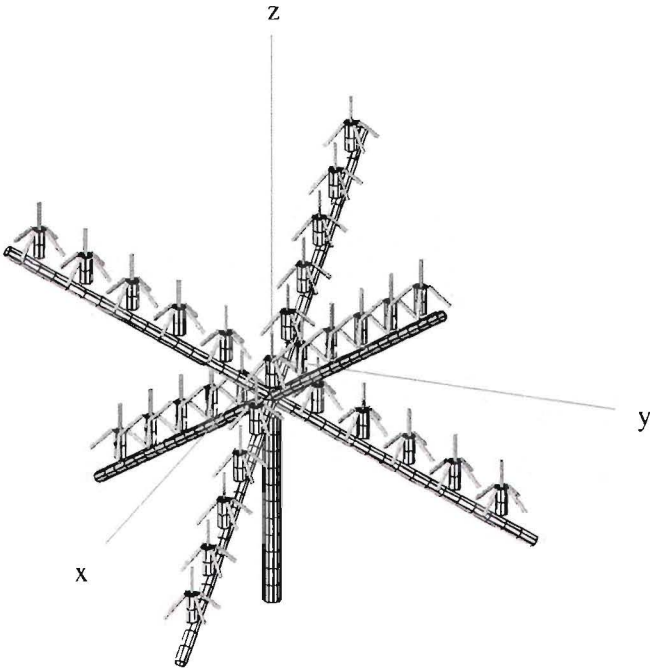
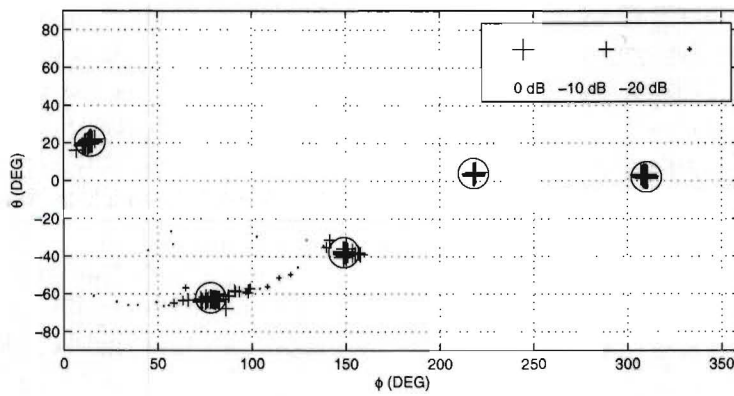
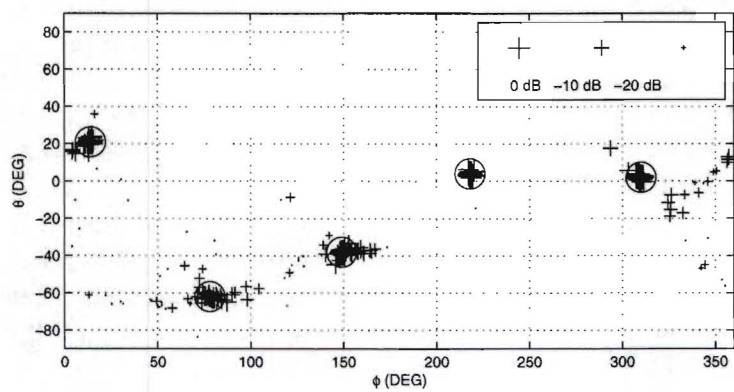


Figure 5.14: 3-D tilted cross array with support structure modelled in FEKO.

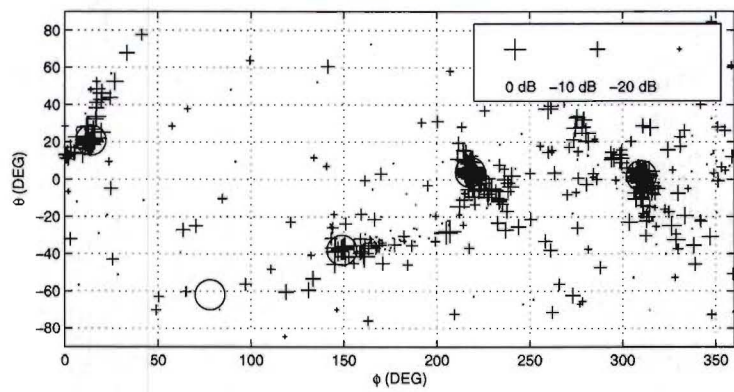
To compare these results with the previous idealistic results, the same simulations as described in section 4.4.2 are performed. The results in figure 5.15 show that the algorithm is still capable of resolving the true DOAs and corresponding powers in the low elevation angles at an SNR of 35dB. A number of spurious estimates occur in the higher elevation angles and at lower SNR levels. Although these spurious estimates occur, the estimated power can still give an indication of the reliability of the estimation.



(a) SNR=35dB



(b) SNR=25dB



(c) SNR=15dB

Figure 5.15: DOA estimation using five incident waves, 10 snapshots and SNR levels of 35, 25 and 15dB.

5.4 Doppler Considerations

The measurement equipment is intended to be used for mobile DF measurements, which means Doppler effects have to be taken into account. During measurements, the antenna array is moving with respect to its environment through a stationary electromagnetic field that is caused by the incident waves. When one snapshot of the array is taken (31 elements are sampled), it is important that all antennas in the array are sampled long before the array has travelled a significant distance through the spatial fluctuations of amplitude and phase of the EM field. Because the spatial period of these fluctuations is at least one wavelength, all elements have to be sampled before the antenna array has travelled a significant percentage of the wavelength.

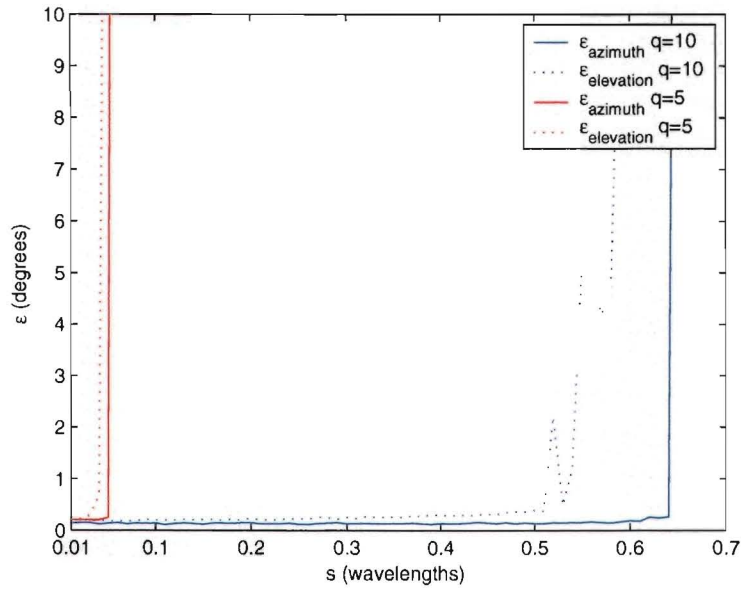
It should be noted that the spatial fluctuations are maximal if the antenna array is travelling in the same or the exact opposite direction of the incident wave. If the incident waves arrive from a direction perpendicular to the moving direction of the array, the effects are minimised.

Simulations are performed using different scenarios to determine the minimum distance, S_{min} , that can be travelled during one snapshot. Figure 5.16 shows the angular estimation error, ϵ , in azimuth and elevation versus the travelled distance, S , of the array during one snapshot. The different results all show an abrupt increase in the estimation error at a certain value for S . From these results it can be concluded that choosing a maximum travelled distance of 1/100th of a wavelength or less in all scenarios keeps the estimation error at a sufficiently low level.

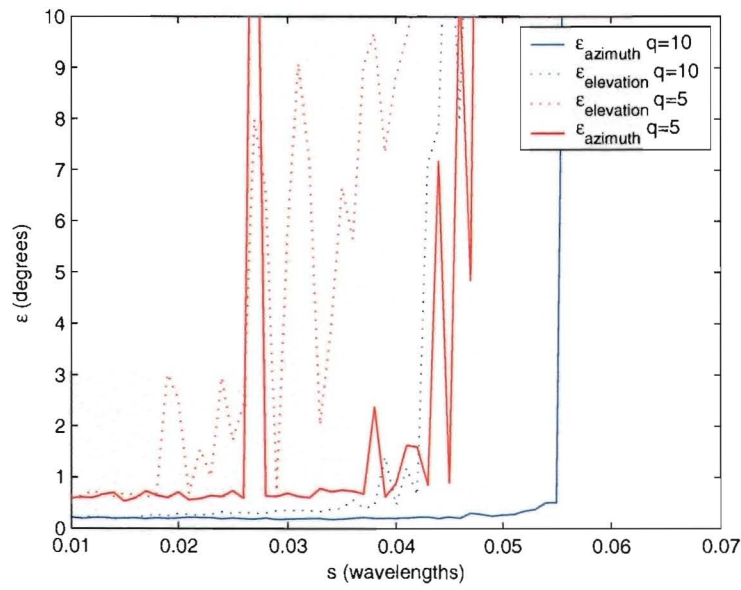
Recall that the bit rate of the PN sequence is 50Mbit/s and that 255 bits of 20ns each are used for one CIR. This means that the duration of one sequence of 255 bits is $5.1\mu s$. The acquisition time of one snapshot t_{snap} is therefore equal to $5.1\mu s$ times 31 antennas, which equals $158\mu s$. With a maximum allowable travelled distance of $\lambda/100$, the maximum allowable speed of the measurement vehicle can be determined from

$$V_{max} = \frac{0.01\lambda}{t_{snap}} \quad (5.4)$$

to be 8.4m/s or 30km/h. This measurement speed is expected to be sufficient to perform mobile DF measurements in urban microcell environments.



(a) SNR=25dB



(b) SNR=15dB

Figure 5.16: Travelled distance S versus the estimation error ϵ in azimuth (solid line) and elevation (dotted line) for 5 (red) and 10 (blue) snapshots, and (a) SNR=25dB and (b) SNR=15dB.

5.5 Conclusion

In this chapter the design and implementation of the drooping-radial monopole antenna elements are shown. Measurement results from this antenna seem to match the simulation results and show that the antenna is a suitable candidate for the 3D antenna array.

A carbon-fiber support structure that positions the antenna elements and guides the cables to the antenna switch is presented and partly implemented. This support structure proved to be very suitable for positioning two antenna elements in the array structure and to perform preliminary measurements.

It is shown that a tuned transmission line can be used as a $j250\Omega$ complex impedance load to terminate the passive antenna elements. Measurements have shown that the technique of terminating the passive elements with a complex load can help to suppress the mutual coupling effects in an array geometry. The measurements show the best results in planar array geometries.

Simulations that use the output data from FEKO have shown that the mutual coupling and shadowing effects, which disturb the properties of the antenna elements, cause some degradation in the DF performance.

To prevent large errors in the DF measurements, Doppler effects have to be considered, which limit the maximum speed of the measurement system. Simulation have shown that under typical conditions reliable measurements with the new system are still possible at a speed of about 30Km/h.

Chapter 6

Conclusions and recommendations

This chapter summarises the conclusions drawn along this thesis and presents recommendations to the work.

6.1 Conclusions

The mobile channel sounder currently operational at the TU/e is capable of measuring the directions-of-arrivals (DOAs) of incident waves using a synthetic uniform-circular-array (UCA). The work presented in this thesis concerns the upgrade of the existing direction-finding (DF) system in order to improve the performance. Improvements in performance mainly concern the elevational resolution and the possibility to perform mobile DF measurements. The results from mobile measurements can provide more information about the change in composition of the radio propagation in the mobile channel, which can be used for more efficient planning of microcellular radio networks and provide a basis for the design of radio systems that are better matched to the real-world behaviour of urban radio channels.

It is shown that compared to the UCA array, an Y-shaped antenna geometry with the same number of antenna elements increases the azimuth resolution by reducing the azimuth half-power-beamwidth (HPBW) from eight to six degrees. To improve the resolution in elevation and to remove the two-fold ambiguity that exists with horizontal planar arrays, the Y-shaped array design is used as a basis from which a 3-D antenna array is constructed. The resulting 3-D tilted cross array can provide uniform and equal resolution in azimuth as well as in elevation. The HPBW of this 3-D array is 16 degrees in both directions, which means a degradation in azimuth resolution, but a significant improvement of elevation resolution compared to the elevation HPBW of roughly 40 degrees with the current UCA.

The aperture of the array, and therefore the resolution, can be doubled by applying non-uniform element separation. This can however cause the side-lobe-levels (SLLs) to rise. This effect can be minimised by finding the optimal positions of the antenna elements that correspond to the lowest possible SLLs. These positions cannot be determined analytically, therefore optimisation techniques are used to find the optimal sensor positions. The non-uniform element separation in the 3-D tilted cross array causes the SLLs to rise about one degree.

Simulations have shown that in a switched antenna array the mutual coupling effects between the active and the passive elements can be suppressed by terminating the passive elements in $j250\Omega$. This technique proves to be very effective in all array geometries, but

especially in the planar geometries. The radiation pattern distortion of the antenna elements in the Y-shaped array can be reduced from about 6dB to about 1dB, whereas with the 3-D tilted cross array this reduces from 4dB to 2dB. The distortion of the phase pattern is with the Y-shaped array reduced from roughly 70 degrees to about 7 degrees and with the 3-D tilted cross array to 25 and 12 degrees.

After analysing a number of high-resolution DOA algorithms, the Unitary ESPRIT algorithm proves to be a very accurate and computational efficient algorithm that can easily be extended into more dimensions. The algorithm requires the antenna array to be centrosymmetry and to have uniform element spacing, which makes the uniformly spaced 3-D tilted cross array an ideal candidate.

The Unitary ESPRIT algorithm is extended into three dimensions and applied to the 3-D tilted cross array. To further improve the estimation results and to solve a rank deficiency problem embedded in the algorithm, an improved structured-least-squares (SLS) technique is developed that can solve the invariance equations more accurately. It is also confirmed that this new extended SLS method outperforms all other methods available today.

Simulations have shown that the 3-D tilted cross array in combination with the 3-D Unitary ESPRIT algorithm and the improved SLS technique is capable of resolving the true DOAs and the corresponding powers of a number of sources at arbitrary angles with typical values for the SNR. The estimation accuracy is determined from the simulation results in different scenarios. Simulations show that under typical conditions (SNR=25dB, 10 snapshots) it is possible to obtain less than four degrees resolution in azimuth as well as in elevation. At low SNR levels the DF estimation accuracy becomes rather poor.

Measurement results from the implementation of the drooping-radial monopole antennas seem to agree with simulation results obtained from an EM simulation package called FEKO and show that the drooping-radial monopole is a suitable candidate for the antenna elements in the 3D antenna array.

It is shown that a tuned transmission line can be used as a complex impedance load to terminate the passive antenna elements, and measurements confirm that the technique of terminating the passive elements with a complex load can help to suppress the mutual coupling effects in an array geometry. The measurements show the best results in planar array geometries.

A carbon-fiber support structure that positions the antenna elements and guides the cables to the antenna switch is presented and partly implemented. This support structure proves to be suitable for positioning two antenna elements and to perform preliminary measurements.

Simulations that use the output data from FEKO have shown that the mutual coupling and shadowing effects, which disturb the properties of the antenna elements, cause some degradation in the DF performance.

To prevent large errors in the DF measurements, Doppler effects have to be considered, which limit the maximum speed of the measurement system. Simulation have shown that under typical conditions reliable measurements with the new system are still possible at a speed of about 30Km/h.

6.2 Recommendations

In the near future, the antenna support structure should be finalised and populated with 31 elements including the impedance switches and cables. The effect of the switched impedance

technique should be verified by addressing the switches in the proper way and measuring the effect on the antenna performance. To prevent scattering effects, absorbing material should be used to cover the parts of the support structure.

Initial tests have to be performed in an anechoic chamber to prove the technique of DF with the 3-D tilted cross array in combination with the Unitary ESPRIT algorithm.

After the initial tests have proved to be successful, the system can be installed on the measurement vehicle and measurements in an actual urban environment can be performed. To prevent damage to the array caused by wind weather effects, a radome should be constructed that fits over the array structure and has minimal effect on the propagating radio waves.

Additionally, more research is required to find out why exactly $j250\Omega$ performs so well in suppressing the mutual coupling effects between monopole antenna elements. Different type of antennas at different frequencies should be investigated to find out if similar methods can be applied.

To make the measurement system usable for other type of measurements, such as indoor measurements, or measurement with higher velocities, the system should be investigated while operating with a limited number of elements, i.e. 25, 19, 13, or 7 elements.

Also, the newly developed SLS method should be investigated further on different type of array geometries to test its benefits.

Appendix A

FEKO modelling

A.1 Skirted monopole

The 45-degree drooping-radial monopole design used in the FEKO simulations is shown in figure A.1. The wires are segmented into segments with a maximum length of $\lambda/20$. The length of the wires is chosen 7% shorter than $\lambda/4$ to have the lowest input reflection at 2.25GHz. The radius of the wires is chosen to be 1.5mm. The planar support plane that connects the radials measures $12\text{mm} \times 12\text{mm}$, and is divided into 32 triangles with a maximum edge length of $\lambda/40$. The feedpoint of the antenna is located immediately above the planar support plane under the vertical wire and is represented by a wire segment of length $\lambda/80$.

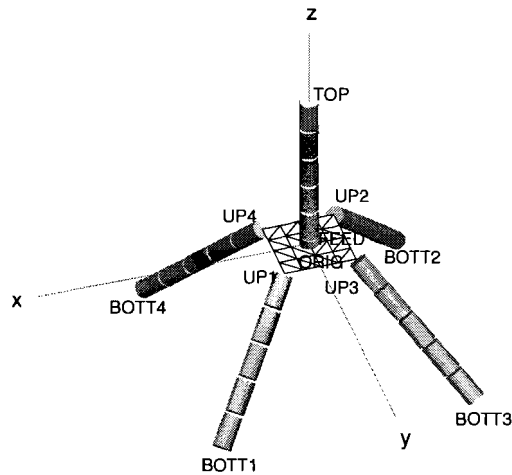


Figure A.1: Skirted monopole antenna modelled in FEKO.

The FEKO geometry code for the 45-degree drooping-radial monopole antenna is shown next.

```

----- Start FEKO code -----

** -----General parameters -----
#MAXNV = 10000          ** Set maximum number of connection points
#freq = 2.25e9          ** The centre frequency wavelength
#lam = #c0/#freq        ** Wavelength

**-----Segmentation parameters-----
#segrad = 0.0015        ** Segment radius
#tri_len = #lam/40       ** Triangle length
#seglen=#lam/20          ** Segmentation length

IP                      #segrad  #tri_len  #seglen  0.02

** -----Geometry variables-----
#ska = (#pi/180)*45      ** skirt angle relative to the el.
#ska2 = (#pi/180)*45     ** skirt angle relative to the az.

#sf=0.233                ** factor - quarter of wavelength
#gap = #lam/80           ** gap between the feed and support

#radp = #lam/22          ** radial start plane dimension

#lenm = #lam*#sf          ** monopole length

#lenvr = #lenr*sin(#ska)+#radv ** vertical reach of radials
#skp = #radp+#lenhr*cos(#ska2) ** x,y value of the legs lower point

** -----Define points for first element-----
DP   top                #x0      0          #lenm
DP   feed               #x0      0          #gap
DP   orig               #x0      0          0

DP   up1                #radp+#x0 #radp      0
DP   up2                -#radp+#x0-#radp  0
DP   up3                -#radp+#x0#radp  0
DP   up4                #radp+#x0 -#radp  0

LA   1
DP   bott1              #skp+#x0  #skp      -#lenvr
DP   bott2              -#skp+#x0 -#skp      -#lenvr
DP   bott3              -#skp+#x0 #skp      -#lenvr
DP   bott4              #skp+#x0 -#skp      -#lenvr

** -----Create wire segments for legs-----
LA   2
BL   up1  bott1

```

```
BL up2 bott2
BL up3 bott3
BL up4 bott4
```

```
** -----Create the top half of the dipole-----
```

```
LA 3
BL top feed
```

```
** -----Create the feed-----
```

```
LA 4
BL Orig Feed
```

```
** -----Create the leg support-----
```

```
LA 5
BQ up1 up3 up2 up4
```

```
_____ End of FEKO code _____
```

Appendix B

Switched-impedance simulation results

This section presents details on the impedance switching simulation results obtained from FEKO and used in section 3.6.3.

B.1 Uniform Y-shaped array

Figures B.1 to B.6 show the results for the uniform Y-shaped array.

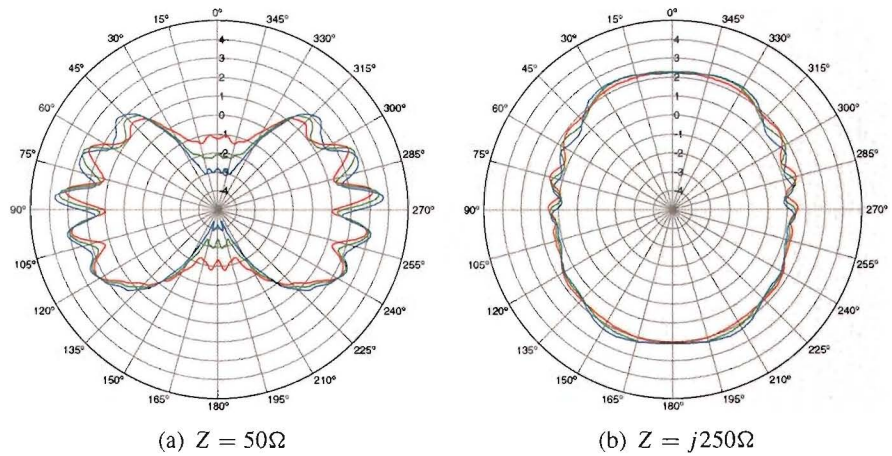


Figure B.1: Element radiation pattern of the 6th element in the uniform Y-shaped array at 2200MHz (red), 2250MHz (green) and 2300MHz (blue) with $Z = 50\Omega$ (a) and $Z = j250\Omega$ (b).

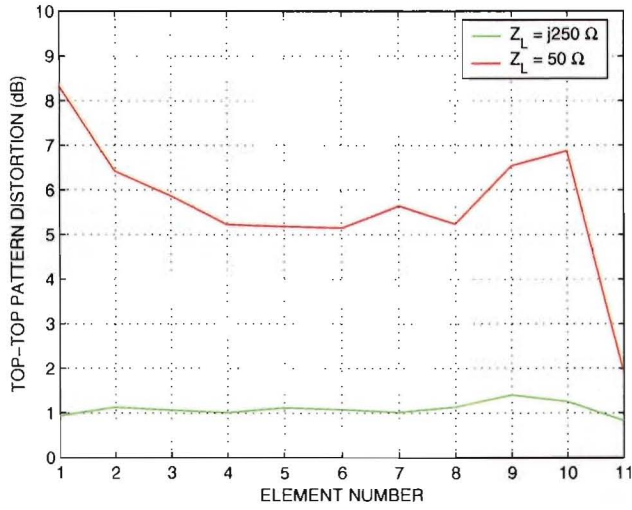


Figure B.2: Top-top radiation pattern distortion versus element number (1 is centre element) in one arm of the uniform Y-shaped array, with $Z_L = 50\Omega$ (red) and $Z_L = j250\Omega$ (green).

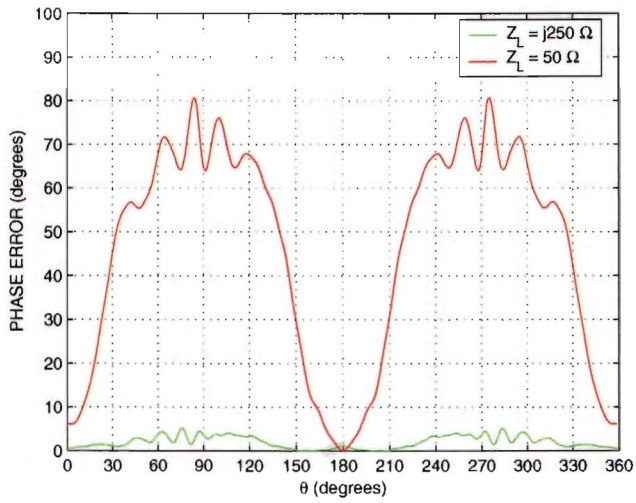


Figure B.3: Phase error of the 6th element in the uniform Y-shaped array, with $Z_L = 50\Omega$ (red) and $Z_L = j250\Omega$ (green).

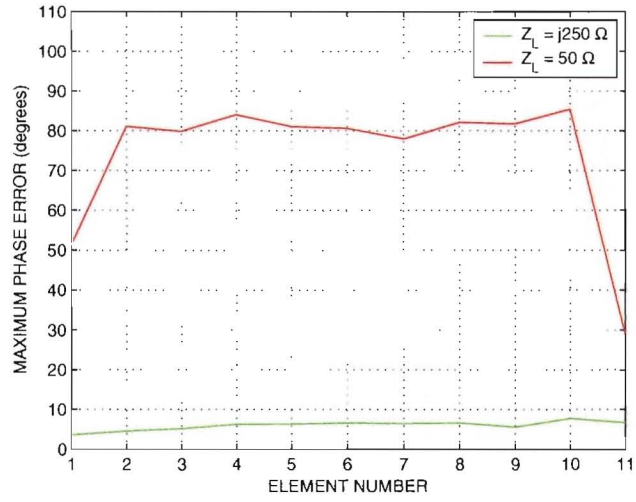


Figure B.4: Maximum phase error versus element number (1 is centre element) in one arm of the uniform Y-shaped array, with $Z_L = 50 \Omega$ (red) and $Z_L = j250 \Omega$ (green).

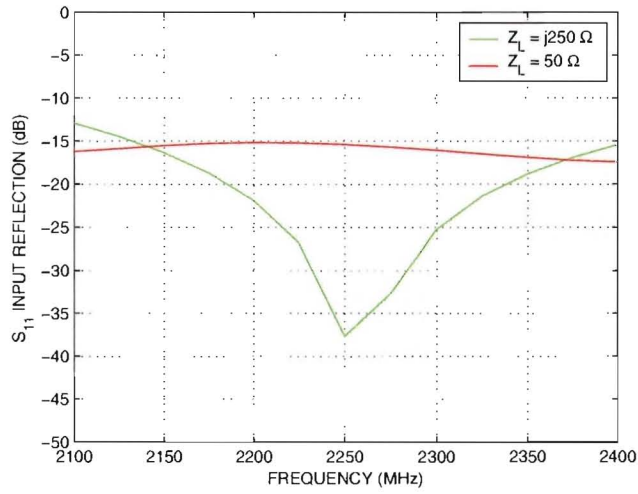


Figure B.5: Input reflection of the 6th element in the uniform Y-shaped array, with $Z_L = 50 \Omega$ (red) and $Z_L = j250 \Omega$ (green).

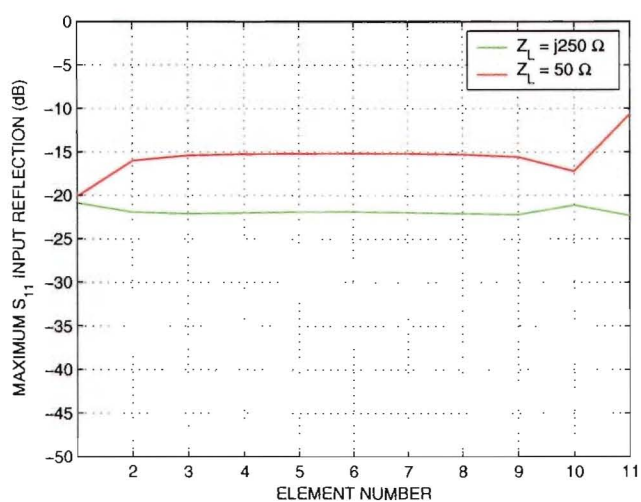


Figure B.6: Maximum input reflection between 2.2GHz-2.3GHz versus element number (1 is centre element) in one arm of the uniform Y-shaped array, with $Z_L = 50\Omega$ (red) and $Z_L = j250\Omega$ (green).

B.2 Non-uniform Y-shaped array

Figures B.7 to B.12 show the results for the non-uniform Y-shaped array.

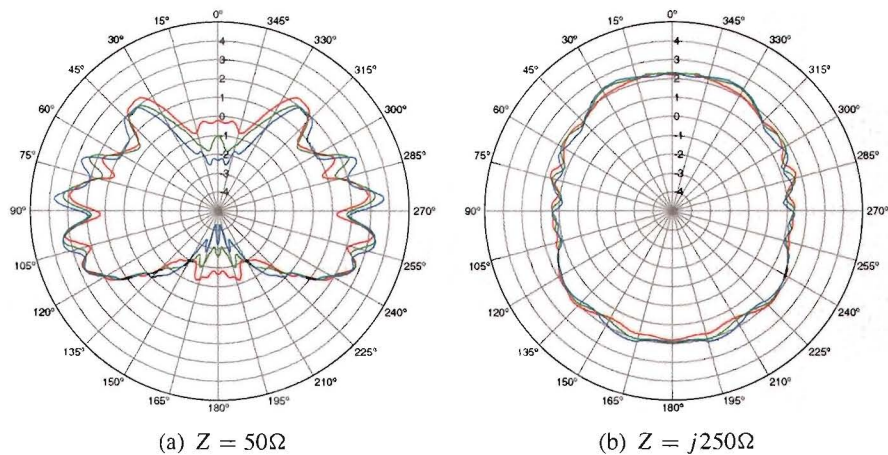


Figure B.7: Element radiation pattern of the 6th element in the non-uniform Y-shaped array at 2200MHz (red), 2250MHz (green) and 2300MHz (blue) with $Z = 50\Omega$ (a) and $Z = j250\Omega$ (b).

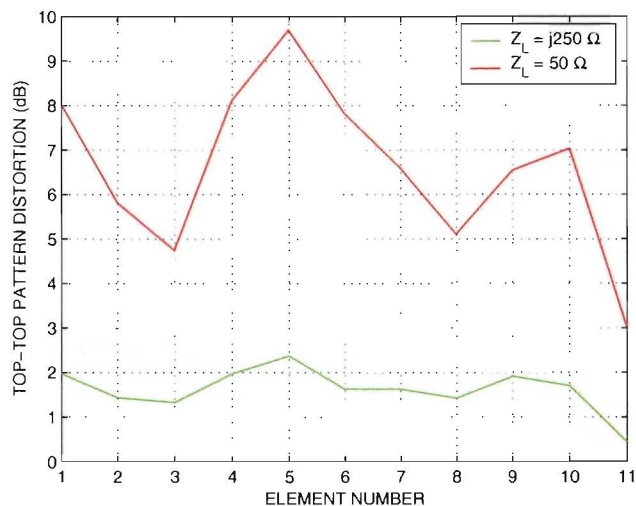


Figure B.8: Top-top radiation pattern distortion versus element number (1 is centre element) in one arm of the non-uniform Y-shaped array, with $Z_L = 50\Omega$ (red) and $Z_L = j250\Omega$ (green).

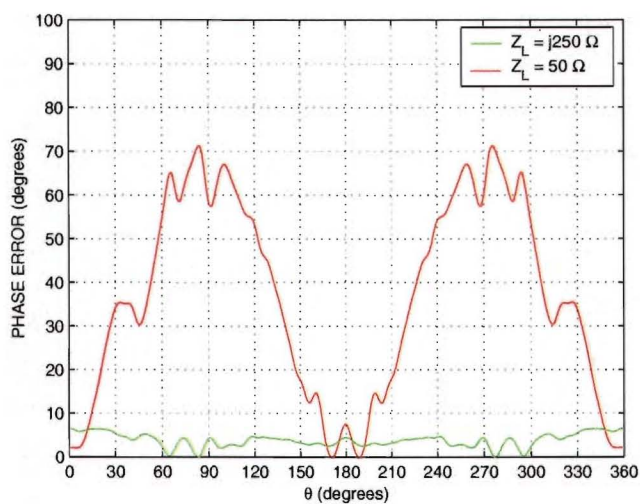


Figure B.9: Phase error of the 6th element in the non-uniform Y-shaped array, with $Z_L = 50\Omega$ (red) and $Z_L = j250\Omega$ (green).

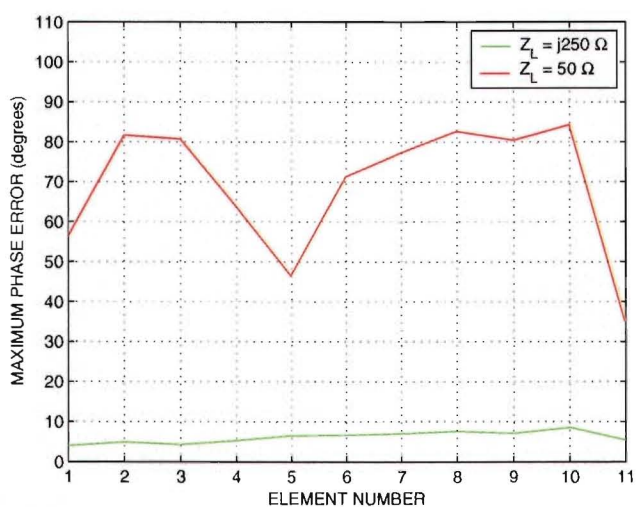


Figure B.10: Maximum phase error versus element number (1 is centre element) in one arm of the non-uniform Y-shaped array, with $Z_L = 50\Omega$ (red) and $Z_L = j250\Omega$ (green).

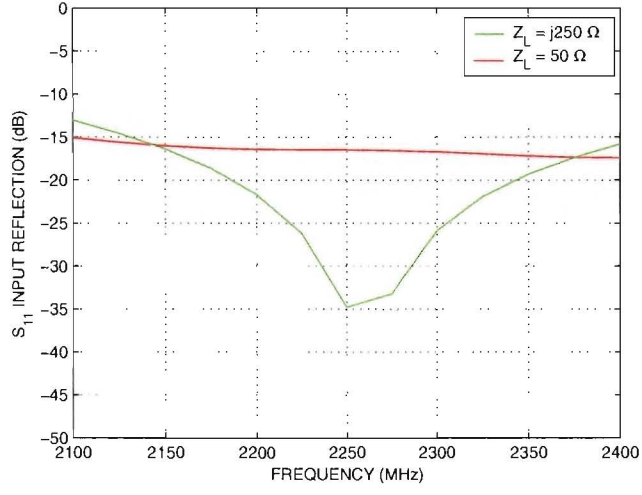


Figure B.11: Input reflection of the 6th element in the non-uniform Y-shaped array, with $Z_L = 50\Omega$ (red) and $Z_L = j250\Omega$ (green).

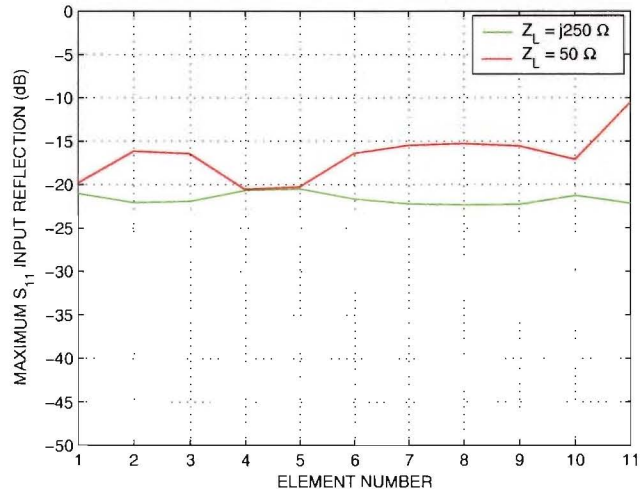


Figure B.12: Maximum input reflection between 2.2GHz-2.3GHz versus element number (1 is centre element) in one arm of the non-uniform Y-shaped array, with $Z_L = 50\Omega$ (red) and $Z_L = j250\Omega$ (green).

B.3 Uniform 3D tilted cross array

Figures B.13 to B.18 show the results for the uniform 3D tilted cross array.

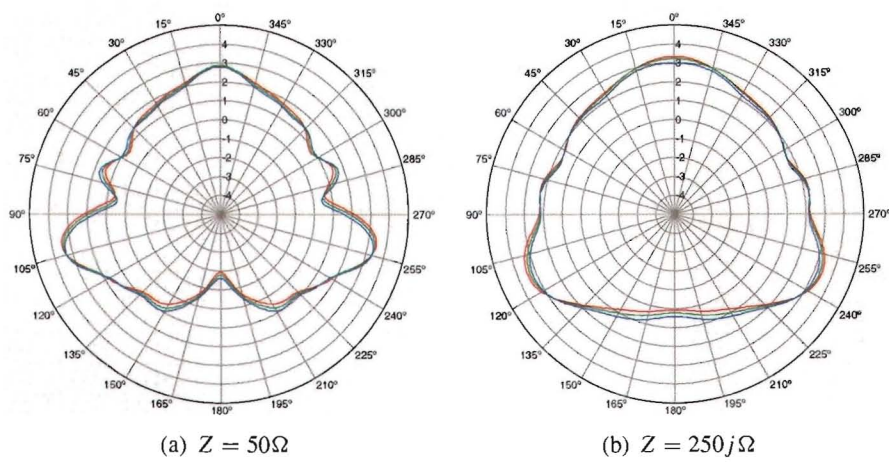


Figure B.13: Element radiation pattern of the 3th element in the uniform 3D tilted cross array at 2200MHz (red), 2250MHz (green) and 2300MHz (blue) with $Z_L = 50\Omega$ (a) and $Z_L = 250j\Omega$ (b).

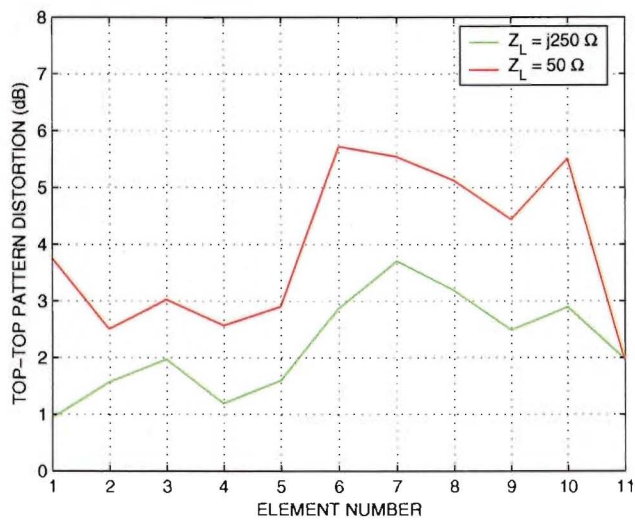


Figure B.14: Top-top radiation pattern distortion versus element number (1 is top, 6 is centre, 11 is lowest element) in one arm of the uniform 3D tilted cross array, with $Z_L = 50\Omega$ (red) and $Z_L = j250\Omega$ (green).

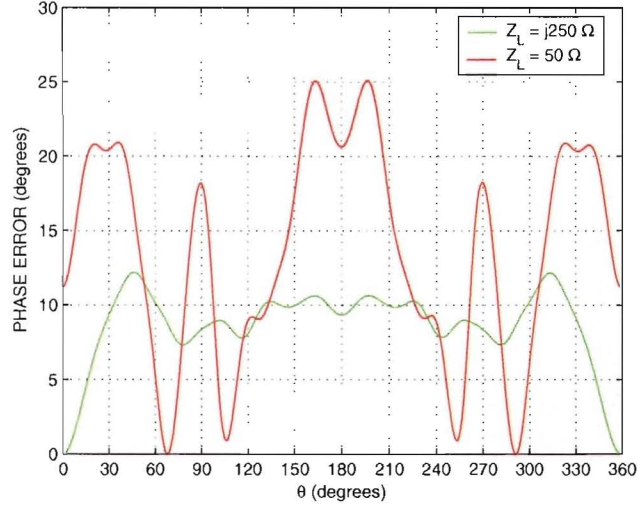


Figure B.15: Phase error of the 3th element in the uniform 3D tilted cross array, with $Z_L = 50\Omega$ (red) and $Z_L = j250\Omega$ (green).

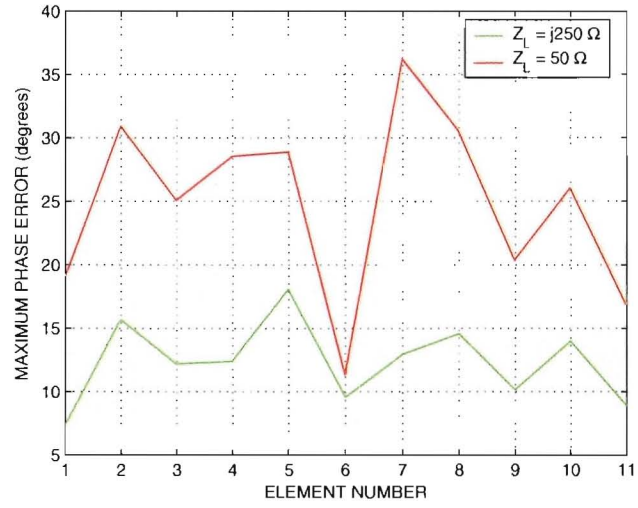


Figure B.16: Maximum phase error versus element number (1 is top, 6 is centre, 11 is lowest element) in one arm of the uniform 3D tilted cross array, with $Z_L = 50\Omega$ (red) and $Z_L = j250\Omega$ (green).

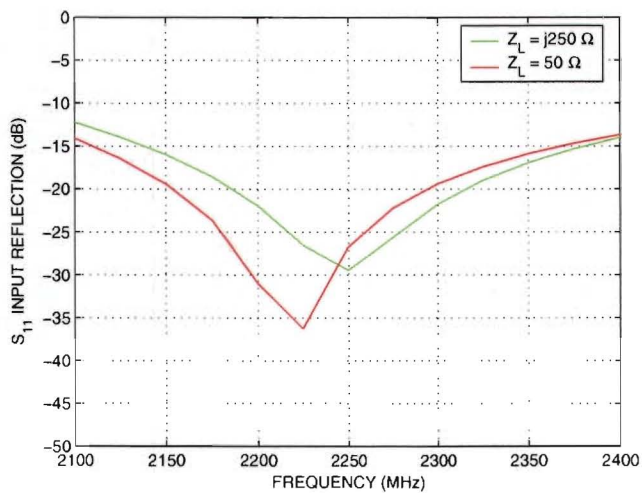


Figure B.17: Input reflection of the 3th element in the uniform 3D tilted cross array, with $Z_L = 50\Omega$ (red) and $Z_L = j250\Omega$ (green).

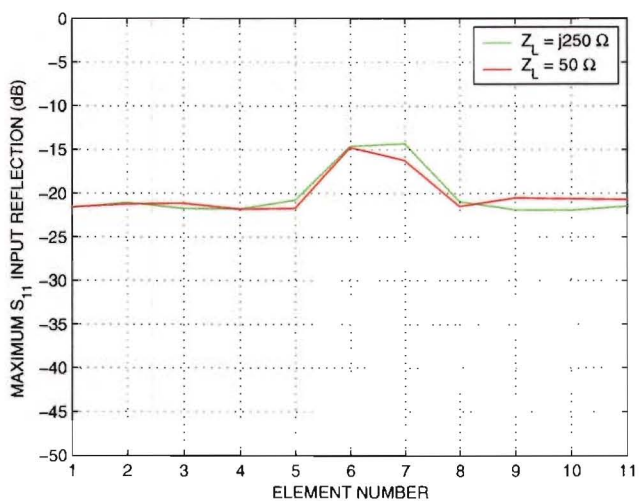


Figure B.18: Maximum input reflection between 2.2GHz-2.3GHz versus element number (1 is top, 6 is centre, 11 is lowest element) in one arm of the uniform 3D tilted cross array, with $Z_L = 50\Omega$ (red) and $Z_L = j250\Omega$ (green).

B.4 Non-uniform 3D tilted cross array

Figures B.19 to B.24 show the results for the non-uniform 3D tilted cross array.

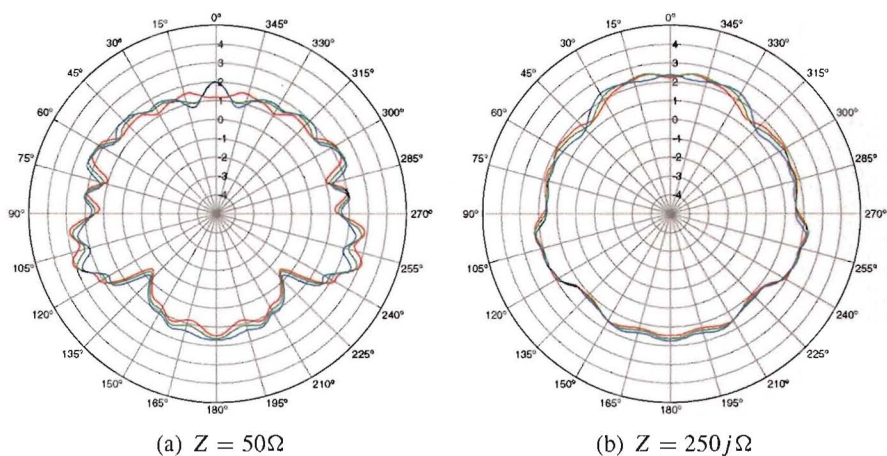


Figure B.19: Element radiation pattern of the 3th element in the non-uniform 3D tilted cross array at 2200MHz (red), 2250MHz (green) and 2300MHz (blue) with $Z_L = 50\Omega$ (a) and $Z_L = 250j\Omega$ (b).

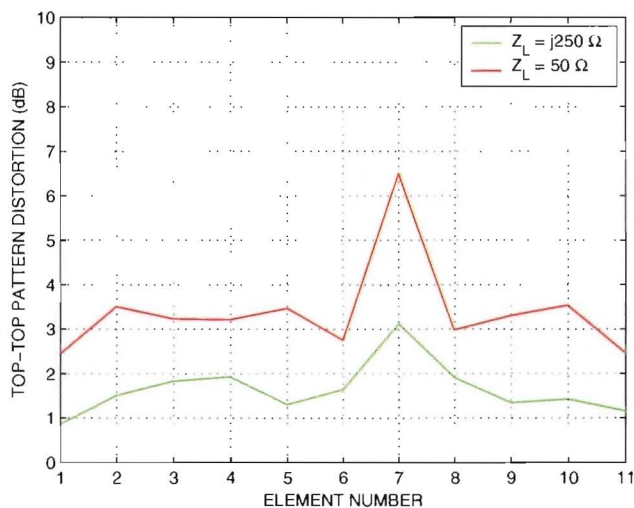


Figure B.20: Top-top radiation pattern distortion versus element number (1 is top, 6 is centre, 11 is lowest element) in one arm of the non-uniform 3D tilted cross array, with $Z_L = 50\Omega$ (red) and $Z_L = j250\Omega$ (green).

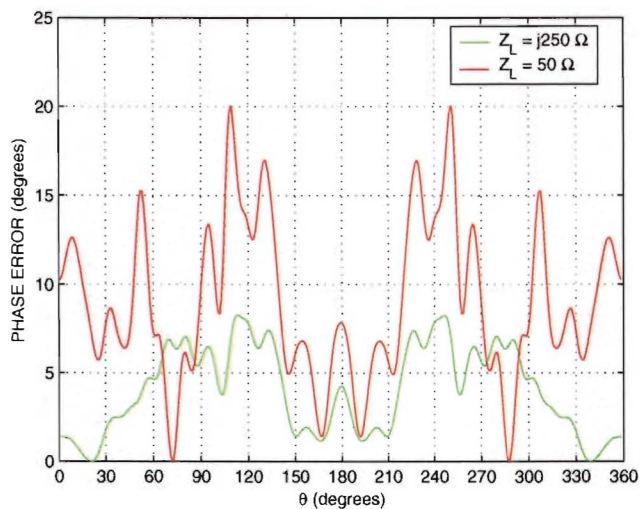


Figure B.21: Phase error of the 3th element in the non-uniform 3D tilted cross array, with $Z_L = 50 \Omega$ (red) and $Z_L = j250 \Omega$ (green).

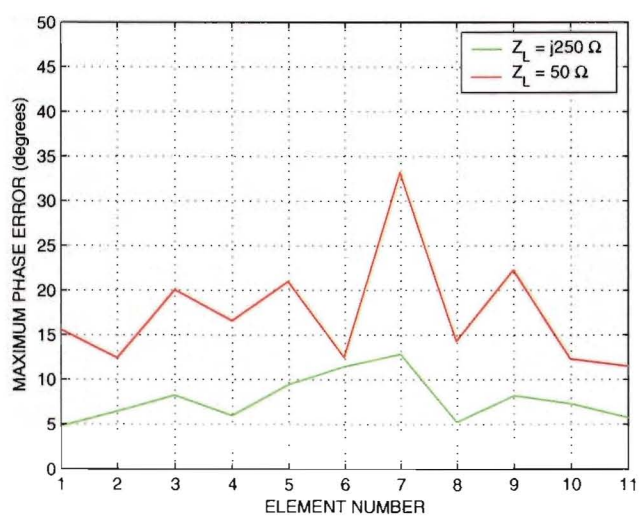


Figure B.22: Maximum phase error versus element number (1 is top, 6 is centre, 11 is lowest element) in one arm of the non-uniform 3D tilted cross array, with $Z_L = 50 \Omega$ (red) and $Z_L = j250 \Omega$ (green).

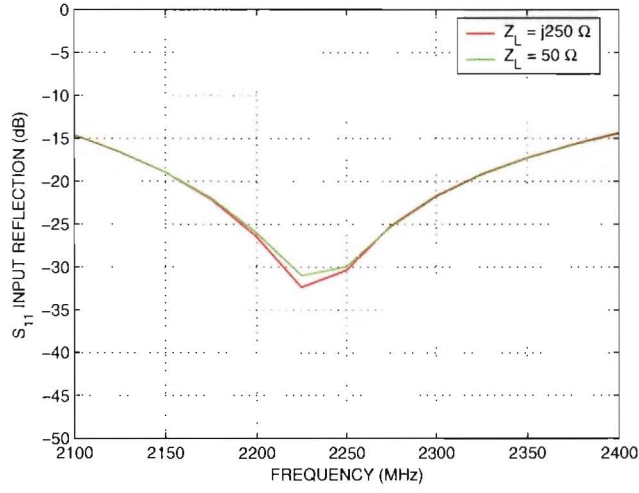


Figure B.23: Input reflection of the 3th element in the non-uniform 3D tilted cross array, with $Z_L = 50\Omega$ (red) and $Z_L = j250\Omega$ (green).

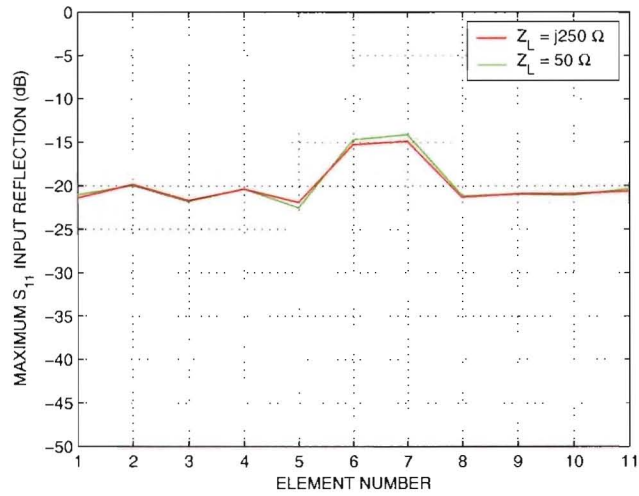


Figure B.24: Maximum input reflection between 2.2GHz-2.3GHz versus element number (1 is top, 6 is centre, 11 is lowest element) in one arm of the non-uniform 3D tilted cross array, with $Z_L = 50\Omega$ (red) and $Z_L = j250\Omega$ (green).

References

- [1] Y.L.C. de Jong, *Measurement and modeling of radiowave propagation in urban micro-cells*, Ph.D. thesis, Technische Universiteit Eindhoven, Eindhoven, The Netherlands, 2001.
- [2] Y.L.C. de Jong, "Suppression of mutual coupling in switched antenna arrays using switched-impedance termination," *Technical Memorandum VPTWS-TM-03-04-06*, Communications Research Centre Canada, 2003.
- [3] R.C. Cristovao, "Design, analysis and measurement of a circular array antenna for direction of arrival estimates," M.S. thesis, IRCTR TUDelft, The Netherlands, 2003.
- [4] K. Kalliola, H. Laitinen, L.I. Vaskelainen, and P. Vainikainen, "Real-time 3-D spatial-temporal dual-polarized measurement of wideband radio channel at mobile station," *IEEE Trans. on Instrumentation and Measurement*, vol. 49, no. 2, pp. 439–448, 2000.
- [5] A. Manikas, A. Alexiou, and H.R. Karimi, "Comparison of the ultimate direction-finding capabilities of a number of planar array geometries," *Proc. Inst. Elect. Eng., Radar, Sonar, Navig.*, vol. 144, no. 6, pp. 1350–2395, 1997.
- [6] R.O. Nielsen, "Azimuth and elevation angle estimation with a three-dimensional array," *IEEE J. Oceanic Eng.*, vol. 19, no. 1, pp. 84–86, 1994.
- [7] S.W. Ellingson, "Design and evaluation of a novel antenna array for azimuthal angle-of-arrival measurement," *IEEE Trans. Ant. Prop.*, vol. 49, no. 6, pp. 971–979, 2001.
- [8] I.J. Gupta and A.A. Ksienski, "Effect of mutual coupling on the performance of adaptive arrays," *IEEE Trans. Ant. Prop.*, vol. 31, no. 5, pp. 785–791, 1983.
- [9] K.M. Pasala and E.M. Friel, "Mutual coupling effects and their reduction in wideband direction of arrival estimation," *IEEE Trans. Aerosp. Electron. Syst.*, vol. 30, no. 4, pp. 1116–1122, 1994.
- [10] J.C. Arnbak, J. Dijk, and M.H.A.J. Herben, *Radio en Radar, Lecture notes*, Technische Universiteit Eindhoven, Eindhoven, The Netherlands, 1998.
- [11] H.R. Karimi and A. Manikas, "Manifold of a planar array and its effects on the accuracy of direction-finding systems," *Proc. Inst. Elect. Eng., Radar, Sonar, Navig.*, vol. 143, no. 6, pp. 349–357, 1996.
- [12] C.A. Balanis, *Antenna theory : analysis and design*, Wiley, Chichester, 1997.

- [13] Y.T. Lo, *Antenna Handbook*, chapter 14, Aperiodic arrays, Van Nostrand Reinhold Company, New York, 1988.
- [14] M. Skolnik, G. Nemhauser, and J. Sherman, "Dynamic programming applied to unequally spaced arrays," *IEEE Trans. Ant. Prop.*, vol. 12, no. 1, pp. 35–43, 1964.
- [15] Y.I. Abramovich, N.K. Spencer, and A.Y. Gorokhov, "Resolving manifold ambiguities in direction-of-arrival estimation for nonuniform linear antenna arrays," *IEEE Trans. Signal Processing*, vol. 47, no. 10, pp. 2629–2643, 1999.
- [16] N. Dowlut and A. Manikas, "A polynomial rooting approach to super-resolution array design," *IEEE Trans. Signal Processing*, vol. 48, no. 6, pp. 1559–1569, 2000.
- [17] M.B. Jorgenson, "Applications of minimum redundancy arrays in adaptive beamforming," *IEE Proc.*, vol. 138, no. 5, pp. 441–447, 1991.
- [18] Ji-Hoon Bae, Kyung-Tae Kim, Joon-Ho Lee, Hyo-Tae Kim, and Jae-Ick Choi, "Design of steerable non uniform linear array geometry for side-lobe reduction," *Microwave Opt. Tech. Lett.*, vol. 36, no. 5, pp. 363–367, 2003.
- [19] Y.I. Abramovich and N.K. Spencer, "Design of nonuniform linear antenna array geometry and signal processing algorithm for DOA estimation of gaussian sources," *Dig. Signal Process*, vol. 10, no. 5, pp. 340–354, 2000.
- [20] EM Software & Systems, *FEKO user's manual*, South Africa, 2003.
- [21] H. Krim and M. Viberg, "Two decades of array signal processing research: the parametric approach," *IEEE Signal Proc. Mag.*, vol. 13, pp. 67–94, 1996.
- [22] R.O. Schmidt, "Multiple emitter location and signal parameter estimation," *IEEE Trans. Ant. Prop.*, vol. 34, no. 3, pp. 276–280, 1986.
- [23] P.J.D. Gething, *Radio direction finding and superresolution*, chapter 12, Superresolution algorithms, Peregrinus, London, 1991.
- [24] L.C. Godara, "Applications of antenna arrays to mobile communications, Part II: Beam-forming and direction-of-arrival considerations," *proc. IEEE*, vol. 85, no. 8, pp. 1195–1245, 1997.
- [25] J.A. Fessler and A.O. Hero, "Penalized maximum-likelihood image reconstruction using space-alternating generalized EM algorithms," *IEEE Trans. Image Proc.*, vol. 4, no. 10, pp. 1417–1429, 1995.
- [26] A.Y.J. Chan and J. Litva, "MUSIC and maximum likelihood techniques on two-dimensional DOA estimation with uniform circular array," *Proc. Inst. Elect. Eng., Radar, Sonar, Navig.*, vol. 142, no. 3, pp. 105–114, 1995.
- [27] R. Roy, A. Paulraj, and T. Kailath, "ESPRIT—A subspace rotation approach to estimation of parameters of cisoids in noise," *IEEE Trans. Acoust., Speech, Signal Processing*, vol. 34, no. 5, pp. 1340–1342, 1986.
- [28] A.L. Swindlehurst and T. Kailath, "A performance analysis of subspace-based methods in the presence of model errors – Part II: Multidimensional algorithms," *IEEE Trans. Sig. Proc.*, vol. 41, no. 9, pp. 2882–2890, 1993.

- [29] M. Haardt and M.E. Ali-Hackl, "Unitary ESPRIT: how to exploit additional information inherent in the relational invariance structure," *Proc. ICASSP '94*, vol. 4, pp. 229–232, 1994.
- [30] M. Haardt and J.A. Nosssek, "Unitary ESPRIT: How to obtain increased estimation accuracy with a reduced computational burden," *IEEE Trans. Signal Process*, vol. 43, no. 5, pp. 1232–1242, 1995.
- [31] P. Satayarak, P. Rawiwan, P. Supanakoon, M. Chamchoi, S. Promwong, and P. Tangtisanon, "The achievable performance of Unitary-ESPRIT algorithm for DOA estimation," *proc. ITC-CSCC*, pp. 1578–1582, 2002.
- [32] D. Zoltowski, M. Haardt, and C.P. Mathews, "Closed form 2-D angle estimation with rectangular arrays in element space or beam space via Unitary ESPRIT," *IEEE Trans. Signal Process*, vol. 44, no. 2, pp. 316–328, 1996.
- [33] M. Haardt and J.A. Nosssek, "Simultaneous Schur decomposition of several nonsymmetric matrices to achieve automatic pairing in multidimensional harmonic retrieval problems," *IEEE Trans. Signal Process*, vol. 46, no. 1, pp. 161–169, 1998.
- [34] M. Tschudin, C. Brunner, T. Kurpjuhn, M. Haardt, and J.A. Nosssek, "Comparison between Unitary ESPRIT and SAGE for 3-D channel sounding," *Proc. 49th IEEE Vehicular Technology Conf. Spring (VTC '99 Spring)*, vol. 2, pp. 1324–1329, 1999.
- [35] P. Strobach, "Total least squares phased averaging and 3-D ESPRIT for joint azimuth-elevation-carrier estimation," *IEEE Trans. Signal Process*, vol. 49, no. 1, pp. 54–62, 2001.
- [36] M. Haardt, "Structured least squares to improve the performance of ESPRIT-type algorithms," *IEEE Trans. Signal Process*, vol. 45, no. 3, pp. 792–799, 1997.
- [37] G.H. Golub and C.F. van Loan, *Matrix computations*, The Johns Hopkins University Press, Baltimore, MD, 1989.
- [38] R. Eckhoff, "Direction-of-arrival determination using 3-axis crossed array and ESPRIT," *Proc. Ninth IEEE Int. Symp. on Personal, Indoor and Mobile Communications.*, vol. 1, pp. 471–475, 1998.
- [39] R.J.C. Bultitude, T.J. Willink, M.H.A.J. Herben, and G. Brussaard, "Detection of changes in the spectra of measured CW mobile radio data for space wave modelling applications," *Proc. of the Queens University Biennial Symposium on Communications, Kingston, Canada*, pp. 90–94, 2000.
- [40] S. Kravitz, "Packing cylinders into cylindrical containers," *Math. Mag.*, vol. 40, pp. 65–70, 1967.
- [41] F.E. Terman, *Radio Engineers Handbook*, chapter 3, Circuit theory, McGraw-Hill book Company, New York, 1943.